Laser powder bed fusion of soft magnetic metallic glasses. A fundamental study on the interplay between processing conditions, defects, microstructure and properties

by

Marcos Rodríguez Sánchez

A dissertation submitted in partial fulfillment of the requirements for the degree of Doctor of Philosophy in

Materials Science and Engineering

Universidad Carlos III de Madrid

Advisor:

Dr. María Teresa Pérez Prado

Tutor:

Prof. Mónica Campos Gómez

February 2026

This thesis is distributed under license “Creative Commons **Atribuittion - Non Commercial - Non Derivatives**”.

"Good evening, Mr. Putt…

…I have also spoken with my parents about this, and they agree and support me."

ACKNOWLEDGEMENTS

This thesis is the culmination of four years where I have worked alongside some incredibly talented, curious, caring and motivating professionals. Without them, this work would not have been possible and I would like to devote a few words to show them my appreciation for their help and support.

First and foremost, I would like to thank my PhD supervisor, Dr. Teresa Pérez Prado. Teresa, hacer un doctorado nunca había entrado en mis planes, hasta que te conocí. Al poco tiempo de empezar a trabajar en tu grupo, contagiarme de tu entusiasmo y sentir tu apoyo en todo momento, supe que era la mejor decisión que podría haber tomado. Has sido y siempre serás, un ejemplo a seguir a nivel cientfífico y personal. Espero algún día ilusionar a la gente que trabaje conmigo como lo haces tú.

This work has been carried out at IMDEA Materials Institute, in collaboration with two departments at the University of Saarland, the Chair of Metallic Materials and the Laboratory of Actuation Technology, the Technical University of Berlin, the Istituto Nazionale di Ricerca Metrologica, Hereaus AMLOY and AMAZEMET. I would like to personally thank all researchers involved in the project who I had the pleasure to work with and share great times at project meetings and conferences.

I will always be grateful to the members of the Sustainable Metallurgy group at IMDEA Materials. Shruti, Xueze, thank you for welcoming me and teaching me the basics around the lab. Sergi, gracias por tu ayuda con el análisis de imágenes y tu recibimiento en Leitat. Souvik, thank you for your advice on mechanical properties and EBSD analysis and for your ever-present smile. Henry, thank you for joining this group, for bringing your enthusiasm and for putting up with all the Spanish talk at IMDEA and outside. Carmen, Phoebe, thank you both for your contributions to this research during your stays at IMDEA. Li, even though our time together at IMDEA was short, it has been a pleasure working with you. I am excited to follow your work in the future. Saumya, seeing you grow has been truly inspiring. Despite the difficulties you have faced, you have persisted and finished an amazing piece of work. From our first *jugaad* in the AM lab to the last conference trip, I have learned more from you than you know. Nacho, como te he dicho muchas veces, he intentado seguir tus pasos en lo profesional y en lo humano, en la medida de lo posible. He disfrutado de trabajar contigo casi tanto como de tu amistad y seguiré disfrutando de verte brillar allá donde vayas.

I would also like to thank all the researchers and technical staff who have participated, direclty or indirectly, in the generation of results covered in this thesis. Adrian, he tenido mucha suerte de poder colaborar contigo en el ámbito científico y en las primeras etapas del emprendimiento. Fue un momento muy emocionante y lo repitiría si volviese a empezar. Amalia, te agrdezco de corazón tus consejos, tu paciencia y tu disposición para ayudarnos a todos. Eres la fuerza motora del trabajo experimetal que se hace en IMDEA. Nacho, muchas gracias a ti también por tu amistad y por tu ayuda con las primeras fabricaciones y a ti, Teri, por tu ayuda con las últimas. Gracias a Javier García, Miguel Monclús, Manuel Avella, Vanesa Martínez, José Luis Jiménez y Jesús Carreras por vuestra ayuda con el trabajo de laboratorio. Trabajar con vosotros hace que las técnicas más avanzadas parezcan sencillas. Thank you Ilchat Sabirov, Damien Tourret and Juan Pedro Fernández for giving me valuable advice when I needed it the

most. Y por supuesto, gracias, Cris, por comentar cada lunes los partidos de fútbol del fin de semana, y por dedicarnos una sonrisa cada mañana, haciendo cada día de esta tesis un poco mejor.

I have met some incredible people during these years who may not have participated in this thesis research, but have made IMDEA Materials a place where I truly loved working. Jorge, Jose, Guille (y los demás), Eugenia, Davide, Paul, Yi, Raúl, las Ángelas, Sofía, Lola, Edu, Óscar, Valerio, Vittoria, Carmen, Alberto, Venkatesh, gracias por todos los momentos que hemos compartido estos años, dentro y fuera de IMDEA.

The biggest support I received to finish this thesis came from outside the academic world. To be precise, she came from Além Paraiba, MG. My wife, Bruna, who put her plans on hold to move to Madrid and made this journey part of hers too. Bruna, this would not have been possible without your love, your celebration of my accomplishments and the support you gave me when the most frustrating moments came. I cannot thank you enough for letting me grow professionally and personally by your side.

I am also incredibly thankful to my family, who always stood by me. Mamá, papá, gracias por vuestra integridad ejemplar, por animarme a trabajar en lo que más me apasiona y por los muchos, muchos "extra efforts" que hicisteis para darnos a Berta y a mi innumerables oportunidades. Y por último, pero no menos importante, Berta, gracias por ser mi fiel compañera, por defenderme cuando lo necesitaba y por ayudarme a ver las cosas igual de claras que tú.

The work hereby presented has been carried out under the scope AM2SoftMag project (GA number 101046870), funded by the European Union. Views and opinions expressed are however those of the author(s) only and do not necessarily reflect those of the European Union or the European Innovation Council and SMEs Executive Agency (EISMEA). Neither the European Union nor the granting authority can be held responsible for them.

Funded by the
European Union

PUBLISHED AND SUBMITTED CONTENT

1. **Relating laser powder bed fusion process parameters to (micro)structure and to soft magnetic behavior in a Fe-based bulk metallic glass.**

   - **M. Rodríguez-Sánchez**, S. Sadanand, A. Ghavimi, R. Busch, P. Tiberto, E. Ferrara, G. Barrera, L. Thorsson, H.J. Wachter, I. Gallino, M.T. Pérez-Prado.
   - Published in *Materialia*, vol. 35 (2024), 102111.
   - https://doi.org/10.1016/j.mtla.2024.102111
   - This article is partially included in Chapter 4.
   - The material from this source included in this thesis is not singled out with typographic means and references.
   - Role: Writing - original draft, visualization, methodology, investigation, formal analysis.

2. **Laser powder bed fusion of an Fe-based metallic glass using time delays.**

   - **M. Rodríguez-Sánchez**, A.D. Boccardo, S. Sadanand, A. Ghavimi, R. Busch, P. Sharangi, E. Ferrara, G. Barrera, P. Tiberto, D. Tourret, I. Gallino, M.T. Pérez-Prado.
   - Published in *Additive Manufacturing*, vol. 110 (2025), 104922.
   - https://doi.org/10.1016/j.addma.2025.104922
   - This article is partially included in Chapter 6.
   - The material from this source included in this thesis is not singled out with typographic means and references.
   - Role: Conceptualization, formal analysis, investigation, methodology, visualization, writing - original draft.

3. **Multi-scale mechanical characterization of an additively manufactured Fe-based glass-forming alloy.**

   - C. Garrote-Junco, A. Ghavimi, R. Busch, M.T. Pérez-Prado, **M. Rodríguez-Sánchez.**
   - Published in *Additive Manufacturing Letters*, vol. 15 (2025), 100345.
   - https://doi.org/10.1016/j.addlet.2025.100345
   - This article is partially included in Chapter 5.
   - The material from this source included in this thesis is not singled out with typographic means and references.
   - Role: Conceptualization, Formal analysis, Methodology, Supervision, Validation, Visualization, Writing – review & editing.

OTHER RESEARCH MERITS

PATENTS

1. **Laser-based additive manufacturing device and method for crystallization control of metallic glasses.**
   - **M. Rodríguez-Sánchez**, M. T. Pérez-Prado, A. D. Boccardo, D. Tourret.
   - Patent application number EP24383248.2 - submitted to the European Patent Office on November 2024.

PUBLICATIONS NOT INCLUDED IN THIS THESIS - PUBLISHED OR SUBMITTED

1. **Laser powder bed fusion of a nanocrystalline Finemet Fe-based alloy for soft magnetic applications.**
   - S. Sadanand, **M. Rodríguez-Sánchez**, A. Ghavimi, R. Busch, P. Sharangi, P.M. Tiberto, E. Ferrara, G. Barrera, L. Thorsson, H.J. Wachter, I. Gallino, M.T. Pérez-Prado.
   - Published in *Journal of Laser Applications*, vol. 36, (2024), 042029.
   - https://doi.org/10.2351/7.0001391
   - This article is not included in this thesis.
   - Role: Investigation; Methodology; Writing – original draft; Writing – review & editing.
2. **Assessment of the Fe-Si-B eutectic composition using calorimetry and microstructural analysis.**
   - A. Ghavimi, M. Rahimi Chegeni, L. Ruschel, B. Adam, **M. Rodríguez-Sánchez**, M.T. Pérez-Prado, I Gallino, R. Busch.
   - Submitted to *Materials Today Communications*.
   - This article is not included in this thesis.
   - Role: Investigation, Methodology; Writing – review & editing.
3. **Crystallization during laser powder bed fusion of the Finemet soft magnetic glass-forming alloy.**
   - S. Sadanand, A.D. Boccardo, B. Yang, **M. Rodríguez-Sánchez**, A. Ghavimi, R. Busch, I. Gallino, M.T. Pérez-Prado.
   - Submitted to *Additive Manufacturing*.

– This article is not included in this thesis.
– Role: Validation; Methodology; Writing – review & editing.

ORAL PRESENTATIONS AT NATIONAL AND INTERNATIONAL CONFERENCES

1. **Laser powder bed fusion of soft magnetic bulk metallic glasses.**
   – **M. Rodríguez-Sánchez**, S. Sadanand, A. Ghavimi, R. Busch, I. Gallino, P. Tiberto, E.Ferrara, G. Barrera, M.T. Pérez-Prado.
   – Oral presentation at Alloys for Additive Manufacturing Symposium 2023 (Madrid, September 2023).
2. **Laser powder bed fusion of soft magnetic amorphous metals.**
   – **M. Rodríguez-Sánchez**, S. Sadanand, A. Ghavimi, R. Busch, I. Gallino, P. Tiberto, E.Ferrara, G. Barrera, M.T. Pérez-Prado.
   – Oral presentation at Euro PM 2023 (Lisbon, October 2023).
3. **Relating LPBF process parameters to (micro)structure and to soft magnetic behavior in a Fe-based bulk metallic glass.**
   – **M. Rodríguez-Sánchez**, S. Sadanand, A. Ghavimi, R. Busch, P. Sharangi, E.Ferrara, G. Barrera, P. Tiberto, L. Thorsson, H.J. Wachter, I. Gallino, M.T. Pérez-Prado.
   – Oral presentation at 19th European Mechanics of Materials Conference (Madrid, May 2024).
4. **Relating LPBF process parameters to (micro)structure and to soft magnetic behavior in a Fe-based bulk metallic glass.**
   – **M. Rodríguez-Sánchez**, S. Sadanand, A. Ghavimi, R. Busch, P. Sharangi, E.Ferrara, G. Barrera, P. Tiberto, L. Thorsson, H.J. Wachter, I. Gallino, M.T. Pérez-Prado.
   – Oral presentation at Alloys for Additive Manufacturing Symposium 2024 (Paris, September 2024).
5. **LPBF of novel soft magnetic metallic glasses.**
   – **M. Rodríguez-Sánchez**, S. Sadanand, A. Ghavimi, I. Gallino, P. Sharangi, E.Ferrara, G. Barrera, P. Tiberto, L. Thorsson, C. Zintel, A. Elsen, R. Busch, M.T. Pérez-Prado.
   – Oral presentation at Alloys for Additive Manufacturing Symposium 2025 (Neuchâtel, September 2025).

CONTENTS

LIST OF FIGURES

LIST OF TABLES

LIST OF ABBREVIATIONS

Abbreviation	Definition
AM	Additive manufacturing
BMG	Bulk metallic glass
LPBF	Laser powder bed fusion
SLM	Selective laser melting
PBF-LB/M	Laser-based powder bed fusion of metals
DED	Direct energy deposition
P	Laser power
v	Scan speed
h	Hatch distance
t	Layer thickness
BD	Build direction
CW	Continuous wave
PW	Pulsed wave
t_{ON}	Exposure time
pd	Point distance
ϕ	Laser's spot size
t_{OFF}	Time delay
VED	Volumetric energy density
$E*$	Dimensionless volumetric energy density
$P*$	Dimensionless laser power
$v*$	Dimensionless scan speed
$h*$	Dimensionless hatch distance
$t*$	Dimensionless layer thickness
α_p	Absorptivity of the powder
ρ	Density
c_p	Specific heat capacity
T_m	Melting temperature

Abbreviation	Definition
T_0	Basal temperature
$\overline{\Delta H}$	Normalized enthalpy
MP	Melt pool
HAZ	Heat affected zone
LoF	Lack of fusion
GB	Grain boundary
R_c	Critical cooling rate
T_x	Crystallization temperature
TTT	Time-temperature transformation
T_L	Liquidus temperature
T_g	Glass-transition temperature
GFA	Glass-forming ability
T_{rg}	Reduced glass-transition temperature
t_c	Critical casting thickness
d_c	Critical casting diameter
H_a	Applied magnetic field
M	Magnetization
SMM	Soft magnetic material
M_s	Saturation magnetization
H_c	Magnetic coercivity
χ	Magnetic susceptibility
RE	Rare earth
SEM	Scanning electron microscopy
SWAP	Spinning water atomization
FEG	Field emission gun
PSD	Particle size distribution
SE	Secondary electron
ρ_a	Apparent density
ρ_t	Tapped density
CI	Carr index
HR	Housner ratio

Abbreviation	Definition
RBV	Reduced build volume
OM	Optical microscopy
XCT	X-ray computed tomography
XRD	X-ray diffraction
DSC	Differential scanning calorimetry
ΔH_{cr}	Crystallization enthalpy
AM %	Amorphous fraction
EBSD	Electron bakcscattered diffraction
TEM	Transmission electron microscopy
FFT	Fast Fourier transform
APT	Atom probe tomography
VSM	Vibrating sample magnetometer
E_r	Reduced elastic modulus
E	Young's modulus of the material
ν	Poisson's ratio of the material
E_i	Young's modulus of the instrument
ν_i	Poisson's ratio of the instrument
FEM	Finite element method
k	Thermal conductivity
T	Temperature
Q_l	Absorbed heat due to the laser's incidence
Q_ϕ	Absorbed/released heat due to melting/solidification
H_l	Laser's penetration depth
(x_l, y_l)	Coordinates of the center of the laser's spot
L_f	Latent heat of fusion
f_s	Solid volume fraction
q_c	Heat flux
h_c	Interfacial heat transfer coefficient
T_∞	Temperature of the environment
T_S	Solidus temperature
τ	Time within T_x and T_S

Abbreviation	Definition
ND	Normal direction
W	Melt pool width
D	Melt pool depth
S	Sample size
a	Defect's length perpendicular to the build direction
b	Defect's length parallel to the build direction
σ	Stress
e	Strain
σ_{max}	Maximum stress
e_u	Uniform strain
H	Hardness
SD	Scan direction
μ	Pearson coefficient

1. INTRODUCTION

1.1. Preamble

In modern times, society's need for efficient energy conversion and storage materials is growing in parallel to the demand of increasingly accessible electric devices. As part of the global goal to reduce greenhouse gas emissions, emphasis has been placed on the replacement of combustion engines for electric motors in the transportation sector. Since electric alternatives are mostly available at a higher cost, much attention and research work has focused on improving the efficiency of such electrical devices.

Additive manufacturing (AM), also known as 3D printing, is a rapidly growing field in the manufacturing industry. It is a process that involves creating three-dimensional objects layer by layer using digital models as a reference [1]. AM offers numerous advantages over traditional manufacturing techniques, including greater design freedom, customization and the potential to reduce manufacturing waste and costs [1–3].

Soft magnetic bulk metallic glasses (BMGs) are a kind of metallic alloys distinguished by their outstanding magnetic properties arising from their characteristic amorphous microstructure. These materials can only be manufactured with specific methods that provide extremely high cooling rates, which produce thin plates, ribbons or fine metallic powder. Nevertheless, they have been used for electromagnetic components for decades, despite the evident limitations on the manufacturing side. AM techniques like laser powder bed fusion (LPBF) have opened the door to fabricating large components with complex geometries out of soft magnetic BMGs. While this is a promising approach to produce highly efficient electrical machines, reducing energy losses and contributing towards reducing greenhouse emissions, a number of new challenges arise with the use of LPBF of BMGs. The high number of processing parameters and repeated thermal cycles inherent to the metal LPBF process, as well as the metastable nature of metallic glasses, require great control of the manufacturing process to achieve the desired material properties.

1.2. Research Objectives

This doctoral thesis addresses the knowledge gap at the intersection of additive manufacturing and soft magnetic metallic glasses by providing a deeper understanding about the complex relationship between LPBF processing conditions, the internal structure of manufactured parts, and the final material properties. For this purpose, the following research objectives were set for this work:

- Understanding of fundamental relationships between the most influential LPBF processing parameters, internal defect structure, (micro)structure, and magnetic properties using a commercial glass-forming composition and a simple scanning strategy.
- Study of the effect of typically generated internal defects and microstructural features on the mechanical behavior of LPBF-processed parts of said commercial composition.
- Investigation of advanced scanning strategies to control heat accumulation, improve the retention of amorphous structure and enhance the magnetic behavior of LPBF-manufactured parts using a commercial composition with limited glass-forming ability.
- Implementation of the most successful processing parameters and strategies on a newly designed composition with improved thermal stability to achieve a superior soft magnetic behavior.

1.3. Outline

This thesis will be structured as follows. Chapter 2 provides a theoretical background of the three core topics of this work: laser powder bed fusion, metallic glasses, and soft magnetic materials. Additionally, this chapter provides a review of the most relevant literature on each of these fields and on the intersection of the three. Chapter 3 presents the materials, instruments and general methodology used throughout the entirety of the work. Other methodologies used for specific studies will be explained in detail in the corresponding chapters. The next four chapters include the core results of this work. Chapter 4 addresses the first research objective, using a commercial alloy as feedstock material and a simple scanning strategy. Chapter 5 evaluates the mechanical properties of the same commercial alloy. In Chapter 6, the use of time delays as

a strategy to achieve a more favorable (micro)structure and soft magnetic properties is explored. Next, Chapter 7 aims to apply the knowledge obtained on the commercial composition to LPBF processing of a new alloy with enhanced properties. Chapter 8 summarizes the most relevant contributions of this work towards filling the presented gaps in the literature. Finally, Chapter 9 highlights several areas that remain unexplored based on the findings included in this thesis.

2. STATE OF THE ART

This chapter covers the most relevant information needed to understand the work carried out in this thesis. It is divided in four sections, each addressing a relevant topic.

First, powder bed fusion of metals will be introduced and discussed in detail. As this is the main manufacturing technique utilized in this work, a description will be provided of the main processing parameters, the internal defects that can be generated during fabrication and commonly used scanning strategies used to achieve stable builds.

Secondly, glass-forming alloys will be discussed. Emphasis will be put on their characteristic structure, their properties and the most commonly used manufacturing routes for this family of materials. The pioneering works on additive manufacturing of glass-forming alloys will be presented, along with the challenges found in recent years.

Next, an introduction to soft magnetic materials will be given. The role they play in critical modern technologies will be explained, followed by an review of the magnetic phenomena and micro-structural characteristics that endow these materials with the properties that are most sought after in the industry. In connection with the previous section, the structure and properties soft magnetic glass-forming alloys will be discussed in detail.

Ultimately, the literature will be reviewed on the intersection of the three aforementioned topics: Powder bed fusion of soft magnetic glass-forming alloys. The relationships between microstructure and soft magnetic behavior and between internal defects and mechanical properties will be presented. Lastly, recent advances associated to the use of complex scanning strategies will be reviewed and the current challenges faced in the field will be highlighted.

2.1. Laser Powder Bed Fusion

Laser powder bed fusion is one of the most commonly used metal additive manufacturing techniques in today's manufacturing industry. Throughout the years, different names have been utilized to refer to this technique, which can therefore be found in the literature under selective laser melting (SLM) or direct melting laser sintering (DMLS). Although laser-based powder bed fusion of metals (PBF-LB/M) is the standard name from ISO/ASTM 52900, LPBF will

also be used throughout this thesis for brevity. LPBF belongs to the category of additive manufacturing of metals where the feedstock material is in the form of powder, along with electron beam-based powder bed fusion (PBF-EB/M), direct energy deposition (DED) and binder jetting [1–3].

The working principle of the LPBF process is depicted in Fig. 2.1. It consists of a recoater which spreads a thin layer of powder (ideally 20 - 60 μm in size) over a build plate or substrate. The powder layer is then scanned by a high energy laser, melting a cross-section of the object that is being printed, according to an input 3D model that must be provided to the system's control unit. If the feedstock powder is stored in a reservoir adjacent to the build plate, the reservoir is raised and the build plate is lowered by the same distance simultaneously, prior to the recoater's spread of a new layer over the powder bed. Alternatively, the powder reservoir may be placed above the system, in which case the build plate is lowered, the needed amount of powder is deposited next to the powder bed and finally the new powder layer is spread. This process is repeated layer by layer and, upon completion of the build job, the powder is removed and can be reused for further printing.

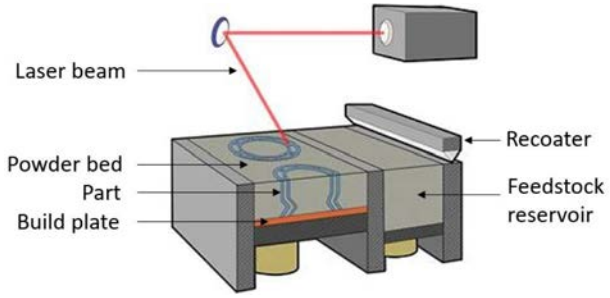

Figure 2.1. Schematic of the laser powder bed fusion process [2].

LPBF has become very popular in the past few decades, as it poses several advantages over traditional manufacturing methods. First, it offers the possibility to produce complex geometries, otherwise unattainable by casting or subtractive methods like turning or milling. Furthermore, it allows to reuse unmelted feedstock material, limiting the material waste. Finally, it also provides high local cooling rates, in the range of $10^5 - 10^7$ K/s [3], which yield specific microstructures and properties. On the other hand, it poses several challenges, as the quality of the final part is determined by the coupled effect of many parameters related to the laser, to the scan path, to the material, to the powder-laser interaction, to the chamber's atmosphere, and more. It is crucial to understand the effect of these parameters on the generation of internal defects, on microstructural changes and, ultimately, on the properties of the manufactured components.

2.1.1. Processing parameters

The main processing parameters that can be tuned in the LPBF process are the laser power (P), the scan speed (v), the hatch distance (h), and the layer thickness (t) [3]. Fig. 2.2 provides a diagram illustrating these four parameters. The laser power is simply the energy per unit time that is applied by the laser. The scan speed is the velocity at which the laser's focal point moves over the plane perpendicular to the build direction (BD). For continuous wave (CW) emission lasers, it can be directly tuned by the user. However, pulsed wave (PW) emission lasers scan individual exposure spots and are turned off when they shift from one spot to the next. This can be done very quickly such that the laser produces one continuous melting track, but the parameters that control the speed are, in this case, the exposure time (t_{ON}) and the point distance (pd), according to the following relationship:

$$v = \frac{pd}{t_{ON} + 10} \tag{2.1}$$

where the 10 in the denominator is the minimum time (in μs) needed for the laser to move from one exposure point to the next, during which the laser remains turned off. The hatch distance or hatch spacing is the distance between the center of two adjacent tracks. Lastly, the layer thickness is the distance that the build plate is lowered every layer, which is filled by powder during the recoater's motion.

Additional relevant parameters for the work carried out in this thesis are the laser's spot size (ϕ) and the time delays (t_{OFF}). The spot size has a minimum value for each LPBF system but it can be increased by shifting the laser's focal point. If all other parameters are kept constant, this reduces the energy input per surface unit. Time delays refer to the period of time that the laser is switched off at the end of each track. Most LPBF systems have a default value which is needed for the servo motors of the optic system to decelerate at the end of a track and to accelerate at the beginning of the next one. Time delays can also be increased, leaving longer times between subsequent melt tracks.

2.1.2. Energy input

Several analytical expressions can be used to model the energy input applied during the LPBF process as a function of the selected processing parameters. The most commonly used

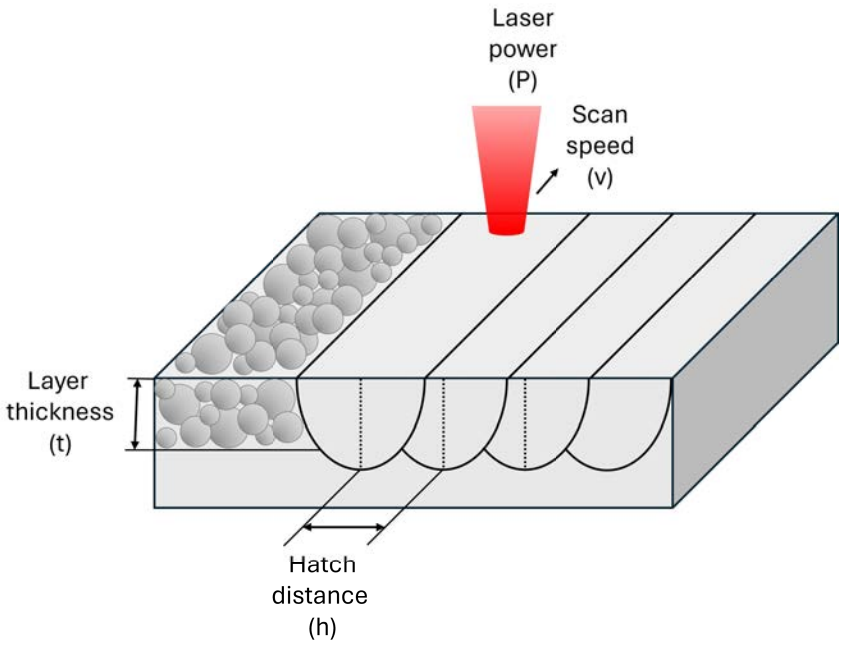

Figure 2.2. Diagram illustrating the main processing parameters of the LPBF process.

magnitude is the volumetric energy density (VED), which is calculated (in J/mm^3) with the following expression:

$$VED = \frac{P}{vht} \tag{2.2}$$

The VED is a simple and effective function that takes into account the four major parameters discussed in Section 2.1.1 and is able to roughly predict the generation of internal defects due to insufficient or excess input energy for a specific material and LPBF system [4]. However, it has been argued that it is overly simplistic and is not effective at translating processing parameters from one material to another or from one LPBF system to another [5, 6]. The normalized VED (E^*) , is a modified version put forward by Thomas et al. [5] that incorporates material and powder properties, as described by the following formula:

$$E^* = \frac{P^*}{v^* h^* t^*} = \frac{\alpha_p P}{2vht\rho c_p (T_m - T_0)}, \tag{2.3}$$

where P^*, v^*, h^*, and t^* are the dimensionless laser power, scan speed, hatch distance and layer thickness, respectively. The expressions for each normalized parameter are $P^* = \alpha_p P/[\phi D\rho c_p(T_m - T_0)]$, $v^* = v\phi/D$, $h^* = h/\phi$, and $t^* = 2t/\phi$. Here, α_p is the absorptivity of the powder, D is the thermal diffusivity, ρ is the density, c_p is the specific heat capacity, T_m is the melting tem-

perature, T_0 is the basal temperature of the material, which can be used to account for the temperature of the previous layer or track when a new track is scanned [7].

A third function put forth by Hann et al. [8], known as the normalized enthalpy ($\overline{\Delta H}$) was originally used to predict the dimensions of a weld track. Later, Ghasemi-Tabasi et al. [6] used it as a rule to identify optimal LPBF processing parameters and to adapt them from one material to another. $\overline{\Delta H}$ has proven to be quite effective to translate processing parameter combinations that yielded minimal defects on bronze to red-gold and 316L steel [6]. $\overline{\Delta H}$ can be calculated using the following expression:

$$\overline{\Delta H} = \frac{\alpha P}{\rho(c_p(T_m - T_0) + L_m)\sqrt{\pi D \phi^3 v}}, \tag{2.4}$$

where L_m is the latent heat of melting. Besides incorporating additional material properties such as L_m and the D, $\overline{\Delta H}$ can be effectively used to predict the melting mode. Depending on the energy input, two melting modes can be achieved in LPBF: conduction or keyhole, which are illustrated in Fig. 2.3. Both are described in detail below.

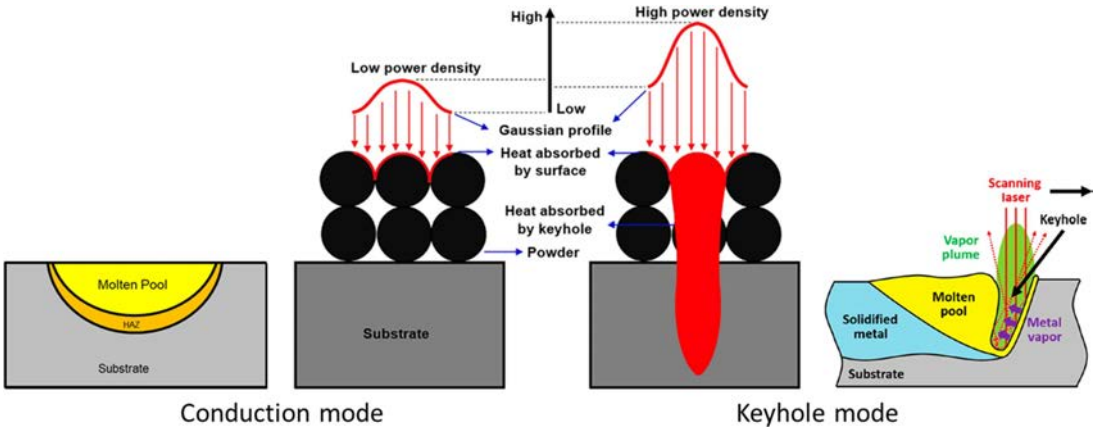

Figure 2.3. Diagram showing the conduction and keyhole melting modes in LPBF [9].

Conduction melting takes place when relatively low energy is applied to the system. In this melting mode, the temperature in the molten metal does not raise significantly over its boiling point, so the vapor cavity and its associated effects are negligible. Therefore, heat conduction is the main heat dissipation mechanism after the laser melts the material [10]. This melting mode leads to the formation of semi-circular melt pools (MPs) [9], which are surrounded by a heat affected zone (HAZ), as shown in Fig. 2.3. The latter consists of material solidified in previous layers, which is not remelted during the scanning of a new layer but undergoes a strong reheating cycle, often resulting in local micro structural changes.

Alternatively, when a relatively high energy input is applied to the material, the local temperature raises over the boiling point, leading to a strong local evaporation of the molten metal, known as a vapor depression zone or keyhole. Simultaneously, the temperature gradient in the melt pool causes the hot liquid to flow towards cooler regions. This is known as the Marangoni effect and, along with the recoil pressure generated in the vapor cavity, it drives the fluid away from the laser beam. As a result, deep and elongated melt pools with a shape that gives name to the melting mode are formed [11], as shown in Fig. 2.3.

In general, the preferred melting mode is the transition point between conduction and keyhole [6, 12, 13]. Such conditions provide sufficient overlap between adjacent melt pools and layer, while avoiding significant evaporation of the material, thereby preventing the formation of defects associated to either lack or excess of energy.

2.1.3. Defects in LPBF-manufactured parts

A multitude of defects and anomalies have been reported and studied in parts produced by LPBF throughout the years [9]. Only the most relevant defects for this work are described in detail below.

Lack-of-fusion (LoF) defects are generated when the energy input and the overlap between adjacent melt pools is insufficient, leaving voids with unmelted powder particles behind. As presented on Fig. 2.4a, such voids are relatively large, possess irregular shapes, and tend to be elongated in a direction perpendicular to BD [14, 15]. Conversely, the keyhole melting mode can result in the formation of keyhole porosity, when the vapor at the bottom of the melt pool collapses and bubbles are trapped. The size of these defects tends to be smaller than LoF pores an their shape is typically spherical [14]. Fig. 2.4b illustrates an example of severe keyhole porosity throughout an LPBF-manufactured part.

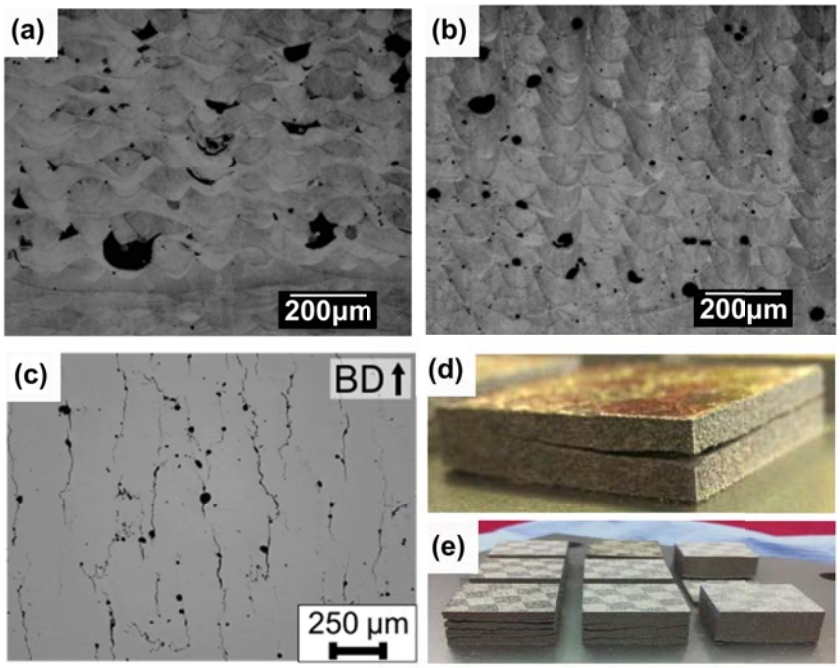

Figure 2.4. (a-c) Optical microscopy images of samples exhibiting different classes of internal defects. (a) Lack of fusion and (b) keyhole porosity on Inconel 625 parts [15]. (c) Internal cracks on $AlMg_{4.5}Mn_{0.7}$ samples[16] (d,e) External cracks on M2 high speed steel specimens [17].

Moreover, there are different mechanisms in the LPBF process that favor crack generation and propagation. Internal cracks often appear within the solidified melt pool (solidification cracking) or at its interface with the heat-affected zone (liquation cracking). Solidification cracks arise from the stresses generated by solidification shrinkage in the center of the melt pool, and are typically oriented parallel to the build direction [18]. Liquation cracks originate from stress-concentration in the partially remelted regions at the boundary of the melt pool, and are oriented perpendicularly to the MP-HAZ interface, i.e. at different angles with respect to the BD [19]. Both of these are considered hot cracking mechanisms, as they take place at temperatures close or above the liquidus temperature of the metal. An example of internal hot cracks is depicted in Fig. 2.4c.

Residual stresses are inevitably created in LPBF-manufactured specimens due to the subsequent shrinkage of the top layers as new material is melted, rapidly cooled and solidified. The repetition of this layer-wise process results in tensile stresses at the edges of the fabricated parts and, depending on the stress intensity and the material properties, cracks can propagate from the edge of the sample into the bulk. This is known as a cold cracking mechanism as it takes place at lower temperatures than the hot cracking events. Two examples of LPBF parts that have undergone external cold-cracking are shown on Fig. 2.4d and Fig. 2.4e. Such cracks

can propagate perpendicularly to the BD, along the plane of printed layers, and can lead to full delamination if they connect with similar cracks from opposite ends of the part.

Many efforts have been placed in mitigating internal defects. For a fixed alloy composition, the selection of processing parameters with the aid of variables as VED, E^* and $\overline{\Delta H}$ has proven to be an effective approach when trying to mitigate porosity [4–6]. Alternatively, cracking can be alleviated by carefully tailoring scanning or post-processing strategies [20].

2.1.4. Common scanning strategies

A schematic of three widely used scanning strategies is provided in Fig. 2.5. The meander scanning strategy (Fig. 2.5a) is likely the most commonly used in the literature. The laser travels from one end of the cross-section to another in a straight path, turning at the edge of the sample and traveling back in the opposite direction. The scan direction of successive layers can be rotated to minimize residual stresses. 67º or 90º are the most common rotation angles between layers [21]. The stripe strategy (Fig. 2.5b) consists in performing meander scans over long stripes that extend from one end to another of the sample. Each of these stripes is a few millimeters wide and is fully scanned by the laser before starting the next. The lines where two stripes come together tend to overlap to ensure no internal defects are generated in these regions. This strategy reduces residual stresses [9, 20]. The chessboard or island strategy (Fig. 2.5c) is similar to the previous one, except that, instead of stripes, squares are independently scanned with a meander path over the cross-section. The scan direction of the vectors within each square is typically offset by 90º with respect to the direction of vectors in adjacent squares. With this approach, residual stresses are partially compensated throughout the cross-section of the part [20, 22].

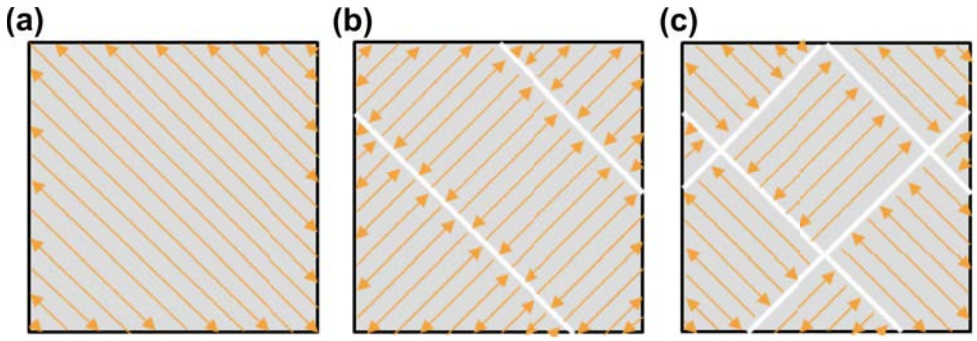

Figure 2.5. Schematic of commonly used scanning strategies. (a) Meander, (b) stripes and (c) chessboard paths.

2.2. Glass-forming alloys

Glass-forming alloys, also known as metallic glasses, amorphous metals or amorphous alloys, are a class of materials that present unique properties due to their lack of long range atomic order [23, 24]. Owing to their disordered atomic arrangement, metallic glasses exhibit excellent corrosion resistance [25], high strength [26, 27], high elastic limit [28], and good damage tolerance [29], and excellent soft magnetic behavior [30]. Widely researched metallic glass systems include Zr, Pd, Ti, and Fe-based among others.

While crystalline materials present an ordered atomic structure, where atoms lie in specific crystal lattice sites, atoms in amorphous metals have a quasi-random arrangement which resembles that of a frozen liquid [31, 32]. Furthermore, the absence of defects such as grain boundaries (GBs) and dislocations gives rise to their unique properties [33]. Fig. 2.6 illustrates the differences in atomic arrangement among single-crystal (Fig. 2.6a), polycrystal (Fig. 2.6b) and amorphous structures (Fig. 2.6c).

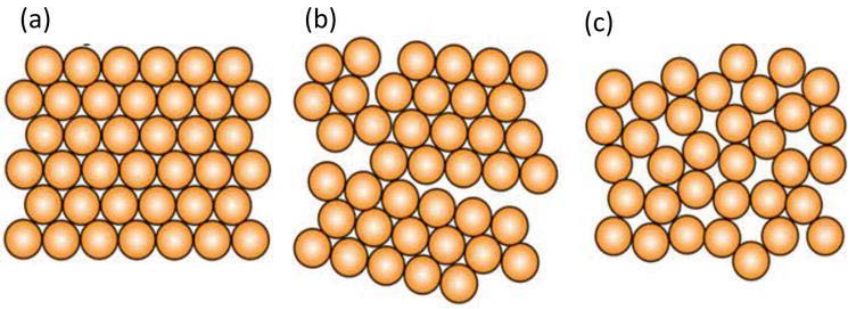

Figure 2.6. Schematic of the atomic arrangement of (a) single crystal, (b) polycrystal and (c) amorphous structure [33].

In order to retain this amorphous or glassy structure, glass-forming alloys must generally be cooled at high cooling rates from the molten state (10^2 – 10^6 K/s, depending on the alloy system) [23, 31]. At the appropriate solidification rates, crystallization kinetics of purposefully designed compositions are usefully sluggish and therefore the atoms are frozen in a disordered metastable arrangement and cannot reach an ordered, more energetically favorable, crystalline structure [34, 35].

2.2.1. Structure of glass-forming alloys

TTT diagram

Glass-forming alloys can crystallize following two different paths. First one, during solidification, as they cool down from the molten state at a rate lower than the critical cooling rate (R_c) of the specific alloy. The second path is known as devitrification, which is the transition from an amorphous solid state to crystalline solid, when the amorphous material is heated above its crystallization temperature (T_x). [32].

The onset of crystallization for a given glass-forming alloy is dependent on the temperature and on the cooling or heating rate [32]. Hence, a time-temperature transformation (TTT) diagram can be constructed for each alloy system, indicating where in the cooling or heating curve crystallization can happen. Fig. 2.7 illustrates a schematic TTT diagram, containing the typical crystallization curve and indicating the liquidus temperature (T_L) and the glass transition temperature (T_g). These three divide the diagram in four regions: The liquid, glassy, crystalline and supercooled liquid regimes. The first three have already been explained. The supercooled liquid region is a regime where the material is in a glassy state but can flow as a viscous liquid. It is in this region that metallic glasses can be molded and residual stresses can be relieved.

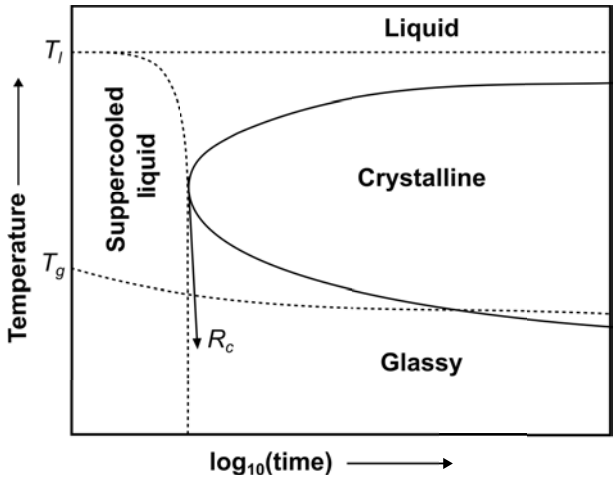

Figure 2.7. Example of a time-temperature-transformation (TTT) diagram. If solidified at a cooling rate higher than the critical cooling rate (R_c), a material will remain amorphous in the solid state and avoid the crystallization nose.

GFA and thermal stability

In the TTT diagram, the nose of the crystallization curve denotes the temperature at which the material will crystallize if it is cooled from the molten state at exactly the critical cooling rate [23]. The longer the time scale for crystallization is for a particular alloy, the lower the critical cooling rate is [24]. The position of the crystalline nose also represents the glass-forming ability (GFA) of a system. A good glass former will exhibit a crystalline nose that is shifted to longer times (further to the right in the TTT diagram), while a poor glass former will, in theory, have a nose position at shorter times (to the left of the diagram). In practice, it is difficult or impossible by current experimental methods to obtain the full TTT curve of poor glass-forming alloys, as the time scales for crystallization are so short that experimental systems cannot reach the heating and cooling rates needed to determine the crystallization nose [32].

The thermal stability of an alloy is also reflected in the TTT diagram. It can be typically estimated by the temperature range of the supercooled liquid region (ΔT_x), which is the difference between the crystallization and glass-transition temperatures ($\Delta T_x = T_x - T_g$), both measured upon heating. An amorphous metal with a high thermal stability will resist nucleation and grain growth as it is heated, hence the crystalline nose will be displaced upwards, towards higher temperatures in the TTT diagram from Fig. 2.7.

Design rules

There has been extensive research in the field since the first synthesis of metallic glasses in 1960 [36]. Many criteria have been proposed to screen potential glass-forming system candidates with improved GFA and thermal stability. Inoue et al. [37] proposed three simple rules, known as the Inoue criteria, based on the structural parameters of the constituent elements. There are systems, however, that do not follow these rules because the GFA is also related to kinetic parameters. Turnbull et al. [38] presented additional criteria for a metallic glass to be formed, which were purely related to kinetic parameters. The following rules are the most widely use criteria in the glass-forming alloy design community, combining Inoue's and Turnbull's criteria [32]:

(i) The system should be composed of at least three different elements, but the formation of glassy structures becomes easier with increasing number of constituents.

(ii) There should be a large difference in atomic size among the elements. It is recommended that the difference exceeds 12 % in atomic radius.

(iii) There should be a negative enthalpy of mixing among the constituents with highest concentrations in the system.

(iv) The composition should show a "deep" eutectic point. This is exhibited when there is a large difference between the eutectic temperature and the melting temperature of the individual elements. It is preferred to design the alloy as close to the eutectic point as possible, as this will give less time for crystallite formation during solidification.

(v) The reduced glass-transition temperature (T_{rg}), the ratio between T_g and T_L, can be used as an indicator of the viscosity of the melt. The higher T_{rg}, the higher the viscosity, and the alloy will be more likely to retain the glassy state upon solidification.

2.2.2. Processing routes

Melt spinning

The first metallic glass, a binary Au-25 %Si system, was synthesized by means of melt spinning [36]. Melt spinning is a technique that consists in melting a metal in a crucible and ejecting it through a fine nozzle using an inert gas to exert the required pressure to create a continuous stream [39]. The stream of molten metal falls onto a cold rotating wheel, quickly solidifying into a continuous ribbon. Such ribbon typically has a thickness of 20-50 μm and a width of several millimeters. The cooling rates achieved with this technique are extremely high, from 10^5 to 10^6 K/s, which make it a reliable method to produce fully amorphous alloys. Nevertheless, due to the geometry of the produced material, it is not feasible to fabricate complex parts by melt spinning.

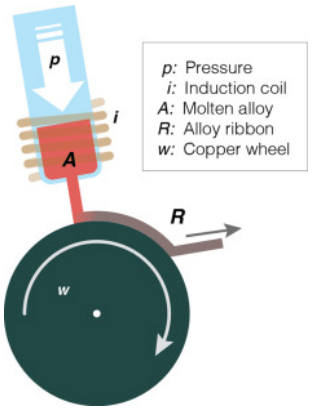

Figure 2.8. Diagram showing the melt spinning process [40].

Casting

Suction casting offers the possibility of producing larger parts, while providing cooling rates ranging from 10 to 10^3 K/s [41–43]. A common setup is comprised of a water-cooled copper plate and a copper mold with an orifice where vacuum is applied to draw the molten metal into the mold [44]. As depicted in Fig. 2.9, the mold is fixed in the center of the water-cooled plate, leaving the inlet at the surface of the copper plate and a channel that connects to the vacuum reservoir in the bottom of the assembly. The alloy is heated above its melting point, typically with an induction or arc melting system. Vacuum is then applied from the inferior orifice of the casting mold and the liquid fills the inner channel.

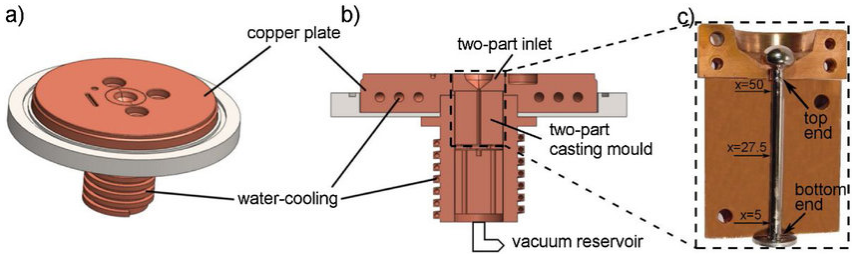

Figure 2.9. Diagram showing a suction casting set up with a water-cooled copper plate [44]. (a) Top view of copper plate; (b) section view of copper plate showing the water cooling system, the material inlet and the outlet where vacuum is applied; (c) section view of a cylindrical mold.

Casting is the preferred method to compare the GFA among alloys [23]. The cooling rate at the inner walls of the mold, which are in contact with the outer surface of the cast sample, is around 10^3 K/s [45], but it decreases through the sample as a function of the distance from the surface [45, 46]. The thickness of the sample will therefore directly affect the cooling rate at the center of the sample's cross-section. For each glass-forming alloy, a critical casting thickness can be determined, beyond which the center of a cast sample will crystallize during

solidification. Generally, the critical casting plate thickness (t_c) and the critical casting rod diameter (d_c) are metrics used to quantify the GFA ability of the system.

When an alloy can retain an amorphous structure by casting with a thickness above 1 mm, the term *bulk* metallic glass is used to indicate the superior GFA over other metallic glasses [23, 47]. Following extensive alloy development research in the last 30 years, bulk metallic glasses have been cast with large dimensions (up to 80 mm) [48]. However, the geometry of cast parts is limited to the shapes of their molds, which thereby restricts the range of applications that cast parts can be used for.

LPBF of metallic glasses

Laser powder bed fusion is a promising avenue to fabricate bulk metallic glasses in the fully amorphous form [49–51]. As explained in Section 2.1, the amount of material that is melted at once in the LPBF process is relatively small. For reference, the width of a scan track is in the order of 100 μm. Therefore, the local cooling rates are usually high enough ($10^5 - 10^7$ K/s) [3] to retain an amorphous structure in the melt pool. Additionally, this technique enables the fabrication of highly complex geometries, unlike the first two methods. A number of BMGs have been produced with LPBF, each system having different properties that make them particularly interesting [24, 31]. Zr-based alloys offer a superior GFA, Al and Ti-based alloys have a high strength to weight ratio, Ni-based alloys offer great corrosion resistance and Fe-based alloys have drawn attention due to their soft-magnetic properties [49].

Despite the aforementioned benefits of LPBF, the technique is known to have limitations, as explained in Section 2.1.3, including the generation of residual stresses and defects, which can impact the final part's properties [9]. An additional challenge with LPBF of metallic glasses is devitrification [52]. This was evident since the first reported metallic glass part printed by LPBF by Pauly et al. in 2013 [53]. The alloy of choice was $Fe_{74}Mo_4P_{10}C_{7.5}B_{2.5}Si_2$ and the geometry, the lattice structure shown in Fig. 2.10. Through x-ray diffraction measurements, it was shown that this printed structure was composed of both amorphous and crystalline phases.

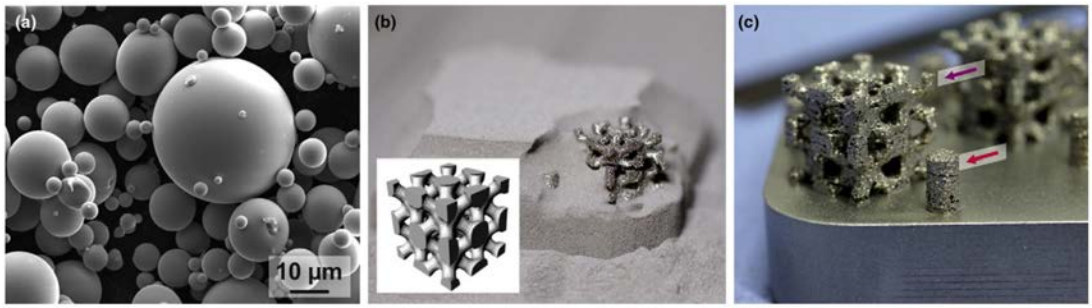

Figure 2.10. First ever reported metallic glass printed by LPBF [53]. (a) SEM image of gas-atomized $Fe_{74}Mo_4P_{10}C_{7.5}B_{2.5}Si_2$ powder; (b) build removal step of LPBF-manufactured samples; (c) final lattice (purple arrow) and cylinder (red arrow).

As explained in Section 2.2.1, devitrification can occur as a solid glass is heated past the crystallization temperature. While a track may remain amorphous after scanning, the subsequent track will reheat the previous one in the overlapping heat affected zone. Thus, new layers can devitrify previously-solidified layers [52]. Section 2.1.2 explains how the preferred melting mode is the transition limit between conduction and keyhole mode. This energy input is high enough to produce highly dense parts. However, a high energy input causes more reheating in the previous tracks and layers, which, in metallic glass parts processing, causes more devitrification. On the other hand, a low energy input is more favorable to retain the amorphous structure after printing but it also creates lack of fusion defects. This is illustrated in Fig. 2.11. The schematic shows, qualitatively, that one should expect an amorphous-crystalline composite when processing metallic glass powders with high energy input combinations of LPBF parameters.

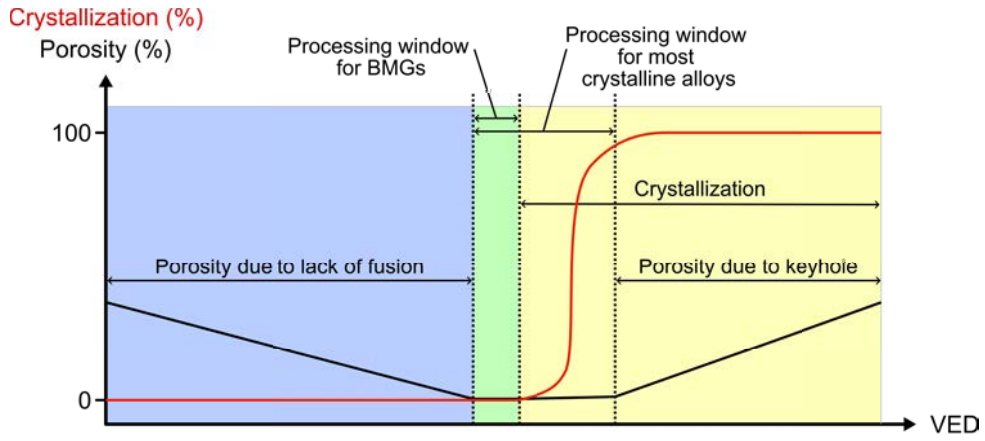

Figure 2.11. Schematic illustrating the processing window of metallic glasses and crystalline alloys as a function of VED.

2.3. Soft Magnetic Materials

2.3.1. Hard vs. soft magnetic materials

Magnetic materials can be divided in two classes, soft magnetic, which are easy to magnetize and demagnetize, and hard magnetic, which are hard to magnetize and demagnetize [54]. When an external magnetic field of alternating polarity is applied to these materials, hysteresis cycles are generated. A schematic example of a hysteresis curve is shown in Fig. 2.12. In magnetism, H_a is used to denote an applied magnetic field and M is used to represent the magnetization within the material [54]. Soft magnetic materials (SMMs) require low H_a to reach their saturation magnetization (M_s), i.e. the state where the M does not increase with increasing H_a. As illustrated on Fig. 2.12, the opposite is true for hard magnetic materials, where a large H_a is needed for the material to reverse their magnetic alignment and reach saturation. The point where the hysteresis curve intersects with the horizontal axis is known as the coercive field or magnetic coercivity (H_c) and it is the measure used to distinguish soft from hard magnetic behavior. Besides their low magnetic coercivity, SMMs possess low magnetic susceptibility (χ), which is reflected in the slope of the hysteresis curve, since $\chi = M/H_a$. A high susceptibility allows the material to reach the saturation state with a small increment of H_a.

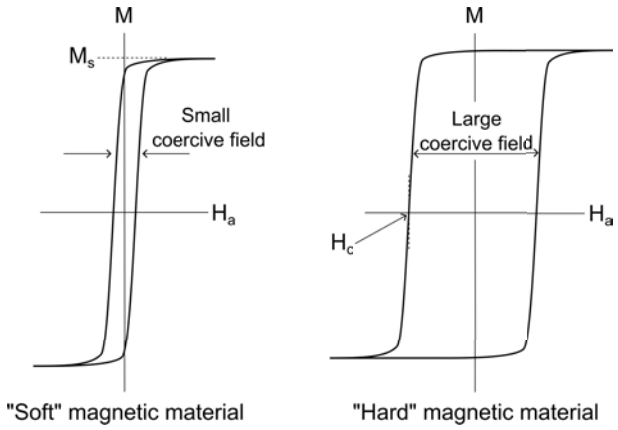

Figure 2.12. Schematic illustrating magnetic hysteresis loops for soft and hard magnetic materials.

2.3.2. Magnetic domain wall movement

The reason why some materials have soft or hard magnetic behavior resides at the microscale. The atoms of ferromagnetic materials are grouped in regions of uniform magnetization, known as magnetic domains [55]. In the absence of an external magnetic field, the sum of

the magnetization of all domains is approximately zero, yielding no net magnetization [54]. This is depicted in Fig. 2.13a. However, when a field is applied to the material, the domains that originally had a orientation close to that of H_a grow at the expense of others, as shown in Fig. 2.13b. This process takes place through the movement of the boundaries between magnetic domains, known as magnetic domain walls. Ultimately, the magnetic direction of the material gets fully aligned with the applied field, if the latter is sufficiently large, through magnetic spin rotation, as illustrated in Fig. 2.13c. After this step, the material reaches M_s, the state presented in Fig. 2.13d, where the magnetic spins of the maximum number atoms are aligned with H_a.

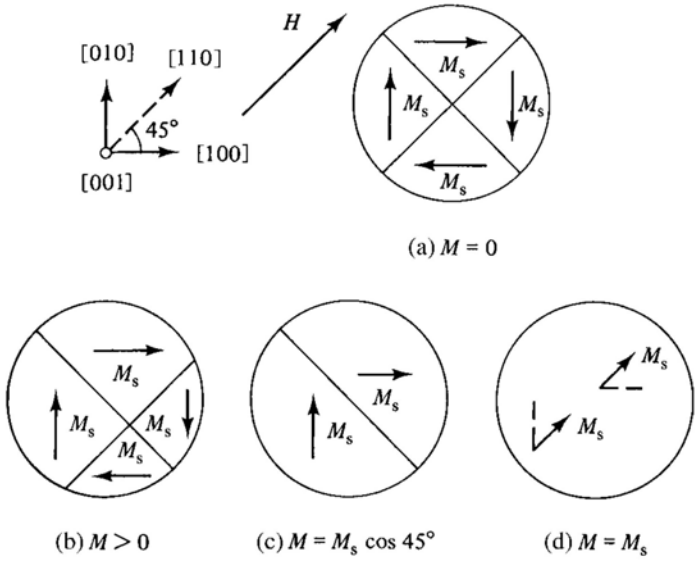

Figure 2.13. Schematic of the magnetization process in a ferromagnet, through domain wall movement [54]. (a) No external field is applied. The net magnetization is zero. (b) An external field is applied and preferentially aligned domains grow at the expense of others through domain wall movement. The material has a net positive magnetization. (c) Magnetic domains finish growing. The internal magnetic field is not fully aligned with H_a. (d) The material reaches saturation magnetization through magnetic spin rotation.

When domain walls can move freely through the material, the magnetization process happens swiftly and M_s is reached at low H_a values. Internal defects like cracks or pores, microsctructural features like grain boundaries, precipitates, and residual stresses can pin the domain wall movement and yield a hard magnetic response [56, 57]. SMMs, on the other hand, typically have few of said obstacles, resulting in a quick response to a changing H_a [58].

2.3.3. Applications and energy losses

Soft magnetic materials are present in widely used modern machines, such as electric motors, generators and transformers, which rely on the quick reversal of magnetic polarity. Electric

motors, for instance, have a rotating component, the rotor, and a stationary one, the stator, which generate the desired movement through attracting and repelling induced magnetic fields [59]. The efficiency of the energy conversion in these machines is directly related to the soft magnetic properties of their components. There are different types of magnetic losses [60, 61], including hysteresis and eddy current losses. In each magnetization cycle, the energy lost to hysteresis losses is equivalent to the area of a hysteresis curve. Hence, SMM's with minimal coercivity are used to maximize the energy efficiency in electric motors [62]. On the other hand, eddy current losses are caused by time-varying magnetic fields, which induce circulating electric current through the conductive material. Such currents form a closed loop and dissipate energy in the form of heat [54]. While hysteresis losses are independent of the frequency of the applied field, eddy current losses scale with the square of the frequency [61, 63].

Traditionally, rotors and stators of electric motors are made out of sheets which are cut and stacked. The material of choice for these components has varied over time and depending on the application. Fig. 2.14 shows a schematic of SMMs according to their typical coercivity values and their year of adoption. Some examples of metals exhibiting soft magnetic behavior include iron alloys such as low carbon or silicon steel, iron-cobalt alloys, and nickel-iron alloys, which are also known as *permalloys* [54, 64]. In the past decades, the emergence of Fe-based amorphous alloys has drawn the attention of the magnetism scientific community, as they can potentially reach lower coercive fields than polycrystalline SMMs [65, 66]. Consequently, amorphous alloys show lower hysteresis losses than their crystalline counterparts [57, 67], making them, in principle, ideal candidates for high-frequency electromagnetic applications where efficiency is the ultimate design criterion.

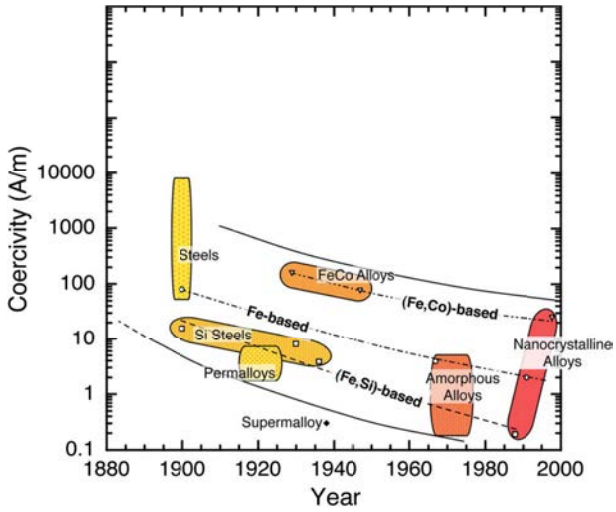

Figure 2.14. Variation of coercivity of different families of soft magnetic materials with respect to the year of first reported values. Adapted from [64].

2.3.4. Soft magnetic metallic glasses

Since first synthesized by Inoue e. al. [30] in 1995, Fe-based BMGs have drawn much attention from the scientific community [31, 37]. When fabricated in the fully amorphous form, they present an excellent soft magnetic behavior, characterized by coercive fields as low as 1 A/m [68, 69], due to the lack of grain boundaries [67]. Additionally, when the system has a high Fe content, the saturation magnetization is high enough to be used for high energy input-output applications. Mechanically, Fe-based metallic glasses are known to exhibit very high strength, hardness, and wear resistance in comparison with their crystalline counterparts [30]. However, the GFA of Fe-based BMGs is relatively low [31], in comparison with that of other MG systems, which limits the practical application of these materials.

Great alloy design advances have been made in the field, searching for compositions that can form large, fully amorphous components. For instance, adding phosphorous to the composition has proven effective to reach d_c of up to 5 mm [70, 71]. However, phosphorus's low boiling point adds difficulty to the alloying process, as P tends to evaporate before other elements are fully melted and small changes in the composition can affect drastically the GFA. Alternatively, the addition of cobalt [72] and rare earth (RE) elements [73, 74] have been shown to increase the d_c to 6 mm and 18 mm, respectively. Although these are constructive advances in the field, the use of critical elements makes the adoption of these compositions unrealistic in a paradigm like that envisioned by the EU Green Deal, where sustainable technological development is paramount. The Fe-based MGs known to date which are free of P, Co and rare earths present $d_c < 0.5$

mm [31] and, thus, cannot be formed into complex-shaped parts. It is clear that alternative manufacturing routes are needed to exploit the potential of these materials and to leverage their outstanding properties for efficient electrical machines. These alloys are the systems of interest within the AM2SoftMag EIC Pathfinder Open project (GA: 101046870), within the framework of which this PhD thesis was carried out.

2.4. State of the art of LPBF of soft magnetic metallic glasses

In the past decade there have been numerous studies on the use of LPBF to fabricating defect-free, fully amorphous Fe-based BMG's with excellent soft magnetic properties. While the vast majority of published works yield parts with amorphous-crystalline composite (micro)structures [53, 75–87], the pioneering work by Jung et al. [84] did report the fabrication XRD-amorphous specimens with composition $Fe_{68.3}C_{6.9}Si_{2.5}B_{6.7}P_{8.7}Cr_{2.3}Mo_{2.5}Al_{2.1}$. This alloy system, owing to the presence of P and to the great number of alloying elements, has a critical casting thickness of approximately 3 mm. This suggests that alloys with high GFA are more likely to resist devitrification during LPBF.

Since the Fe-based alloys of interest for the current thesis, namely those without P, Co or RE elements, have very low GFA, they have not been processed, to date, in a fully amorphous form [76–78, 85–92]. Optimizing LPBF processing parameters for these systems requires carefully tailoring the thermal cycles during the layer-wise manufacturing process. This can be achieved by gaining a fundamental understanding of the effect of the processing parameters on the (micro)structure and, in turn, on the magnetic behavior.

2.4.1. (Micro)structure and soft magnetic behavior

As explained in Section 2.2.2, the reheating cycles inherent to the LPBF process tend to cause devitrification in the heat affected zones of each scan track. Fig. 2.15 depicts the crystallites formed by devitrification in two specimens of a $[(Fe_{0.6}Co_{0.4})_{0.75}B_{0.2}Si_{0.05}]_{96}Nb_4$ alloy manufactured by LPBF with high (Fig. 2.15a, Fig. 2.15c) and low (Fig. 2.15b, Fig. 2.15d) energy input by Luo et al. [79]. These scanning electron microscope (SEM) images show crystalline features on both sample's HAZs, but the reheating experienced by the first, processed with a higher energy, led to severe devitrification, while the latter, processed with a comparatively

lower energy, partially retained the amorphous structure in the MP.

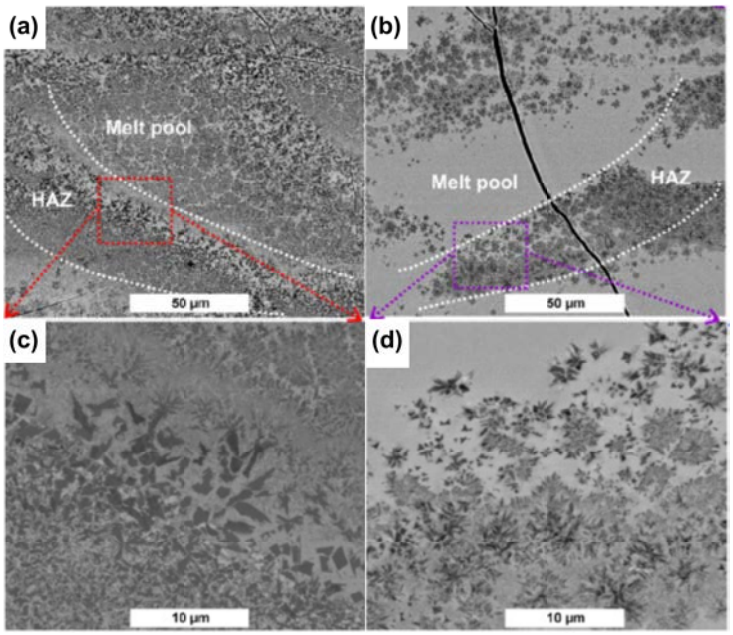

Figure 2.15. SEM images of $[(Fe_{0.6}Co_{0.4})_{0.75}B_{0.2}Si_{0.05}]_{96}Nb_4$ samples processed by LPBF [79]. The images are of two samples with (a,c) relatively high and (b,d) low energy input.

In general, the crystalline phases generated in the HAZ of Fe-based glass-forming alloys when processed by LPBF are reportedly composed of α-Fe [76, 78, 80, 85, 87, 89, 91, 93] and phases containing Fe with one of the other main alloy constituents, such as Si [76, 78, 87, 89], B [76, 78, 89, 91] or C [76, 81]. The size of these grains is usually larger than 100 nm, which, according to Herzer [67], leads to drastic increases in the magnetic coercivity. Several studies [76, 84, 86] have reported that partially crystalline LPBF-processed samples of different Fe-based BMGs exhibit coercive fields that are several orders of magnitude higher than what is typically expected from an amorphous reference of the same composition. In particular, coercive fields over 1000 A/m [76, 85–87] are typically measured in these alloys when printed by LPBF while the corresponding feedstock powder exhibits coercivities around 500 A/m [85] and melt-spun ribbons of similar composition reportedly have coercive fields below 50 A/m [78]. In order to minimize the generation of undesired crystalline phases and to maximize the retention of the amorphous structure, low-energy input parameter combinations like high scan speed or low laser power, are typically used [82], at the expense of the part density.

2.4.2. Internal defects and mechanical properties

While low-energy processing parameters provide the desirable conditions to avoid crystallization (low temperatures and high cooling rates), this inevitably leads to the generation of internal defects, such as LoF voids [77, 81, 82, 84, 93] and internal cracks [77–79, 81, 83, 93, 94]. Jiang et al. [77] and Nong et al. [93] studied the effect of LPBF processing parameters on the defect structure of $Fe_{54}Cr_{18.5}Mn_2Mo_{14}W_6B_3C_1Si_{1.5}$ [wt.%] systems. Two micrographs from said studies are presented in Fig. 2.16, exemplifying the typical distribution of internal defects that can be found when manufacturing Fe-based metallic glass parts by LPBF.

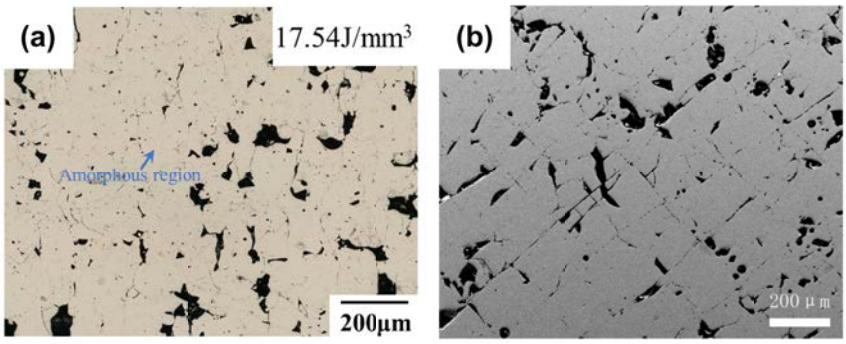

Figure 2.16. Internal pores and cracks along the cross-section of LPBF-processed $Fe_{54}Cr_{18.5}Mn_2Mo_{14}W_6B_3C_1Si_{1.5}$ [wt.%]. (a) Optical micrograph from [77]. (b) SEM image from [93].

Fe-based glass-forming alloys tend to be brittle and susceptible to cracking during LPBF processing. Works by Jiang et al. [77] and Xie et al.[80] have investigated the origin of these cracks and concluded that they originate at the interface of the MP and HAZ [79], and pores [95] which act as stress concentration points. When crystalline HAZ are formed, cracks tend to propagate along the grain boundaries of α-Fe grains [95, 96].

It is known that internal defects directly affect the mechanical properties of the material [3, 9]. The high concentration of internal defects typically observed in LPBF-manufactured Fe-based metallic glasses promote the propagation of cracks and the failure of a part when subjected to a load. Few works have been carried out on the mechanical properties of these materials, with the exception of hardness and nanoindentation studies which neglect the influence of internal defects [76–78, 93, 96, 97]. Although the enhancement of the soft magnetic properties is the main goal in this research, it is paramount to understand the effect of internal defects on the multi-scale mechanical properties of these alloys, given that any electric motor or generator part will be subjected to mechanical loads during assembly and operation.

2.4.3. Advanced scanning strategies

Several research groups have put forward novel scanning strategies to mitigate devitrification and the generation of internal defects in Fe-based metallic glass parts produced by LPBF. Nam et al. [85] used a double-scanning approach where, for every layer of powder, the laser would melt the surface twice. This proved to be a successful strategy to achieve denser prints with slightly improved amorphous fraction with respect to single-scan parameters [85]. Zou et al. [92] also employed a remelting strategy with the chessboard pattern explained in Section 2.1.4. A diagram of this strategy is displayed on Fig. 2.17a. By limiting the scan track length within each island, cracking of the top surface was mitigated on 100-μm-tall samples [92]. However, when reproduced by Jiang et al. [77] on 1-cm-tall samples of a similar alloy, the material was severely cracked. Zrodowski et al. [89] proposed the point-random strategy, which consisted of, first, depositing a layer of powder (Fig. 2.17b1), then melting the powder using the chessboard strategy (Fig. 2.17b2) and remelting the surface using randomly placed points (Fig. 2.17b3) until entire cross-section is remelted (Fig. 2.17b4). By keeping the spacing between subsequent points relatively large, enhanced heat dissipation was achieved. Although the point-random approach did not prevent crack formation, it led to a significant improvement of the amorphous fraction and the soft magnetic properties of printed parts. The downside from this strategy, besides the increase in build time from re-melting, is that most commercial LPBF systems do not allow for such a strategy to be easily implemented.

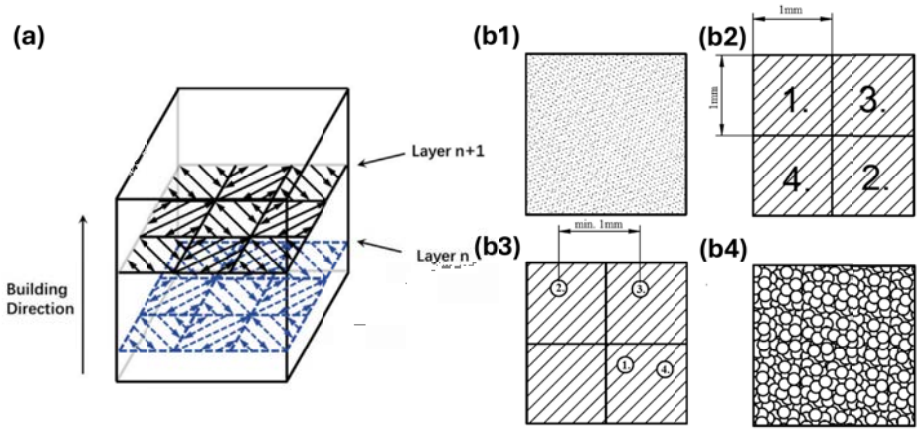

Figure 2.17. (a) Remelting chessboards strategy from [77]. (b1-4) Point-Random strategy from [89].

It is evident that advanced scanning strategies are necessary to fully exploit the soft magnetic potential of some of the most challenging Fe-based glass-forming alloys, including those without P, Co, and RE elements. Easily implemented strategies should be further investigated,

and their impact on internal defects, (micro)structure and properties should be understood.

Ultimately, the viability of implementing soft magnetic metallic glass components fabricated by LPBF in electrical machine components resides in the intersection between alloy systems with high GFA and carefully selected processing parameters and scanning strategies. In order to be aligned with the EU Green Deal and contribute to a sustainable technological development, new alloys must be free of critical elements such as P, Co or rare earths. Furthermore, the interplay between processing parameters and the generation of internal defects, (micro)structure and soft magnetic properties must be thoroughly investigated.

3. MATERIALS AND METHODS

3.1. Feedstock powder

Two Fe-based glass-forming powder alloys with different composition were used as feedstock material throughout this thesis. The first is a commercial alloy known as Kuamet 6B2 with composition $Fe_{73.7}B_{11}Si_{11}Cr_{2.3}C_2$ [at. %]. The second system's exact composition remains confidential, as it is subject to patenting by the Chair of Metallic Materials at the University of Saarland. This alloy will be referred to as Fe-Si-B-Nb-Ni throughout this work. They were both atomized by Epson Atmix by means of spinning water atomization (SWAP) [98]. The powder was handled and stored in small containers while working in a glovebox with an argon atmosphere to limit oxidation.

Prior to LPBF processing, the morphology and rheological properties of the feedstock powder particles were evaluated. An Apreo 2S (ThermoFisher Scientific) field emission gun scanning electron microscopy (FEG-SEM) system was used to image the powder particles. Fig. 3.1 presents SEM images of both powder batches, which show particles with good spheroidicity and almost no satellites attached. The particle size distribution (PSD) was measured using a Bettersize laser particle size analyser. The results of these tests are summarized in Table 3.1. Both powder batches presented similar PSDs, although the Fe-Si-B-Nb-Ni batch had a slightly wider distribution with a higher volume of large particles, represented by the D_{90} value.

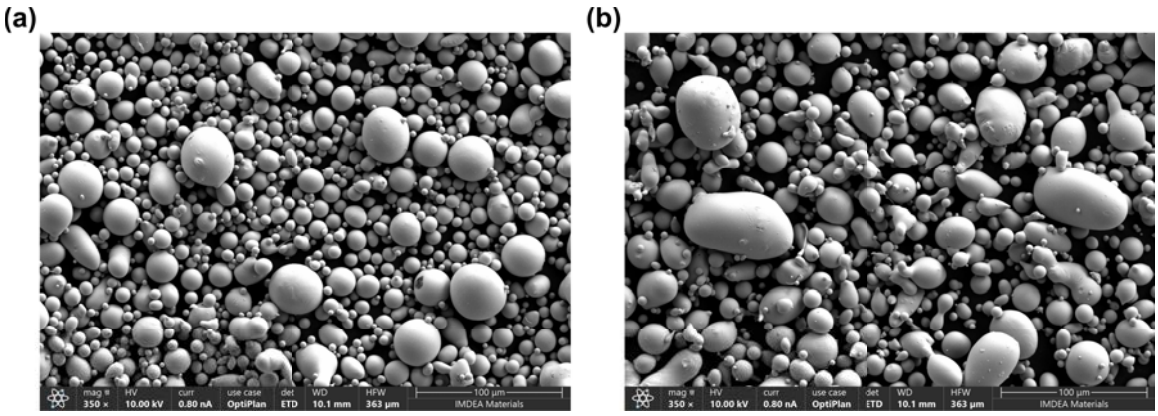

Figure 3.1. SEM micrograph illustrating the spinning water-atomized (a) Kuamet 6B2 powder and (b) Fe-Si-B-Nb-Ni. The images were obtained using the secondary electron (SE) signal.

The rheological properties such as flowability, apparent density (ρ_a) and tapped density (ρ_t) were evaluated using standard ASTM methods (ASTM B213 [99] and ASTM B527 [100]). The results are summarized in Table 3.2. The flow time was calculated as an average of three measurements on a Hall flowmeter. Kuamet 6B2 averaged a flow time of 23.4 s for a 50 g powder sample. Fe-Si-B-Nb-Ni powders, however, did not flow uninterruptedly through the apparatus. From the apparent and tapped density measurements the Carr Index (CI = $\rho_a(1/\rho_a - 1/\rho_t) \times 100$) and the Hausner Ratio (HR = ρ_t/ρ_a), which are also indicators of powder flow character [101], were calculated. The CI and HR values suggest *excellent* flowability for the Kuamet 6B2 powder, and *good* flowability for the Fe-Si-B-Nb-Ni batch. Ultimately, the spread of both powder batches in the LPBF system was adequate for printing trials.

Table 3.1. Particle size distribution values for two feedstock powder batches used for LPBF trials.

	D_{10} µm	D_{50} µm	D_{90} µm
Kuamet 6B2	11	30	61
Fe-Si-B-Nb-Ni	12	33	68

Table 3.2. Comparison of Kuamet 6B2 and A112 powder flow properties (flow time; apparent density, ρ_a; tapped density, ρ_t; Carr Index, CI; and Hausner Ratio, HR) with flow character evaluation from [101].

	Flow time (s)	ρ_a (g/cm^3)	ρ_t (g/cm^3)	CI	HR	Flow character
Kuamet 6B2	23.4	4.03	4.27	5.62	1.06	Excellent
Fe-Si-B-Nb-Ni	N/A	3.87	4.49	13.8	1.16	Good

3.2. Experimental Methods

3.2.1. Laser Powder Bed Fusion

The two LPBF systems used in this work are shown in Fig. 3.2. The first is the Renishaw AM400 (Fig. 3.2a), a machine that uses a 400 W pulsed-wave ytterbium fiber laser with a spot size of 70 µm. The second system is the Renishaw RenAM500Q Flex (Fig. 3.2b), which is equipped with four 500 W Yb-fiber lasers with a 80 µm spot size. Both machines were operated using pulsed-wave emission mode and reduced build volume (RBV) platforms furnished with 316L steel substrates were utilized to minimize powder waste. As explained in Section 2.1.1, due to the pulsed nature of the lasers, v was be modified throughout this work by changing the exposure time (t_{ON}), as expressed in Eq. (2.1).

Figure 3.2. Laser powder bed fusion systems used in this work. (a) AM400; (b) RenAM500Q.

The most relevant difference between the two systems used for LPBF tests is the capability that the RenAM500Q Flex has to apply variable time delays at the end of each scan track, a processing parameter that will be paramount for the work presented in Chapter 6 and Chapter 7. Therefore, the AM400 machine was dedicated to studies with simple scanning strategies, like the ones used in Chapter 4 and Chapter 5, while the RenAM500Q Flex was employed for advanced approaches, like those presented in Chapter 6 and Chapter 7.

In-operando infrared emission measurements were carried out with Renishaw's RenAM500Q built-in photo-diode. Fig. 3.3 shows a diagram of the integrated InifniAM Spectral system. The utilized sensor is part of the MeltVIEW module and is calibrated to record emissions of wavelengths between 1100 – 2000 nm, which are associated to the thermal emissions of the melt pool. Data post-processing was carried out using Renishaw's InfiniAM Spectral software and MATLAB.

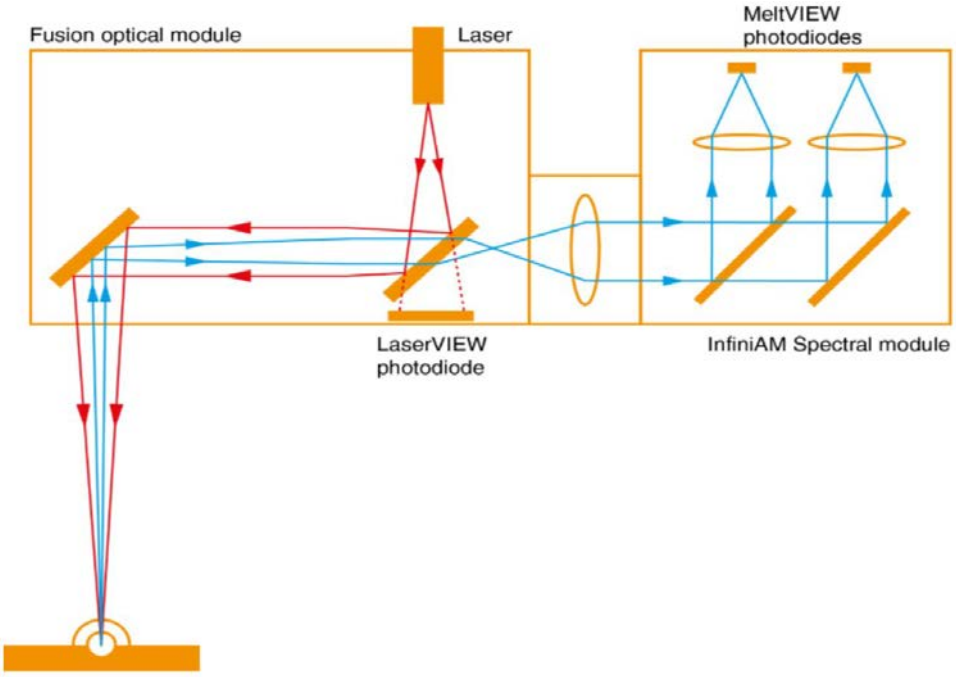

Figure 3.3. Schematic provided by Renishaw plc detailing the working principle of the InfiniAM Spectral module.

3.2.2. Sample preparation

The same sample preparation procedure was followed for most samples presented in this work. After LPBF processing, specimens were first removed from the substrate plate and then they were sectioned in two halves along a plane parallel to the BD with a Struers Secotom-20 disc cutting machine. One half was generally used to measure density, to analyze defects, and for (micro)structural examination. The newly cut surface was ground with sandpaper of grit sizes ranging from 300 to 2400 and polished with diamond pastes of sizes decreasing from 9 μm to 1 μm, followed by chemical-polishing with a 0.04 μm colloidal silica suspension to achieve a mirror-like surface finish. The melt-pool geometry was examined in selected samples additionally etched using a 10:10:1 solution of 98 % ethanol, distilled water, and 65 % nitric acid. Etching was carried out by immersion during 15 s followed by water rinsing. The remaining halves of the cut samples were used for magnetic characterization and calorimetry studies.

3.2.3. Defect analysis

The density of LPBF-printed samples was measured via the Archimedes method using a BEL Engineering density kit. Furthermore, internal defects were studied in two and three di-

mensions dimensions by optical microscopy (OM) and X-ray computed tomography (XCT), respectively. An Olympus BX51 optical microscope was used to image the mirror-polished cross-sections. Images were taken at 5x magnification and stitched together to cover the entire sample's cross-section. A Waygate Technologies Phoenix Nanotom M was employed to obtain 3D tomography volumes of uncut samples. Measurements were performed using a beam voltage of 130 kV, current of 60 μA, voxel size of 3 μm and exposure time of 0.5 s, resulting in 2000 projections per sample. 2D and 3D defects were reconstructed and analyzed with ImageJ/Fiji image analysis software. In particular, Fiji's machine learning-assisted segmentation plug-in, the WEKA trainable segmentation package [102], was used to segment the obtained images or volumes into binary data structures containing information about one defect class. An example of the workflow followed on a 2D image is illustrated on Fig. 3.4. First, the image (Fig. 3.4a) is converted into binarized images of voids (Fig. 3.4b) and cracks (Fig. 3.4c).

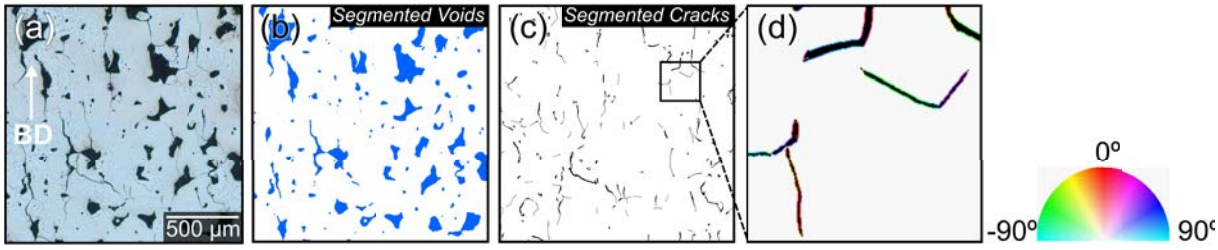

Figure 3.4. Schematic illustrating the workflow of the machine-learning based image segmentation procedure utilized for defect characterization. (a) Optical micrograph illustrating, in black, the defect structure; (b) binarized image of voids (including small and large pores), shown in blue; (c) binarized image of cracks; (d) color coding for the angular deviation of cracks with respect to the BD (0°).

Voids were indexed via Fiji's particle analyzer plug-in and later filtered based on size. Filtering is done by setting an area threshold of 2500 pixels, which allows to isolate small circular pores resulting from keyhole effects and from trapped gas (named "small pores" in Chapter 4) from large and irregularly shaped ones, which are attributed to lack of fusion (LoF) effects (named "large pores" in Chapter 4 and type-1 voids in Chapter 5). Internal cracks are also isolated (Fig. 3.4c) and their area fraction can be also estimated. Finally, Fiji's directionality plug-in is utilized on 2D images to analyze the angular deviation (θ) of cracks with respect to BD (which is parallel to the vertical direction in the figure). In Fig. 3.4d the cracks have been colored according to their θ angle following the color coding included in the inset.

3.2.4. Microstructure characterization

X-ray diffraction (XRD) was carried out in a Malvern PANalytical Empyrean X-ray diffractometer using Cu Kα radiation to evaluate qualitatively the phase distribution on the LPBF-manufactured parts. A 3x3x1 mm^3 piece was cut from each printed sample to evaluate the fraction of amorphous phase by differential scanning calorimetry (DSC) in a Perkin Elmer DSC8000 system. A constant heating rate of 20 K/s was applied and the obtained DSC curve was integrated to obtain the crystallization enthalpy of each sample $\Delta H_{cr,sample}$. The same procedure was applied to a fully amorphous melt-spun ribbon of the same composition to be used as reference. The amorphous fraction of each LPBF-manufactured specimen was then calculated by taking the ratio of the crystallization enthalpy of each sample to that of the amorphous ribbon ($AM\% = \Delta H_{cr,sample}/\Delta H_{cr,ribbon}$).

Microtexture analyses were conducted using an Apreo 2S (ThermoFisher Scientific) field emission gun scanning electron microscope (FEG-SEM) equipped with an Oxford Instruments electron backscattered diffraction (EBSD) detector, a CCD camera, and the Aztec data acquisition and analysis software package. EBSD maps of the crystalline regions were acquired using 20 kV, a current of 3.2 nA, a working distance of 13 mm, and a step size of 120 nm for low magnification maps or, alternatively, a step size of 30 nm for high magnification maps.

A FEI Helios NanoLab 600i FEGSEM equipped with a focused ion beam (FIB) milling system was employed to extract transmission electron microscopy (TEM) lamellae from selected LPBF-processed specimens. An area of 15 μm × 1.5 μm was covered with a Pt-layer to protect it from milling. The long side of this rectangle was aligned with the BD of the sample. Next, a trench was milled on each side of the Pt layer, using an accelerating voltage of 30 kV and a beam current of 9.3 nA. A micro-manipulator was attached to the Pt-covered edge, and a U-cut was performed to detach the lamella from the rest of the sample. The lamella was transported to a Cu-grid and was then thinned by progressively lowering the beam current from 2.5 nA to 41 pA, while the accelerating voltage was kept at 30 kV, except for the final thinning step, where it was reduced to 5 kV. TEM investigation was carried out on a FEI Image-corrected Titan equipped with a CETOR and Cs DCOR aberration correction lenses. Maps were obtained in high resolution TEM mode with an accelerating voltage of 300 kV and a spot size of 3. A fast Fourier transform (FFT) was applied to TEM images to search for the presence of crystalline phases using the Fiji/ImageJ FFT tool. Atom probe tomography (APT) was conducted for se-

lected samples. The APT specimens were prepared from site-specific lift-outs from the center of polished samples. In particular, the lift-outs were performed using a dual-beam focused-ion beam FEI Helios G4 following procedures described in [103]. The APT specimens were analyzed using a Cameca LEAP 5000XS instrument operating at 60 pJ laser energy, 333 kHz, and 50 K. The commercial package AP Suite 6.3.1 was used for data reconstruction and analysis.

3.2.5. Magnetic properties

Hysteresis loops were measured at room temperature for all LPBF-manufactured samples using a LakeShore vibrating sample magnetometer (VSM) by applying a DC magnetic field in the range of ± 800 kA/m. The coercive field (H_c) was evaluated for each sample from the hysteresis loop after the subtraction of the sample holder's diamagnetic contribution.

3.2.6. Mechanical properties

Micromechanical nanoindentation tests were carried out on selected pecimens. Areas of 120 × 70 μm were indented with a Hynstron Triboindenter TI 950 using a step size of 1.2 μm and a maximum load of 5 mN. The reduced modulus (E_r), measured by the instrument, was converted to E using the following formula:

$$E = (1 - \nu^2)\left(\frac{1}{E_r} - \frac{1 - \nu_i^2}{E_i}\right)^{-1} \tag{3.1}$$

where ν is the material's Poisson ratio (approximately 0.28) and E_i and ν_i are the elastic modulus and Poisson's ratio of the instrument, respectively. Three cyclic load tests were performed and the instrument compliance was adjusted to ensure that the measured hardness and reduced modulus remained constant across all load cycles. Following this calibration step, values for E_i and ν_i were found to be 1141 GPa and 0.07, respectively.

3.3. Numerical Methods

3.3.1. Thermo-metallurgical model

A thermo-metallurgical finite element method (FEM)-based simulation of the LPBF process is carried out to understand the effect of time delays on the (micro)structure of the Kuamet 6B2 manufactured samples. The thermal model is similar to the one described in [104]. The evolution of temperature in the LPBF-manufactured parts (domain) is computed by solving the heat transfer equation:

$$\rho c_p \frac{\partial T}{\partial t} = \nabla \cdot (k \nabla T) + Q_l + Q_\phi \tag{3.2}$$

where ρ is the density, c_p is the specific heat capacity, k is the isotropic conductivity, T is the temperature, t is the time, Q_l is the absorbed heat due to the laser incidence, and Q_ϕ is the absorbed/released heat due to melting/solidification. The laser source contribution (Q_l) is computed as [105]:

$$Q_l = \alpha_p \frac{G_l I_z}{H_l} \tag{3.3}$$

(2)

where α_p is the laser absorptivity, $G_l = \dfrac{2P}{\pi\phi^2} \exp\left(-\dfrac{2((x-x_l)^2 + (y-y_l)^2)}{\phi^2}\right)$ is the Gaussian distribution at the irradiated surface, $I_z = \dfrac{1}{0.75}\left[-2.25\left(\dfrac{z_l - z}{H_l}\right)^2 + 1.5\left(\dfrac{z_l - z}{H_l}\right) + 0.75\right]$ is a parabolic decay along the laser penetration direction, H_l is the laser penetration depth, P is the laser power, ϕ is the diameter of the laser spot, and (x_l, y_l) are the coordinates of center of the laser spot that irradiates the surface located at z_l, referred to the Cartesian coordinate system (x, y, z).

The contribution Q_ϕ in Eq. (3.3) is computed by taking into account the latent heat involved in melting/solidification as $Q_\phi = \rho L_f \dfrac{\partial f_s}{\partial t}$, where L_f is the latent heat of fusion and f_s is the solid volume fraction that is computed by the metallurgical model. The applied boundary conditions are given by Newton's law $q_c = -h_c(T - T_\infty)$, where q_c is the normal heat flux, h_c is the interfacial heat transfer coefficient, and T_∞ is the temperature of the environment.

Based on the temperature profile and history predicted from the thermal model described above, a simple metallurgical model is applied to qualitatively assess the formation of crystalline

regions. Whenever a region is melted, i.e. when the local temperature exceeds the alloy liquidus temperature (T_L), the resulting default state from the fast cooling is considered to be considered fully amorphous, since the critical casting thickness is approximately 150 μm, i.e., around the width of a printed track, and the cooling rate of LPBF (10^5–10^7 K/s) [82] is substantially higher than that typical of casting processes (10–10^3 K/s) [3].

Hence, it is assumed that any crystalline region is purely the result of solid-state devitrification within a relevant temperature range, comprised between the crystallization and the solidus (T_S) temperatures. The temperature range for devitrification is calibrated to experimental data, and the residence time between T_x and T_S (τ) can be directly correlated to the extent and location of crystalline phases. The proposed model is implemented into the Abaqus finite element software by programming Fortran user subroutines, using the SoftGLASS plug-in [106]. The equations are solved on a discretized domain, which allows to compute the temperature and phase evolutions into the whole geometry.

3.3.2. Model parameters

The 3D simulations are performed in a domain consisting of a previously deposited bulk substrate. The thermal and material properties used to perform the simulations are summarized in Table 3.3, Table 3.4 and Table 3.5. α_p and H_l were calibrated to get a good match between the measured and simulated melt pool sizes. The material's thermal properties (c_p, L_f, T_S and T_L) were obtained through differential thermal analysis on a NETZSCH STA 449 Jupiter system. The c_p in the liquid phase is assumed equal to that of pure Fe at the melting temperature [107] due to the lack of data on the alloy under investigation. The values of c_p are summarized in Table 3.4. The thermal conductivity (k) is assumed equal to that of pure Fe due also to the lack of data [107]. The variation of k with temperature is summarized in Table 3.5.

Table 3.3. Thermal and material parameters used for simulations.

ρ Bulk material (kg/m^3)	α_p	H_l (µm)	h_c Top domain surface ($W/m^2/°C$)	h_c Bottom domain surface ($W/m^2/°C$)	L_f (J/kg)	T_∞ ($°C$)	T_S ($°C$)	T_L ($°C$)
7200	0.6	62	50 [104]	500 [104]	272000	25	1050	1150

Table 3.4. Specific heat capacity as a function of temperature.

$T(°C)$	$T \leq T_S$ (solid state)	$T \leq T_L$ (liquid state)
$c_p(J/kg/°C)$	527	761

Table 3.5. Thermal conductivity of the bulk material as a function of temperature [107].

$T(°C)$	20	100	200	400	600	800	927	1050	1055	1050
$k(W/m/°C)$	73.3	68.2	61.5	48.6	38.9	29.7	29.7	34	33	33

4. PROCESSING, (MICRO)STRUCTURE, AND PROPERTIES OF THE COMMERCIAL FE-SI-B-CR-C (KUAMET 6B2) ALLOY

4.1. Background

The Fe-Si-B-Cr-C system has drawn special interest for its remarkable soft magnetic behavior, the relatively large availability of its elements and the absence of rare earths or elements with high social and environmental cost, such as Co. To date there is very limited information regarding the LPBF processability of this alloy class, as only a handful of studies have been published on this topic [78, 85–87, 89]. Furthermore, these studies utilize different alloy compositions within the Fe-Si-B-Cr-C system, as well as various LPBF machines, and thus it is not straightforward to extract basic processing-structure-property relations that can be transferred to a wide range of alloy/machine combinations. In Section 2.4, recent literature works were discussed where complex scanning strategies have been put forward to favor heat dissipation [85, 89]. However, the large number of LPBF parameters to be optimized, which are often not fully disclosed, as well as the limited information regarding the crystalline/amorphous composite structures formed, together with the complexity of the scan strategies proposed, obscure the fundamental knowledge underlying LPBF processing of the mentioned Fe-based glass-forming alloys.

This chapter aims to build a solid relationship between the LPBF processing parameters, the corresponding (micro)structure and the magnetic properties of the commercial Fe-based Kuamet 6B2 metallic glass using a simple scanning strategy. With that goal, the material under investigation was additively manufactured using a wide array of process parameter combinations and a meander scanning strategy. In particular, critical processing parameters, including the laser power, the scan speed, and the hatch distance were varied over a large range of values. Several complementary characterization techniques were then utilized to assess the defect structure, the fraction of amorphous material, and the (micro)structure of the crystalline regions of the printed parts. The latter was then related to the corresponding magnetic properties, including the saturation magnetization and the coercivity. The associated electrical losses are also discussed. This study aims to provide guidelines to leverage LPBF AM methods to produce

soft magnetic Fe-based BMG components.

4.2. Methods

4.2.1. LPBF processing parameters

Simple prism samples of $8 \times 8 \times 9.5$ mm^3 in size were fabricated in two different printing campaigns to study the relationship between the processing parameters, the generated (micro)structure and the corresponding soft magnetic properties. The selected scanning strategy was always meander, with a rotation in the scanning direction of 67º between subsequent layers. The first LPBF processing campaign (Print 1) was aimed at studying the influence of P and v while all other parameters were kept constant. The hatch distance was fixed at 80 μm and t at 30 μm (equivalent to the D_{50} particle size). P was varied between 20 and 60 W. Due to the pulsed nature of the laser, v was modified by keeping pd fixed at 80 μm and varying the exposure time (t_{ON}) between 350 and 650 mm/s. The processing parameter combinations probed in Print 1 are depicted in Fig. 4.1 and are summarized in Table 4.1. A total of 14 LPBF parameter sets (samples KS1-KS14) were explored. The volumetric energy density (VED) is also included in Table 4.1 for reference. The second LPBF processing campaign (Print 2) was aimed at investigating the influence of h. In particular, four parameter sets including the extreme P and v values of Print 1 (KS1 (20 W, 350 mm/s, VED = 23 J/mm^3), KS3 (20 W, 650 mm/s, VED = 12 J/mm^3), KS11 (50 W, 350 mm/s, VED = 59 J/mm^3), and KS13 (50 W, 650 mm/s, VED = 32 J/mm^3), were selected, and, for each of them, h was varied between 50, 70, and 90 μm. Since KS3 lead to a combination of extremely low VED, the highest h value (90 μm) was not attempted on this combination of parameters. Fig. 4.1b-d depicts the parameter sets that were probed in Print 2, which are also summarized in Table 4.1. A total of 11 LPBF parameter combinations (KS15-KS25) were tested in the second campaign.

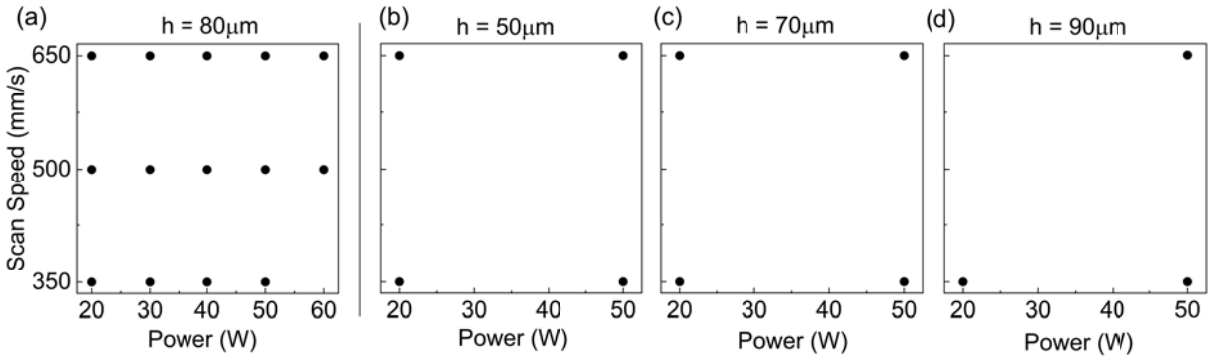

Figure 4.1. Processing parameter combinations corresponding to (a) print 1 (KS1-KS14) and (b-d) print 2 (KS15-K25).

Table 4.1. Relative density, area fraction of different defect types, and amorphous fraction of Kuamet 6B2 additively manufactured samples.

Sample Name	*P* (W)	*v* (mm/s)	*h* (μm)	VED (J/mm^3)	Relative Density (%)	Small voids (%)	Large Voids (%)	Cracks (%)	AM % (%)
					Print 1				
KS1	20	350	80	23	88.8	0.9	7.7	2.6	17
KS2	20	500	80	16	85.6	1.0	10.6	2.8	25
KS3	20	650	80	12	74.3	0.8	23.0	1.8	35
KS4	30	350	80	35	88.5	1.3	7.5	2.7	18
KS5	30	500	80	25	80.5	1.4	15.6	3.0	32
KS6	30	650	80	19	68.8	1.0	27.6	2.6	42
KS7	40	350	80	47	88.1	0.9	8.4	2.6	11
KS8	40	500	80	33	82.9	0.9	3.8	2.3	30
KS9	40	650	80	25	73.7	1.0	23.1	2.3	46
KS10	60	500	80	50	92.5	0.8	4.4	2.3	21
KS11	50	350	80	59	93.1	0.7	3.5	2.7	20
KS12	50	500	80	41	90.0	0.9	6.5	2.6	25
KS13	50	650	80	32	85.8	0.9	10.8	2.4	21
KS14	60	650	80	38	81.1	1.0	15.4	2.4	34
					Print 2				
KS15	20	350	50	38	90.8	0.6	6.5	2.1	10
KS16	20	350	70	27	91.1	0.7	5.8	2.4	14
KS17	20	350	90	21	89.4	0.9	7.4	2.2	24
KS18	20	650	50	26	85.2	0.8	12.1	2.0	27
KS19	20	650	70	19	75.2	0.7	22.2	1.8	36
KS20	50	350	50	95	91.8	0.6	5.4	2.2	3
KS21	50	350	70	68	92.0	0.6	5.1	2.3	11
KS22	50	350	90	53	92.9	0.7	4.0	2.4	18
KS23	50	650	50	67	87.1	0.8	9.9	2.2	24
KS24	50	650	70	48	81.4	1.0	15.7	2.0	36
KS25	50	650	90	37	76.6	1.0	20.6	1.7	42

4.3. Results

4.3.1. Effect of LPBF processing parameters on the defect structure

Fig. 4.2 illustrates the defect structure along a cross-section parallel to BD in all samples manufactured within prints 1 (KS1-KS14) and 2 (KS15-KS25). The corresponding density values, along with the area fraction of small pores, large pores, and cracks, are included in Table 4.1. The area fraction of small voids generated by trapped gas or by keyhole effects is small (around 1 %) irrespective of the processing parameters. Conversely, the area fraction of large voids, originated by lack of fusion of the feedstock powder, ranges from 3.5 to 27.6 % and it depends strongly on the processing conditions. Finally, the area fraction of cracks ranges from 1.7 % to 3.0 % within the processing window investigated in the present study. Fig. 4.3 is a color map illustrating the variation of the density of the LPBF manufactured parts with respect to the processing parameters for samples manufactured within prints 1 (Fig. 4.3a) and 2 (Fig. 4.3b-d). The actual measurements have been plotted using solid black dots and color coding has been utilized to build the map by interpolation of the measured data. It can be seen that, for a fixed value of the hatch distance, the density increases when using processing conditions that combine high power and low scan speed. The difference between the maximum and minimum density values obtained for each h increases with increasing hatch distance. Overall, the highest density (93.1 %) was achieved in sample KS11 (P = 50 W, v = 350 mm/s, h = 80 μm) and the lowest (68.8 %) was detected in sample KS6 (P = 30 W, v = 650 mm/s, h = 80 μm).

Fig. 4.4 illustrates the orientation of the cracks in sample KS1, measured using the image analysis tool described in Fig. 3.4. The angle θ represents the inclination of each crack with respect to BD. Cracks lie preferentially at θ angles that are symmetric with respect to the build direction. In particular, higher frequencies of cracks appear at θ values of approximately ±0°, ±5°, ±15°, ±20°, ±25°, ±45°, ±50°, ±70°, and 90°. Comparatively, the frequency of cracks at said orientations is slightly higher for the negative θ values than in their positive counterpart with the exceptions of ±5° and ±20°, where the frequency is roughly the same on both sides of the histogram. Examination of the crack orientation in all processed samples yielded identical results.

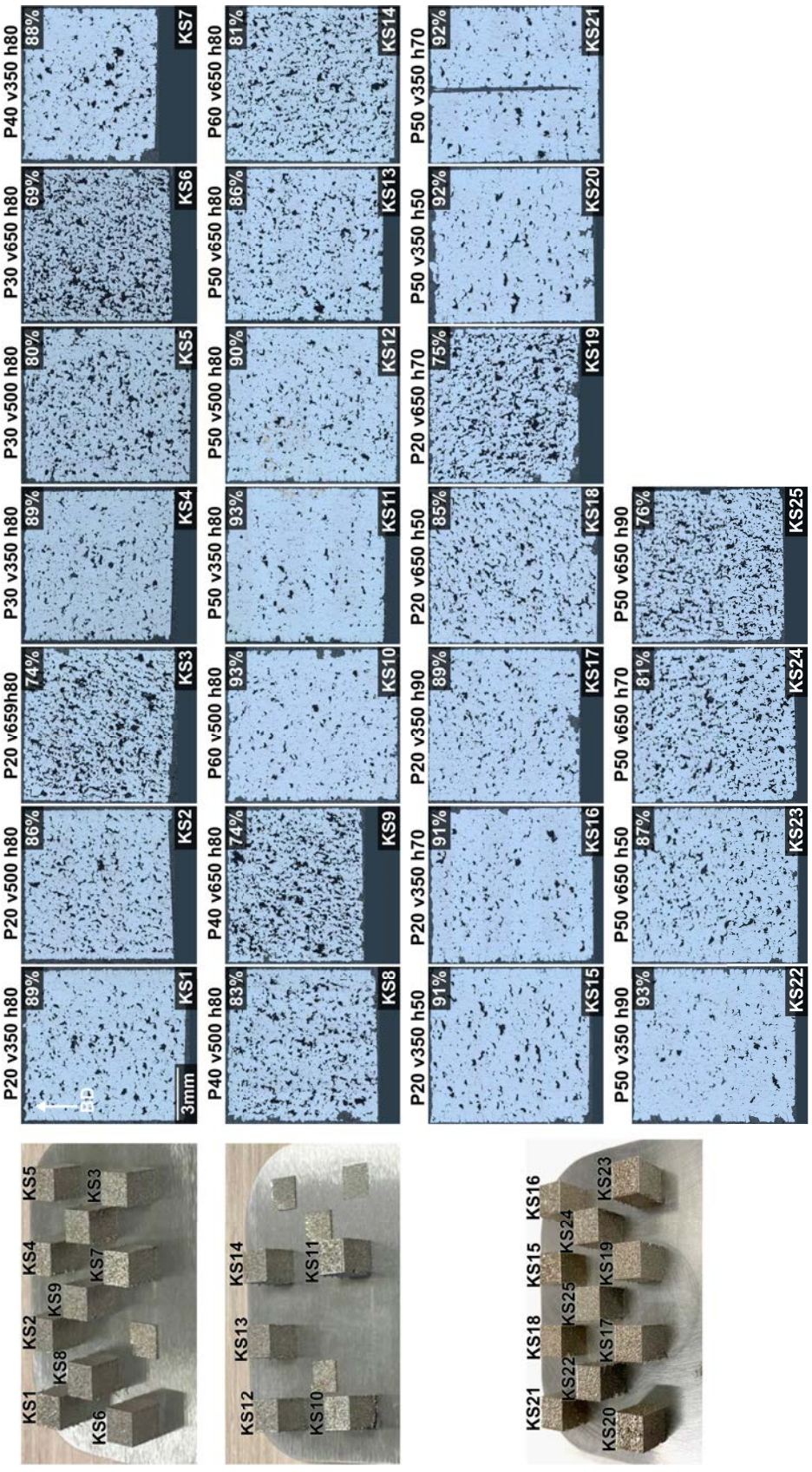

Figure 4.2. As-built prisms manufactured within print 1 (KS1-KS14) and print 2 (KS15-KS25) as well as the corresponding optical micrographs illustrating the defect structure along a cross-section parallel to the BD. The density values estimated by image analysis have been included as insets on the top right corner of each image.

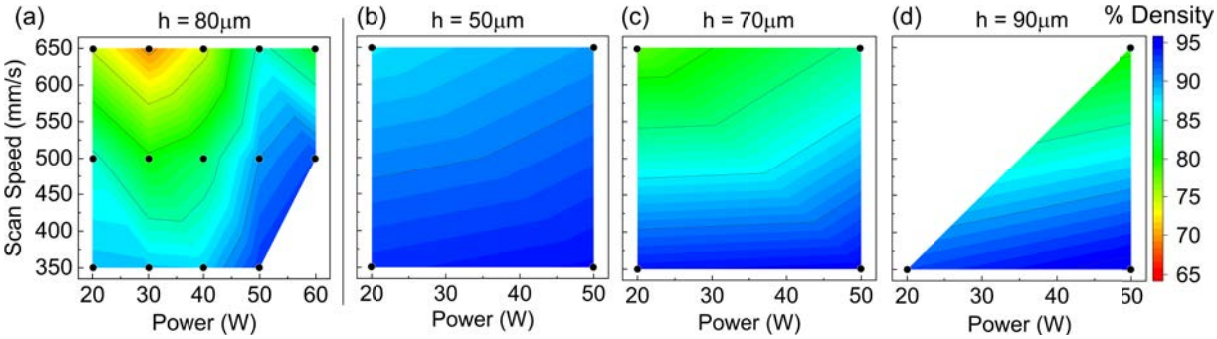

Figure 4.3. Color maps illustrating the variation of the density of the LPBF manufactured parts as a function of the processing parameters. (a) Print 1; (b) print 2, h = 50 μm; (c) print 2, h = 70 μm; (d) print 2, h = 90 μm. The solid black dots indicate the actual measurements. The maps have been constructed by interpolation.

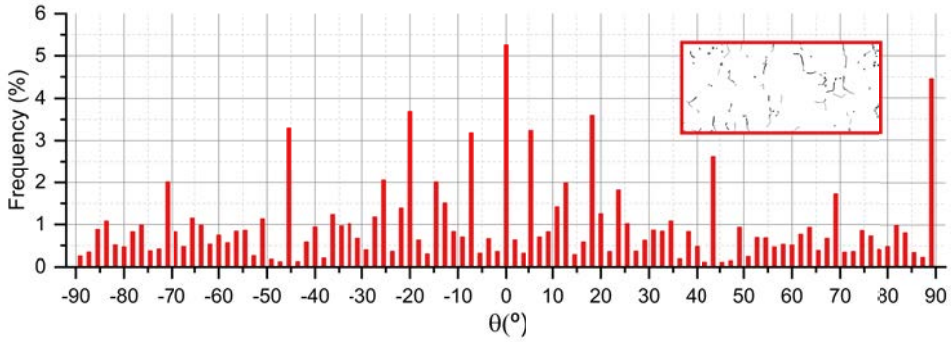

Figure 4.4. Histogram representing the orientation of cracks with respect to the BD on sample KS1.

4.3.2. Effect of LPBF processing parameters on crystallization

Irrespective of the processing conditions, a two-phase (amorphous/crystalline) structure was obtained following LPBF processing of the Kuamet 6B2 alloy under investigation. Fig. 4.5 compares the XRD patterns corresponding to all the samples processed using the conditions included in prints 1 and 2 with that of a reference fully amorphous Kuamet 6B2 melt-spun ribbon and with that of spinning water atomized powders with the same alloy composition. The ribbon exhibits an amorphous hump at diffraction angles comprised between 40º and 50º, in the absence of any distinct diffraction peaks. The powder pattern is formed by the superposition of a very similar hump with a small intensity peak at 45º. The latter might be attributed to either α-Fe or Fe_3Si, as these two phases cannot be unambiguously distinguished by XRD [108]. The XRD patterns from all printed samples, however, show a slight amorphous hump located at the same diffraction angle as the ribbons and the powder, as well as pronounced superimposed peaks, which may be attributed to the presence of the α-Fe/Fe_3Si and Fe_2B phases, which are known to be formed during the solidification of Fe-Si-B MGs [108, 109]. The presence of an amorphous/crystalline composite-like structure following LPBF of this alloy is consistent with

earlier reports [88]. XRD did not reveal the presence of oxides.

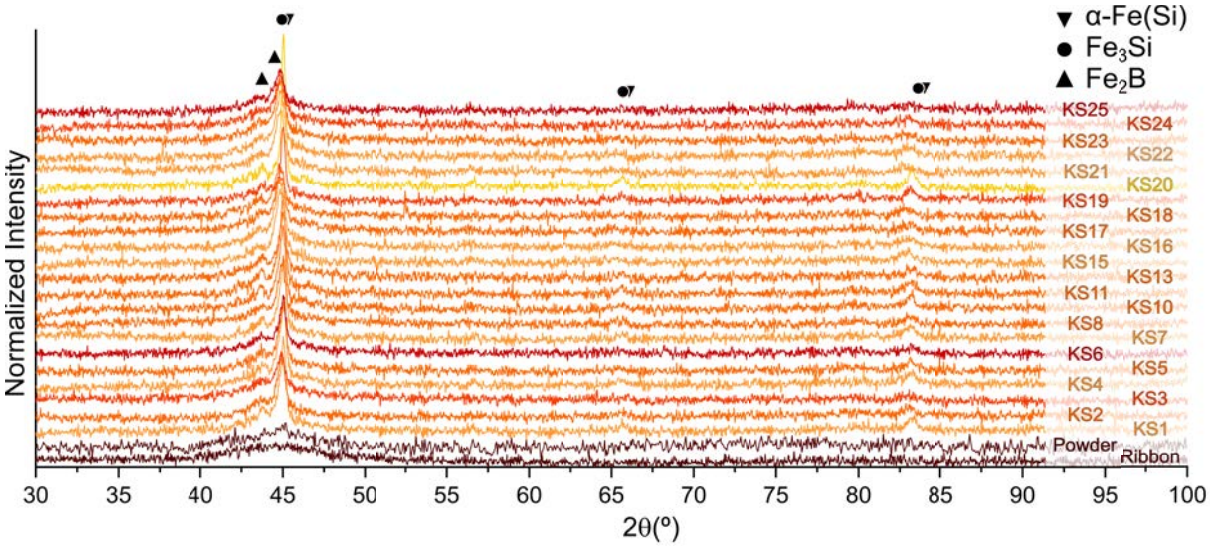

Figure 4.5. Comparison of the XRD patterns corresponding to the Kuamet 6B2 samples fabricated using the parameter sets included in prints 1 (KS1-14) and 2 (KS15-25) with those of reference melt-spun ribbons and of gas atomized powder with the same alloy composition.

The spatial distribution of the amorphous and crystalline phases is, qualitatively, similar for all LPBF parameter combinations investigated (KS1-KS25). As an example, Fig. 4.6 provides a qualitative view of the amorphous and crystalline regions in an etched cross-section parallel to the BD in sample KS7. The amorphous phase appears with light contrast, while areas populated by crystallites appear as brown regions, as they are selectively corroded during etching. The top layer in Fig. 4.6 is populated by melt pools containing a much larger fraction of amorphous phase than those present at the interior of the printed sample. This confirms that crystallization does not take place preferentially during solidification but that it occurs on the HAZ as a consequence of the overlap between neighboring tracks or between consecutive layers. Indeed, it can be clearly seen in Fig. 4.6 that crystalline regions are predominantly located both at the left-hand side of melt pools (HAZ of neighboring tracks) and at the bottom of melt pools (HAZ of subsequent layers). The thickness of the corroded regions, i.e., the degree of crystallization, was found to be highly dependent on the parameter combination used. Further quantification of crystallization is provided below.

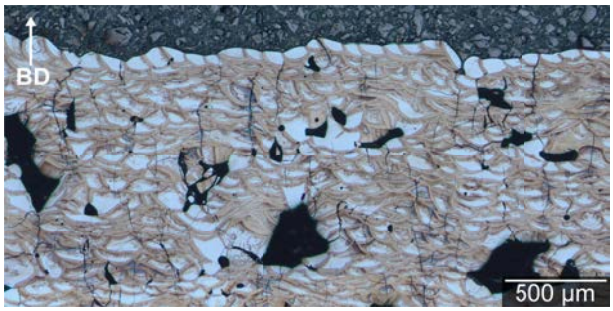

Figure 4.6. Optical image of an etched cross-section parallel to the BD in sample KS7. The amorphous phase appears with light contrast, while areas populated by crystallites appear as darker regions, as they are selectively corroded during etching. In the top layer the tracks are perpendicular to the imaged cross-section.

Fig. 4.7 includes several color maps illustrating the variation of the fraction of the amorphous phase, measured by DSC, as a function of the processing parameters for samples processed within prints 1 (Fig. 4.7a) and 2 (Fig. 4.7b-d). The actual measurements have been plotted using solid black dots and color coding has been utilized to build the map by interpolation of the measured data. The amorphous fraction values corresponding to each processing condition investigated are listed in Table 4.1. For a fixed value of the hatch distance, the fraction of the amorphous phase increases when using processing conditions that combine low power and high scan speed. In particular, the largest value (46 %) was measured on sample KS9 (P = 40 W, v = 650 mm/s, h = 80 µm) and the lowest value (3 %) was found on sample KS20 (P = 50 W, v = 350 mm/s, h = 50 µm). The difference between the maximum and the minimum fractions of amorphous phase obtained for each hatch distance increases as h increases from 50 to 90 µm. Comparison of Figs. 4.3 and 4.7 reveals that amorphous fraction decreases when LPBF is carried out under conditions for which the density increases. Such inverse relationship between amorphous fraction and the relative density, which also applies to other BMGs processed by LPBF [49–51], represents a critical challenge for LPBF process optimization of Kuamet 6B2.

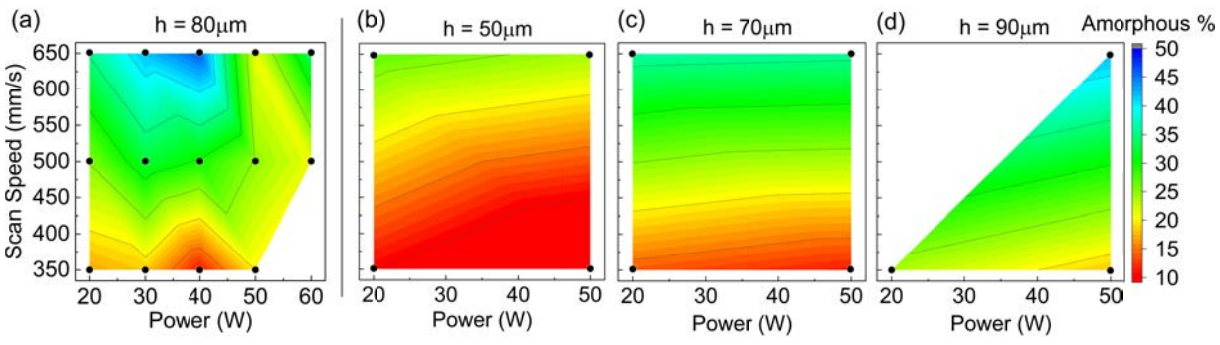

Figure 4.7. Color maps illustrating the variation of the amorphous fraction, measured by DSC, in the LPBF-manufactured samples as a function of the processing parameters. (a) Print 1; (b) print 2, h = 50 µm; (c) print 2, h = 70 µm; d) print 2, h = 90 µm.

In Fig. 4.8 the amorphous fraction values are related to the processing parameters (P,v,h) for all samples manufactured within prints 1 (KS1-KS14) and 2 (KS16-KS26). The results are grouped by hatch distance (black dashed rectangles with rounded corners). Yellow, orange, and red squares correspond, respectively, to v = 350 mm/s, 500 mm/s, and 650 mm/s. Fig. 4.8 reveals that, irrespective of h, for a given v, changing P from 20 to 50-60 W has a relatively small influence on amorphous fraction whereas for a fixed P, increasing v from 350 to 650 mm/s leads to a significant increase in amorphous fraction. As explained in Section 2.1.1, v was modified by altering the laser exposure time while keeping the point distance constant. Thus, the data of Fig. 4.8 reveal that altering the exposure time of the pulsed laser has a stronger influence on amorphous fraction than changing P.

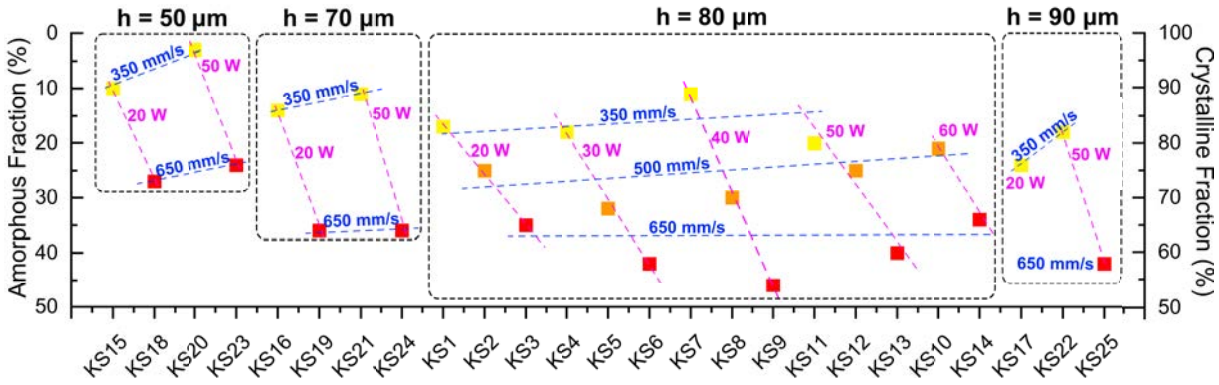

Figure 4.8. Amorphous fraction of all samples processed within prints 1 (KS1-14) and 2 (KS15-25) as a function of the LPBF processing parameters. The results are grouped by h (black dashed rectangles with rounded corners). Yellow, orange, and red squares correspond, respectively, to v = 350 mm/s, 500 mm/s, and 650 mm/s.

The (micro)structure and the microtexture within crystalline regions were examined by SEM and EBSD and were found to be similar for all processing conditions. As an example, Fig. 4.9 illustrates the (micro)structure of two samples processed with very different parameters: KS19, with P = 20 W, v = 650 mm/s, and VED = 10 J/mm^3 (Fig. 4.9a-c) and KS20, with P = 50 W, v = 350 mm/s, and VED = 95 J/mm^3 Fig. 4.9d-f). Fig. 4.9a and Fig. 4.9d are SEM micrographs obtained in the SE mode in which several cracks traversing melt pools can be appreciated. Fig. 4.9b and Fig. 4.9e are EBSD phase maps in which α-Fe/Fe_3Si crystallites are colored in red, $Fe_{23}B_6$ grains are colored in blue, and Fe_2B crystals are colored in green, while dark areas are zero-solutions, associated to amorphous or nano-crystalline regions with sizes below the instrument's resolution. Finally, Fig. 4.9c and Fig. 4.9f are EBSD IPF maps in the BD in which grains are colored following the color coding included as an inset. Fig. 4.9c and Fig. 4.9f also contain the corresponding inverse pole figures illustrating the orientation of the

BD. Fig. 4.9 confirmed, first, that crystalline regions are preferentially located at the perimeter of melt pools, as was inferred from the etched optical micrograph of Fig. 4.6. Second, the EBSD phase maps of Fig. 4.9b and Fig. 4.9d reveal that the largest fraction of crystallites corresponds to the α-Fe/Fe_3Si phases (colored in red), which can not be distinguished unambiguously by this technique due to the similarity between the crystalline lattice parameters of the two phases [108]. Third, the fraction of borides (colored in blue and green) seems to be higher in the sample processed with a lower energy density (KS19) (Fig. 4.9b). Fourth, crystalline regions are formed by randomly oriented, mostly equiaxed grains, with sizes under 4 μm (Fig. 4.9c and Fig. 4.9f). The largest grains are found at the bottom of melt-pools, while ultra-fine and nanocrystalline grains with sizes under 1 μm tend to be dispersed within amorphous regions at the melt-pool cores.

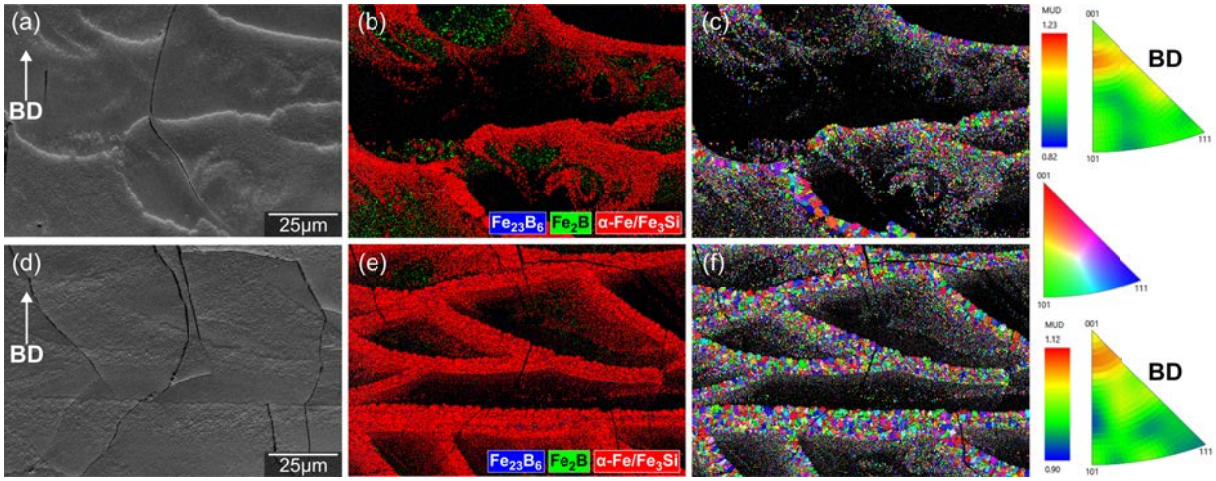

Figure 4.9. (Micro)structure and microtexture within crystalline regions in LPBF processed Kuamet 6B2 KS19 (a-c) and KS20 (d-f) samples. a, d) Secondary electron SEM images; b, e) EBSD phase maps; c, f) EBSD IPF maps in the BD and the corresponding inverse pole figures illustrating the direction of BD.

4.3.3. Magnetic properties

Room temperature hysteresis loops of all printed samples, of the feedstock powder and of the melt-spun ribbon were measured. A representative selection of $M(H_a)$ curves is shown in Fig. 4.10. The ribbon shows the typical $M(H_a)$ curve of a soft magnetic material characterized by a fully amorphous (micro)structure, i.e., a regime of full saturation achieved at a low magnetic field that reverses in a narrow magnetic field range. As a result, a high magnetic susceptibility (the slope of M curve with increasing H_a) and a very low coercive field (lower than the sensitivity of VSM, as shown in the inset) are measured. Conversely, the magnetization reversal process of the $M(H_a)$ curves for the printed samples and for the powder takes place over

a wider magnetic field interval with a reduce magnetic susceptibility. These characteristics are compatible with the reduction of the amorphous fraction observed in these samples compared to the as-quenched ribbon. The crystalline phase would hinder the movement of the domain walls affecting both the magnetic field strength needed to reach saturation as well as the values of saturation magnetization and coercivity (the latter is now detectable by VSM, as shown in the inset). Finally, while the magnetization process measured in the powder displays almost the same susceptibility value as the printed samples, the coercivity is lower due to the presence of a higher fraction of the amorphous phase.

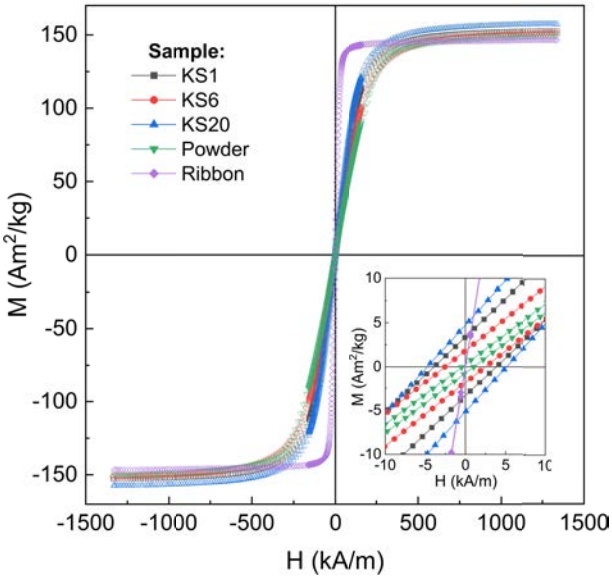

Figure 4.10. Room-temperature hysteresis loops of selected printed samples, of the feedstock powder, and of melt-spun ribbon. An enlarged view of the of $M(H_a)$ curves at low magnetic field is shown as an inset.

Fig. 4.11a depicts the saturation mass magnetization, M_s, of the samples manufactured within prints 1 and 2 (blue squares) as a function of the amorphous fraction (estimated by DSC measurements). The M_s values corresponding to the feedstock powder (149 Am^2/kg, yellow triangle) and to a fully amorphous ribbon (147 Am^2/kg, red circle) are included in the plot for reference. M_s decreases slightly as the amorphous fraction increases. As the Fe content is the same in all samples independently on the synthesis process, the M_s, which is an intrinsic property of the alloy, is expected to be the same in all measured samples. The reduction of M_s with increasing amorphous fraction observed in Fig. 4.11a is ascribed to a lower magnetic moment of the amorphous Fe-based alloy phases with respect to that of the Fe-based crystalline phases [110]. Fig. 4.11b shows the coercive field (H_c) of all samples processed within prints 1 and 2 as a function of the corresponding amorphous fraction (estimated by DSC measurements).

The values corresponding to the feedstock powder (amorphous fraction of 82 %) and to a fully amorphous ribbon are included in the plot for reference. It is evident that, overall, the coercivity decreases as amorphous fraction increases. Indeed, the lowest coercive field (H_c = 2.5 kA/m) was measured on sample KS6, with one of the highest amorphous fractions (42 %), while the highest coercive field (H_c = 5.0 kA/m) was measured on sample KS21, in which the amorphous fraction is rather low (11 %). Irrespective of the printing conditions, H_c in the LPBF-processed samples is three orders of magnitude higher than in the amorphous ribbon, which confirms that crystallization severely hinders the soft magnetic response. Microstructural parameters such as the average grain size do not appear to have a significant influence on H_c.

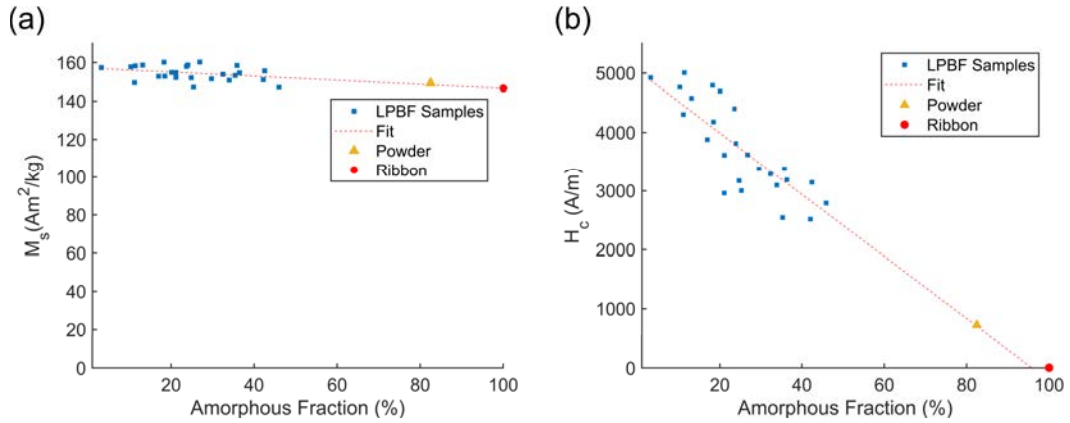

Figure 4.11. (a) Saturation mass magnetization (M_s) and (b) coercive field (H_c) as a function of the amorphous fraction. Blue squares represent the LPBF manufactured samples (prints 1 and 2). The values corresponding to the feedstock powder (yellow triangle) and melt-spun, fully amorphous, ribbon (red circle) of the same composition are included as a reference.

In Fig. 4.12 the H_c values are related to the processing parameters (P,v,h) for all samples manufactured within prints 1 (KS1-KS14) and 2 (KS15-KS25). The results are grouped by hatch distance (black dashed rectangles). Yellow, orange, and red squares correspond, respectively, to v = 350 mm/s, 500 mm/s, and 650 mm/s. The H_c value of a fully amorphous melt-spun ribbon (6.2 A/m) has been added as a reference. It is apparent that, for a given v, changing P from 20 to 50-60 W has a minor influence on H_c, whereas for a fixed P, increasing v from 350 to 650 mm/s leads to a significant reduction of H_c. Moreover, when h is increased from 50 to 90 μm, the said impact of the scanning speed on H_c is further accentuated. As explained in Chapter 3, v was modified by altering the laser exposure time while keeping the point distance constant. Thus, the data of Fig. 4.12 reveal that altering the exposure time of the pulsed laser has a stronger influence on H_c than changing P (within the ranges investigated). Comparison of Fig. 4.12 with Fig. 4.8 confirms that the strong effect of v on H_c can be directly related to the similarly strong effect of v on the amorphous fraction.

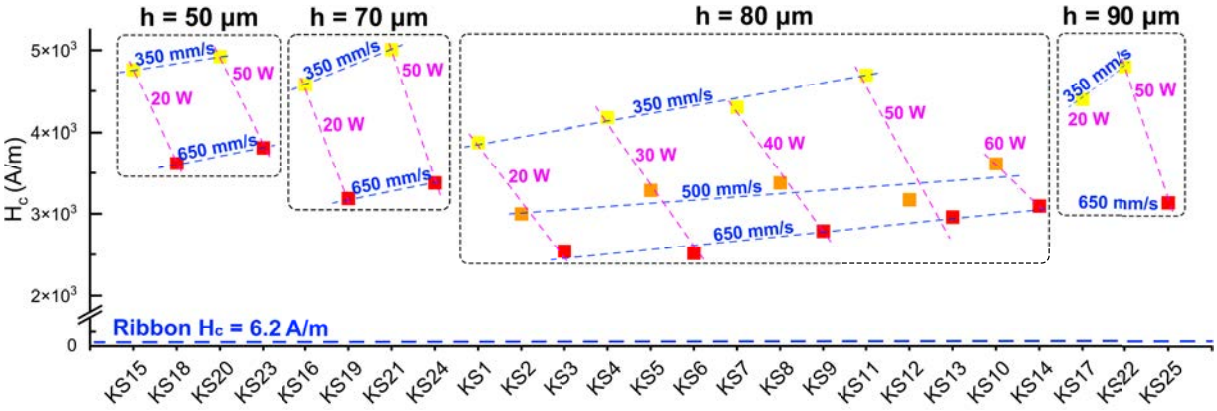

Figure 4.12. Coercive field (H_c) of all samples processed within prints 1 (KS1-14) and 2 (KS15-25) as a function of the LPBF processing parameters. The results are grouped by hatch distance (black dashed rectangles). Yellow, orange, and red squares correspond, respectively, to v= 350 mm/s, 500 mm/s, and 650 mm/s. The value corresponding to a fully amorphous melt-spun ribbon is presented as reference.

4.4. Discussion

4.4.1. Analysis of crack propagation

Optimization of LPBF of Fe-based BMGs for soft-magnetic applications requires a thorough understanding of crack nucleation and propagation mechanisms. Earlier works on LPBF of Fe-based BMGs have reported that crack nucleation takes place preferentially at pores [93], as they act as stress concentration points, or at the junction of crystalline and amorphous regions [79, 96] owing to the local stresses generated by the different volume shrinkage of the two phases during solidification. Comparatively less work has been carried out on the analysis of crack propagation paths. Our research shows that cracking is present in all the LPBF-processed Kuamet 6B2 samples, irrespective of the processing conditions, and that the area fraction occupied by cracks remains always between 1.8 and 3 % (Table 4.1). Fig. 4.4 shows that cracks propagate preferentially at θ values of approximately $\pm 0°$, $\pm 5°$, $\pm 15°$, $\pm 20°$, $\pm 25°$, $\pm 45°$, $\pm 50°$, $\pm 70°$, and $90°$ with respect to BD. In Fig. 4.13 we relate the orientation of crack propagation paths to the morphology of the crystalline regions. The latter is "quantified" by measuring the orientation of the directions perpendicular to the facets of crystalline/amorphous interfaces (normal directions, NDs) as described in Fig. 4.13a-d. In particular, the distribution of inclination angles of all the NDs with respect to BD (θ') was analyzed by segmenting optical micrographs of etched surfaces (Fig. 4.13a) into amorphous (Fig. 4.13b) and crystalline (Fig. 4.13c) as described in Chapter 3. In Fig. 4.13d the facets along the crystalline/amorphous interfaces have been colored according to their θ' angle following the color coding included in the inset. Fig. 4.13e com-

pares the θ (red bars, data from Fig. 4.4) and θ' (blue bars) distributions in sample KS1. Both distributions are remarkably similar, with almost overlapping high frequency peaks, thereby confirming that cracks propagate preferentially along directions that are perpendicular to the crystalline/amorphous interfaces. Moreover, the amorphous/crystalline interfaces show higher frequencies at positive angles than their negative counterparts, which is the opposite that was observed for the crack orientations, further confirming that cracks preferentially grow perpendicular to the crystalline/amorphous interfaces. The difference in frequency observed on both sides of the histograms can be explained by the overlap of adjacent tracks, which generate crystalline HAZ's that are asymmetric about the BD (Fig. 4.6 and Fig. 4.8). This phenomenon was observed on several Kuamet 6B2 samples processed using widely different sets of LPBF processing parameters (KS1, KS16-KS26). These results suggest that crack propagation is mainly dependent on the melt pool geometry and on the degree of periodic overlap of crystalline regions following LPBF processing [77, 79, 96].

Goodall et al. [111] have recently reported how altering crack propagation paths in a Fe-Si steel processed by LPBF can be a very useful tool to increase the resistance in the planes in which eddy currents circulate, thereby reducing energy losses. They succeeded to control crack density and crack propagation paths by tuning the LPBF processing parameters and the scanning strategy. Our data suggest that controlling melt pool shapes and sizes, and thus the corresponding HAZ, may constitute a useful tool to design crack propagation paths in LPBF-manufactured Fe-based BMGs.

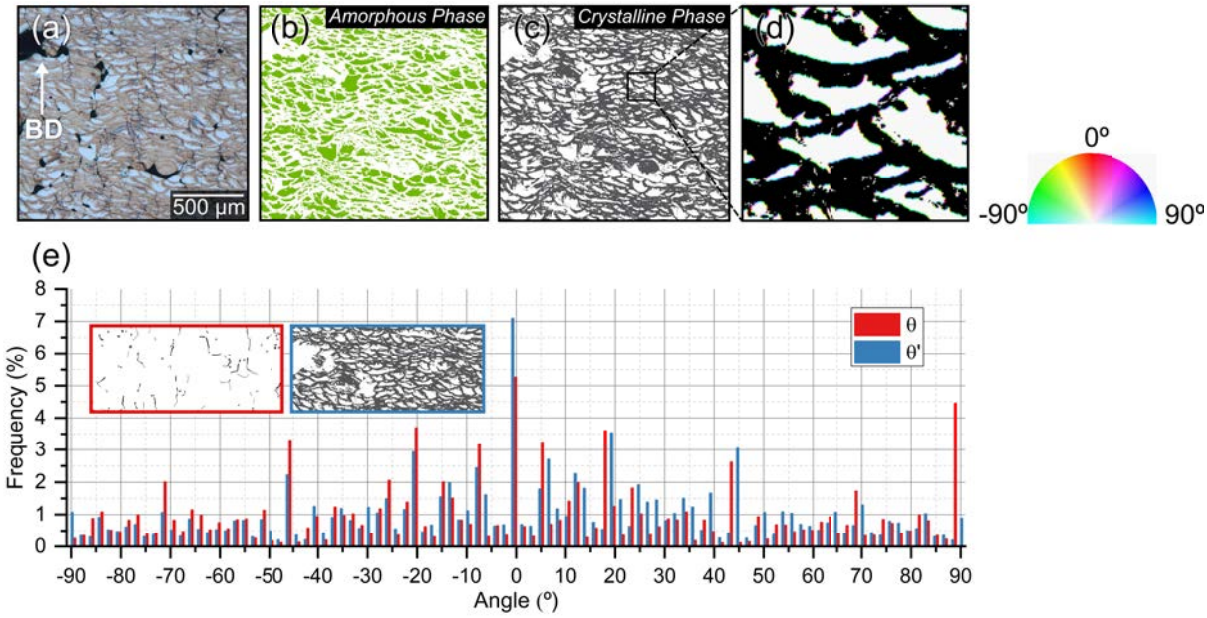

Figure 4.13. Schematic of the workflow followed to analyze the paths of preferential crack propagation by image analysis. (a) Etched optical micrograph illustrating, in brown contrast, crystalline regions and in light contrast, amorphous regions; (b,c) binarized images highlighting amorphous (green, b) and crystalline (gray, c) phases; (d) enlarged view of a region of (c) in which facets along the crystalline/amorphous interfaces have been colored according to the orientation of their normal direction following the color coding included in the inset. (e) Histogram comparing the preferential orientations of cracks (red bars, θ) and of the directions perpendicular to the different facets along the crystalline/amorphous interphases (blue bars, θ') in the LPBF manufactured Kuamet 6B2 KS1 sample.

4.4.2. Scan strategy as a tool to achieve high density levels and high amorphous fraction simultaneously

The present work has shown the effect of some of the main LPBF processing parameters on the fraction of internal defects, on the generated (micro)structure and on the corresponding magnetic properties. For instance, high P, low v, and low h combinations give rise to high relative density and highly crystalline samples, endowed with high M_s and high H_c. On the other hand, parameter sets including low P, high v, and high h lead to samples with lower relative density and with higher amorphous fraction, which thus possess slightly smaller M_s and a significantly lower H_c. Such findings are coherent with the few works published in the literature on LPBF of similar Fe-based BMGs [78, 82, 84, 85, 89]. It therefore becomes clear that when using a simple scanning strategy, such as the one adopted in the current study (meander), there are no combinations of P, v, and h that will allow to manufacture samples with both the density and the M_s and H_c values required for soft magnetic applications.

Several approaches to overcome the barriers to manufacture Kuamet BMG alloys with high

densities and large amorphous fraction by LPBF have been reported recently [78, 85, 89]. Table 4.2 compares the values of density, amorphous fraction, M_s and H_c corresponding to these studies with those of the current work. The most successful approach, involving the use of a two-pass scanning strategy, was reported by Zrodowski et al. [89] in 2019. The first pass, in which the laser followed a chessboard strategy, would melt the powder once. During the second pass, without depositing a new powder layer, the laser was programmed to follow a "point-random strategy", which consisted on melting single points separate from each other in a random fashion, until the full surface had been re-melted. This strategy yielded, simultaneously, an amorphous fraction of 90 % and a maximum relative density of 94 %. The material used in this study was Kuamet 52, which has a slightly different composition ($Fe_{71}Si_{10}B_{11}C_6Cr_2$ [at. %]) from that of the Kuamet 6B2 used for the presented work. The drawbacks of this complex scanning strategy are a considerable increase in build time and the difficulty to replicate it with commercial LPBF systems. In 2020 Nam et al. [85] proposed a double scanning strategy to manufacture Kuamet 6B2 by LPBF where the laser would first melt a powder layer following a meander path and, without depositing a new layer, it would then re-melt the solid material following a second meander path rotated 90º with respect to the previous scan. This yielded an amorphous fraction up to 47 % in samples with a density of 96 %. Although this double-pass approach is simpler than the point-random strategy, the main drawback continues to be the considerable increase in production time. In 2022 Thorsson et al. [78] manufactured by LPBF a record-large Kuamet 6B2 rotor prototype with an amorphous fraction of 70 % and with a density of approximately 98 % using an advanced scanning strategy that was not disclosed. Further efforts are required to devise advanced scanning strategies that allow to overcome the "density/amorphous fraction" paradox without significantly compromising productivity.

4.4.3. Origin of the strong effect of the scanning speed on crystallization

A key finding of the present study is that, for a given hatch distance, v and, more specifically, the laser exposure time, has a more significant effect on crystallization, and thus on H_c, than P Figs. 4.8 and 4.12, at least when these parameters are changed within the ranges investigated. Since the investigated Fe-based MG is targeted for soft magnetic applications, for which achieving very low H_c values is of paramount importance, understanding the origin of the dominant effect of v is key to devise guidelines for LPBF process optimization.

Table 4.2. Comparison of the relative density, amorphous fraction, and magnetic properties achieved in this study with those reported in the literature for similar alloys [78, 85, 89].

Reference	Material [at. %]	Sample Geometry	Density (%)	Amorphous Fraction (%)	M_s (T)	H_c (A/m)
Zrodowski 2019 [89]	$Fe_{71}Si_{10}B_{11}C_6Cr_2$	Discs (⌀5 mm x 1 mm)	94	90	1.30	397
Nam 2019 [85]	$Fe_{73.7}B_{11}Si_{11}Cr_{2.3}C_2$	Prisms (10 x 10 x 5 mm^3)	96	47	1.22	1600
Thorsson 2022 [78]	$Fe_{73}Si_{11}B_{11}C_3Cr_2$	Rotor (⌀60 mm x 46 mm)	98	70	1.29	510
This work KS11	$Fe_{73.7}B_{11}Si_{11}Cr_{2.3}C_2$	Prisms (8 x 8 x 9.5 mm^3)	93	20	1.23*	4697
This work KS9	$Fe_{73.7}B_{11}Si_{11}Cr_{2.3}C_2$	Prisms (8 x 8 x 9.5 mm^3)	74	46	1.19*	2790

On the other hand, our results also show (Fig. 4.6) that crystallization takes place preferentially because of the heating resulting from the deposition of neighboring tracks and of consecutive layers. For fixed hatch and layer thickness values, the overall volume of the HAZ will, in general, increase with the melt pool size [112], as larger melt pools give rise to a higher degree of overlap between neighboring tracks and between consecutive layers, respectively. In the following, the effect of P and v on the melt pool dimensions is analyzed. Fig. 4.14 illustrates the evolution of the average melt pool's width (W) and depth (D) with v (Fig. 4.14a,c) and with P (Fig. 4.14b,d) in samples manufactured within print 1 (h = 80 μm). Several observations can be made from this figure. First, the fact that $D/W < 1$ for all conditions investigated, together with the semi-circular shape of the melt pools (Fig. 4.6), evidences that LPBF processing was carried out within the conduction mode [3, 6, 113–118]. Second, W decreases with increasing v (Fig. 4.14a) but remains invariant with changes in P (Fig. 4.14b). Third, D is basically independent of v (Fig. 4.14c) and of P (Fig. 4.14d). Altogether, these data suggest that the average melt pool's cross-section and, thus, the HAZ, decreases with increasing v, while remaining almost invariant with P.

In Fig. 4.15 the melt pool's widths of samples KS1-KS25 are related to the corresponding processing parameters (P, v, h). The results are grouped by hatch distance (black dashed rect-

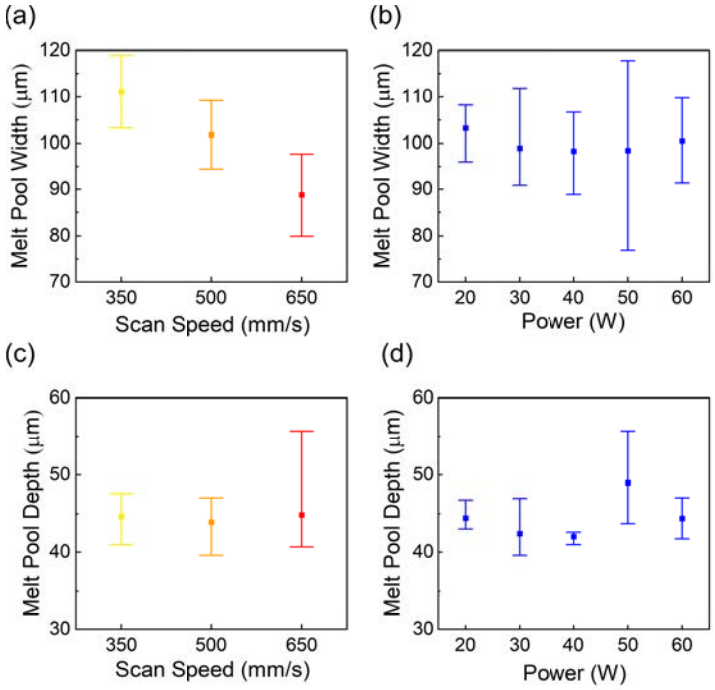

Figure 4.14. (a) Average melt pool width with respect to v; (b) average melt pool width with respect to P; (c) average melt pool depth with respect to v; (d) average melt pool depth with respect to P. The error bars represent the minimum and maximum averages among the samples of each parameter group.

angles). Yellow, orange, and red squares correspond, respectively, to v = 350 mm/s, 500 mm/s, and 650 mm/s. It is apparent that v has a more significant influence than P on the melt pool's width, at least within the parameter range investigated in the present study. Moreover, when h is increased from 50 to 80 μm, the said impact of v on the melt pool's width is further accentuated. Comparison of Fig. 4.15 with Fig. 4.8 and Fig. 4.12 suggests that the origin of the dominant effect of v on amorphous fraction (and therefore on H_c) is, at least partially, related to the stronger influence of v than of P on the melt pool size (and, thus, on the corresponding HAZ). Therefore, optimizing v (by tuning the exposure time) might constitute a valuable tool for the design of LPBF-manufactured Fe-based metallic glasses with reduced H_c and high M_s and thus to improve the soft magnetic behavior.

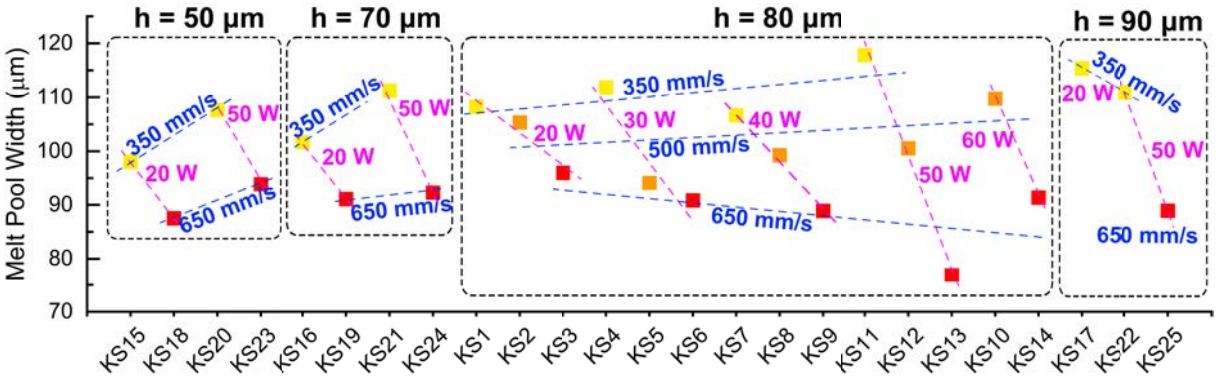

Figure 4.15. Melt pool widths of all samples processed within prints 1 (KS1-15) and 2 (KS1-26) as a function of the LPBF processing parameters. The results are grouped by hatch distance (black dashed rectangles). Yellow, orange, and red squares correspond, respectively, to v = 350 mm/s, 500 mm/s, and 650 mm/s.

Although it is widely agreed that the melt pool size and, in particular, the melt pool width, increase with the VED [12, 119–122], further efforts are needed to understand the effect of isolated processing parameters such as P and v on melt pool geometry for each metallic alloy class [116, 120, 121, 123–125]. In the present work the prevalent influence of v on W described above is not related to the overall VED level as, for example, within print 1, at P = 30 W, increasing v between 350 to 650 mm/s leads to a decrease of VED between 35 and 19 J/mm^3 (Table 4.1, ΔVED = -16 J/mm^3) and to a decrease of the melt pool width of 20 µm while, at v = 500 mm/s, increasing P between 20 to 60 W leads to an increase of VED between 16 and 41 J/mm^3 (Table 4.1, ΔVED = 25 J/mm^3) and to an increment of the melt pool size of only 4 µm. That is, within a similar VED range, comparable changes in VED achieved by changing either P or v led to larger variations of the melt pool geometry when altering v. This research, thus, suggests, that, within the LPBF parameter ranges investigated, changes in v (by altering the exposure time) have a stronger effect in heat conduction than altering P.

4.5. Conclusions

This study aims to establish a relationship between the LPBF processing parameters, the (micro)structure, and the magnetic behavior of a Fe-based Kuamet 6B2 BMG for soft magnetic applications. With that purpose, an extensive range of LPBF process parameter sets (P, v, and h), a simple meander strategy, and a fixed layer thickness of 30 µm, were utilized to manufacture simple geometry specimens. The LPBF processing parameters were related to (micro)structural features such as the density, the area fraction of pores and cracks, the fraction of amorphous and

crystalline phases, and the (micro)structure of the crystalline regions. Finally, soft magnetic properties such as M_s and H_c were measured and related to the LPBF parameters and to the (micro)structure. The following conclusions can be drawn from the present work.

1. Within the entire LPBF processability window the manufactured samples present composite-like structures formed by crystalline and amorphous phases. Crystallization occurs preferentially in the HAZs surrounding melt pools due to the melting of neighboring layers or of consecutive passes. Crystalline regions are formed by α-Fe/Fe_3Si, $Fe_{23}B_6$, and Fe_2B equiaxed grains with random orientations and sizes ranging from a few microns to the nano regime.

2. In the conduction regime investigated here, the parameter sets giving rise to the highest densities (high P, low v) caused the most crystallization and, in turn, settings leading to high porosity (low P, high v) allowed the material to retain the highest amorphous fraction after fabrication. In particular, the highest density (93.1 %) was achieved in a sample that was 20 % amorphous, while the highest amorphous fraction (46 %) was achieved in a sample with a density of 73.7 %.

3. Comparatively, for a fixed hatch distance, the scanning speed had a stronger effect than the laser power in the resulting amorphous fraction. The origin of the potent effect of v lies in its stronger influence on the melt pool size and, in turn, on the corresponding HAZ volume.

4. The saturation magnetization and the coercive field of the LPBF processed samples are both inversely related to the amorphous fraction, albeit the influence of the latter is much stronger in H_c. In comparison with a fully amorphous ribbon of the same composition the saturation magnetization obtained in printed samples is slightly larger due to the presence of crystalline phases, but the lowest coercivity achieved is still three orders of magnitude larger.

5. The preferential paths for crack propagation lie perpendicular to crystalline/amorphous interfaces. Thus, altering the geometry of and spatial distribution of melt pools, and consequently of the associated HAZs, might constitute a useful tool to design crack networks leading to higher resistance to eddy currents and, in turn, to lower energy losses.

5. MULTISCALE MECHANICAL CHARACTERIZATION OF A LPBF-MANUFACTURED FE-SI-B-CR-C (KUAMET 6B2) ALLOY

5.1. Background

The previous chapter established the fundamental relationships between processing parameters, defects, (micro)structure and soft magnetic properties of a commercial Fe-based glass-forming, Kuamet 6B2. It was shown that, regardless of the combination of processing parameters, samples exhibited some degree of internal defects such as LoF voids and highly oriented cracks. While most published works on this alloy focused on the evaluation of the magnetic behavior of the material [78, 85–87, 89], which is of primary interest for industrial applications, the ever-present internal defects are expected to influence the mechanical properties, which are also relevant for electro-mechanical applications. In particular, the effect of persistent highly oriented defects on the micromechanical behavior of LPBF-processed samples, as well as the size effects must be understood. Furthermore, the mechanical properties at the microscale have not been studied on this alloy, where the range of microstructural features reported in Chapter 4 is expected to yield heterogeneous micromechanical properties. A deeper understanding of the interplay between said internal defects, (micro)structure, and mechanical properties is essential for the successful adoption of this material in highly efficient electrical machines.

This chapter aims to contribute to filling this gap in the understanding of the LPBF-processed Kuamet 6B2 alloy by presenting the first investigation on the effect of the defect structure and of the (micro)structure on the multi-scale mechanical performance of specimens of different sizes. With that goal, a combined macro- and micromechanical testing campaign was put in place, and the results are related to the presence of voids, cracks and (micro)structural features in the manufactured samples.

5.2. Methods

5.2.1. LPBF processing parameters

The results from Chapter 4 were taken as reference to produce uniaxial compression specimens for the present study. The combination of parameters previously referred to as KS7 was selected to ensure sufficient mechanical stability for testing. In particular, specimens were processed with P of 40 W, t of 30 μm, h of 80 μm, t_{ON} of 220 μs, and pd of 80 μm, which yielded approximately a v value of 363 mm/s. This combination of parameters was shown to yield a relatively high density (88 % in $8 \times 8 \times 9.5$ mm^3 prisms) and to cause severe devitrification, resulting in an amorphous fraction of only 11 % in the cuboids. A meander scanning strategy with a 67° rotation between successive layers was applied.

Cuboidal specimens with nominal side lengths (S) of 4, 6, and 8 mm were thus manufactured. The actual edge lengths, measured with a caliper after fabrication, averaged 4.17 mm, 6.13 mm, and 8.09 mm, respectively. In total, 30 cuboids were produced, with 10 specimens of each size. Out of these, 2 of each size were reserved for defect and microstructural analysis, while the remaining 8 were used for uniaxial compression tests along two perpendicular loading directions.

5.2.2. Mechanical properties

Room temperature uniaxial compression tests were conducted both parallel and perpendicular to the build direction (BD) in an Instron 3384 electromechanical system furnished with a 150 kN load cell at room temperature. Samples were placed between two plates that moved at a constant crosshead speed equivalent to an initial strain rate of $5 \times 10^{-4} s^{-1}$. A minimum of three tests were performed for each testing condition. The displacement of the load plates was measured using an Instron dynamic extensometer with 12.5 mm gauge length and ±2.5 mm travel. The Young's modulus (E), the maximum stress (σ_{max}) and the uniform strain (e_u) were recorded for each testing condition.

5.3. Results and Discussion

5.3.1. Density and analysis of the defect structure

Fig. 5.1 illustrates the variation of the density, measured by the Archimedes method, with size (S) for all the LPBF manufactured cuboids. Despite the relatively wide scatter in the data, this figure reveals that there is a decrease in density with increasing S. The average density in the printed samples amounted to 6.99 g/cm^3 (4 mm), 6.96 g/cm^3 (6 mm), and 6.89 g/cm^3 (8 mm). These values are naturally lower than the density of a cast Kuamet 6B2 sample (7.14 g/cm^3). Consistently, estimation of the relative area density from optical micrographs by image analysis yielded values of 92.41 %, 90.63 %, and 90.92 % for 4-, 6-, and 8-mm cuboids, respectively. The average density data are summarized in Table 5.1.

Irrespective of their size, all LPBF-manufactured cuboids exhibited the same three types of defects: voids, internal cracks, and surface cracks. Fig. 5.2a shows a representative optical micrograph of a cross-section parallel to BD of an 8-mm cuboid, where the three types of defects are isolated (see insets 1, 2, and 3, respectively). The porosity observed in all samples corresponds to lack-of-fusion (LoF) defects, which is known to arise from insufficient input energy to fully melt the feedstock powder and typically appear as elongated pores oriented perpendicular to the BD [3]. The total fraction of voids was calculated including those with areas larger than 2500 pixels. Such voids, named hereafter “type-1 voids”, are highlighted in black as an example in region (1) of Fig. 5.2a. The area fraction of type-1 voids in cuboids with 4-, 6-, and 8-mm sides amount to 5.01 %, 7.80 %, and 7.48 %, respectively (Table 5.1). The observed reduction of the area fraction of LoF voids as the sample’s cross-section decreases is attributed to the smaller associated rescan times. Indeed, shorter hatch tracks lead to an increase in the basal temperature of the material which leads to higher temperatures during the heating cycles of newly scanned tracks [126–129]. Such heat accumulation within the sample and consequently enhance fusion between powder particles, ultimately yielding denser parts [130]. The average type-1 void length (a_1, measured perpendicularly to BD), width (b_1, measured in parallel to BD) and the aspect ratio (a_1/b_1) are summarized in Table 5.1 and the variation a1 with respect to the sample size is represented in Fig. 5.2b. A minor increase in a_1 is noted when the specimen size increases from 4 mm to 6 and 8 mm. Specifically, a_1 increases from 145 μm to 170 μm and 162 μm, respectively. Moreover, all samples show type-1 voids which are mainly

elongated in the perpendicular direction to BD ($a_1 > b_1$).

Since it is expected that the largest pores are preferential crack initiation sites [22] and that they are likely to have a dominant influence on the mechanical response, a subset of type-1 voids with areas larger than 20000 pixels was isolated. Such voids, hereafter termed as type-2, are highlighted in region (1) of Fig. 5.2a and their main characteristics (area fraction, length (a_2), width (b_2), and aspect ratio (a_2/b_2)) are summarized in Table 5.1. The area corresponding to type-2 voids also increases with increasing specimen size, from 2.29 % in 4 mm cuboids to 4.95 % and 4.45 % in 6- and 8-mm cuboids, respectively. The aspect ratio of type-2 voids is larger than that of type-1 voids. Fig. 5.2b illustrates the variation of a_2 with specimen size. It can be seen that a_2 increases from 279 μm (4 mm) to 351 μm (6 mm), and 344 μm (8 mm), respectively. The aspect ratio of type-2 voids is larger than that of type-1 voids, indicating a more pronounced elongation perpendicularly to the BD.

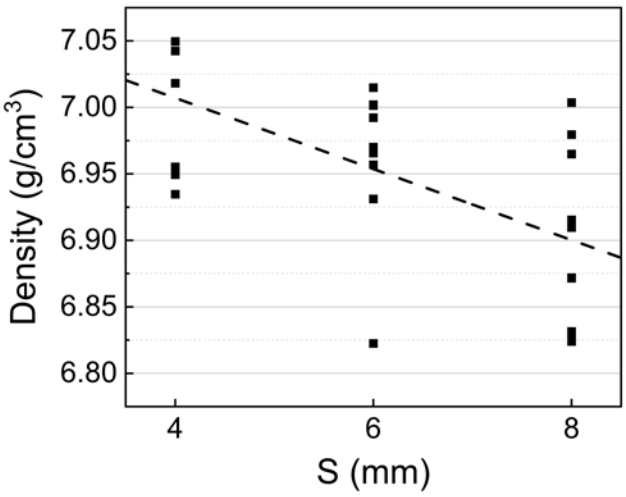

Figure 5.1. Archimedes density with respect to sample size (S).

Internal and surface cracks have been observed in additively manufactured Fe-based metallic glass parts [82, 84, 95]. These defects are formed as a result of the thermal stresses originated from the solidification of consecutive tracks and/or layers [95], which cannot be sustained by brittle materials with high sensitivity to temperature gradients [82, 84]. Table 5.1 summarizes the area fraction and the average length (a_3) of internal cracks. Internal cracks are homogeneously distributed throughout the sample interior and their area fraction is significantly higher in the 4 mm samples than in larger cuboids (2.59 % (4 mm) vs. 1.57 % (6 mm), and 1.60 % (8 mm), respectively. As shown in Fig. 5.2b, internal cracks are longest in the 4

mm sample (45 μm) and virtually equally long in the 6 mm and 8 mm specimens (31 and 29 μm, respectively). These cracks are preferentially tilted at ±0°, ±5°, ±15°, ±20°, ±25°, ±45° ± 50°, ±70°, ±75°, ±85°, and ±90° angles with respect to BD, consistent with the observations presented in Chapter 4.

Finally, surface cracks were observed to propagate perpendicular to BD, extending into the interior of the manufactured samples. The average crack length (a_4) is summarized in Table 5.1 and plotted in Fig. 5.2b as a function of specimen size. The measured values were 318 μm, 321 μm, and 306 μm for the 4-, 6-, and 8-mm cuboids, respectively, indicating a slightly smaller average length in the largest specimens. The area fraction of surface cracks was not quantified due to the irregularity of the sample surfaces, which prevented an accurate image analysis.

Table 5.1. Summary of the density and defect characteristics for the three sample sizes studied.

		4 mm	**6 mm**	**8 mm**
Arquimedes density (g/cm^3)		6.99	6.96	6.89
Relative area density (from OM) (%)		92.41	90.63	90.92
Type-1 voids > 2500 pixels	Number (-)	51	141	267
	Area fraction (%)	4.30	7.07	6.63
	Avg. a_1 (μm)	145	170	162
	Avg. b_1 (μm)	127	138	136
	Avg. a_1/b_1 (-)	1.14	1.23	1.19
	Avg. a_1/S (-)	0.035	0.027	0.020
Type-2 voids > 20000 pixels	Number (-)	11	36	62
	Area fraction (%)	2.29	4.95	4.45
	Avg. a_2 (μm)	279	351	344
	Avg. b_2 (μm)	201	237	250
	Avg. a_2/b_2 (-)	1.38	1.48	1.37
	Avg. a_2/S (-)	0.067	0.057	0.043
Internal cracks	Number (-))	6040	3458	1237
	Area fraction (%)	2.59	1.57	1.60
	Avg. a_3 (μm)	45	29	31
	Avg. a_3/S (-)	0.011	0.005	0.004
Surface cracks	Number (-)	10	21	26
	Area fraction (%)	N/A	N/A	N/A
	Avg. a_4 (μm)	318	321	306
	Avg. a_4/S (-)	0.076	0.052	0.038

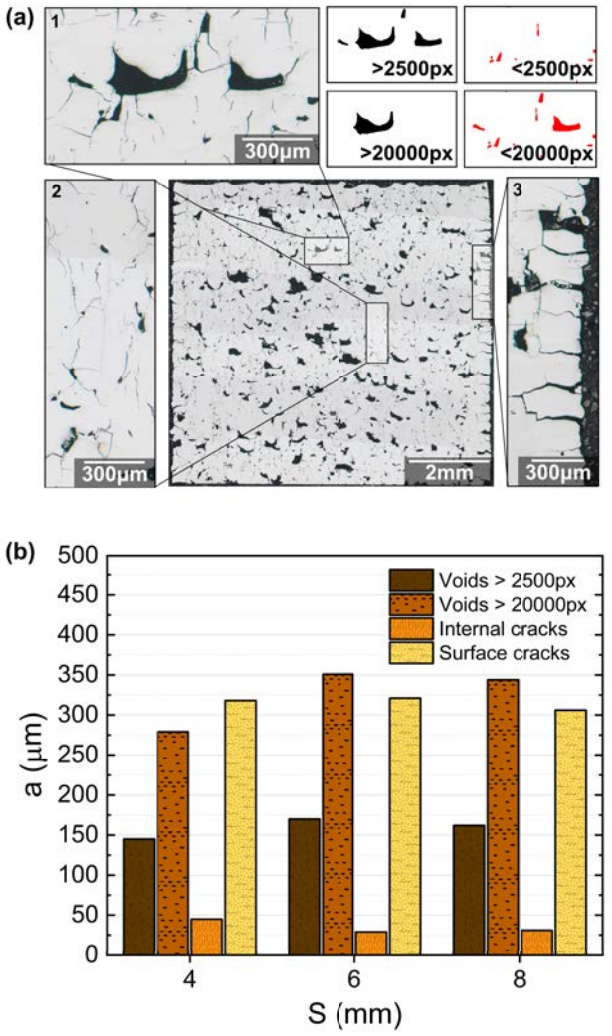

Figure 5.2. (a) Optical micrograph of a cross-section parallel to BD of an 8 mm sample. The insets highlight the different classes of defects: (1) lack of fusion pores, (2) internal cracks, and (3) surface cracks. (b) Variation of the defect length (ai) with respect to the sample size (S).

5.3.2. Macromechanical behavior

Fig. 5.3a-c illustrate the room temperature engineering stress-strain curves corresponding to the LPBF-manufactured 4-, 6-, and 8-mm cuboids. For each specimen size, tests performed with the compression axis parallel to BD (||BD, black lines) and perpendicular to BD (⊥BD, red lines) are compared. Three tests were performed for each condition. Irrespective of the specimen size, failure occurs at strains approximately equal or smaller than 2 %. Fig. 5.3d and Fig. 5.3e illustrate the fracture surface of a representative 6 mm ||BD specimen, which exhibit typical features of brittle failures in MGs, including shear bands (highlighted with yellow arrows) and smooth facets [27, 62].

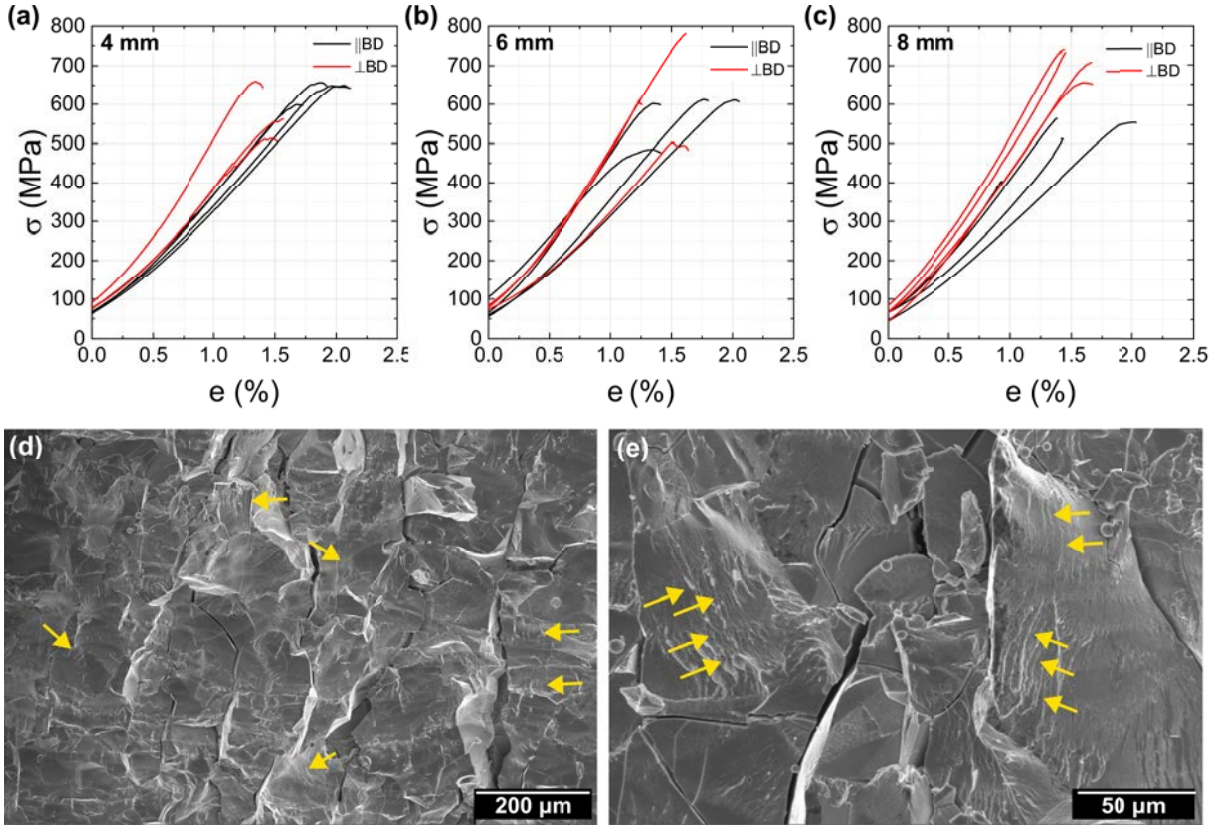

Figure 5.3. (a-c) Uniaxial compression engineering stress-strain curves corresponding to 4-, 6-, and 8-mm cuboids. The black curves correspond to tests performed with the compression axis parallel to BD (||BD) and the red curves correspond to tests conducted with the compression axis perpendicular to BD (⊥BD). (d,e) Representative SEM images of the fractured surface of a 6 mm sample tested along the BD. Yellow arrows are used to mark the appearance of shear bands.

Fig. 5.4 summarizes the variation of E, σ_{max} and e_u with the sample size. Fig. 5.4a shows that there is no perceptible relationship between the sample size and the Young's modulus. However, the average value of Young's Modulus for ||BD samples is smaller than that of BD samples (33 GPa and 44 GPa, respectively). It is well known that the presence of significant fractions of defects have a notable influence in E. For instance, porosity values between 3 % and 7 % have been reported to reduce E by 16 %, following a negative exponential law, when LPBF-processed AMZ4 alloy, a widely studied metallic glass composition, was tested under tension [131]. Furthermore, in numerical studies [132], crack densities of 1.5 % have been reported to decrease the Young's modulus by up to 70 %. In the present study, results of image analysis indicated that samples' porosity due to type-1 voids ranges between 4.3 % and 7.1 % and crack density ranged between 1.6 % and 2.6%. Moreover, type-1 and type-2 voids are elongated perpendicular to the BD, which increases compliance along the BD and is consistent with the lower Young's modulus measured in samples tested parallel to the BD.

Fig. 5.4b and Fig. 5.4c evidence that the maximum stress and the uniform deformation ex-

hibit opposite trends with sample size for the two investigated loading directions. In the ||BD samples, both σ_{max} and e_u decrease as the sample size increases, while in ⊥BD samples, σ_{max} and e_u increase with increasing sample size. In particular, as the specimen size increases from 4 mm to 8 mm, σ_{max} in ||BD samples decreases from 660 to 400 MPa (8 mm), while in ⊥BD samples it increases from 520 to 780 MPa. Conversely, for the same range of specimen sizes, e_u in ||BD samples decreases from 2.0 to 1.4 % and in ⊥BD samples it increases slightly from 1.5 to 1.6 %.

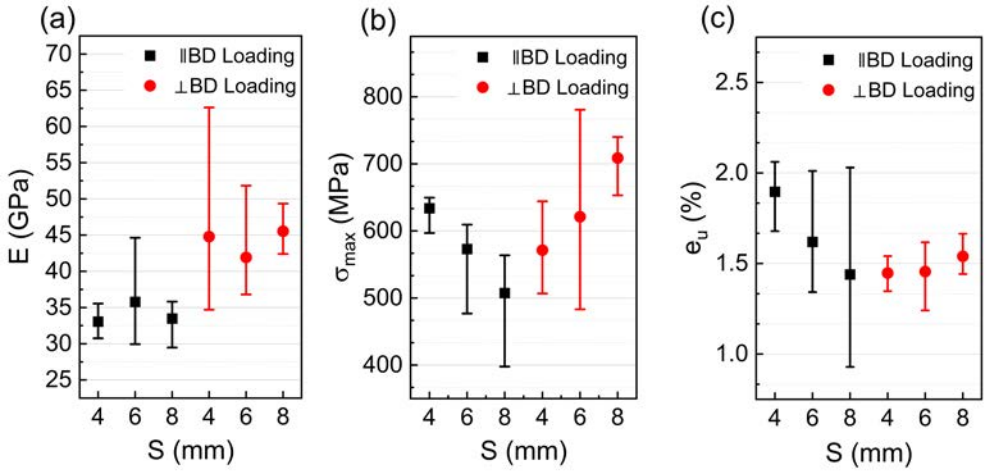

Figure 5.4. Variation of (a) the Young's modulus, (b) the maximum stress, and (c) the uniform deformation with respect to the sample size (S) and to the compression loading mode.

In the following we correlate the variations in the maximum stress reported in Fig. 5.4b with the defect structure described in Section 5.3.1. Internal cracks will not be considered in this analysis because, as shown in Table 5.1 and Fig. 5.2, their area fraction is significantly smaller than that of type-1 (and even type-2) voids and their average length is considerably shorter than that of type-2 voids and surface cracks. Therefore, they are not expected to exert a dominant influence on the mechanical behavior.

Fig. 5.5 schematically illustrates the orientation of type-2 voids (Fig. 5.5a) and surface cracks (Fig. 5.5b) with respect to the loading axis for both ||BD and ⊥BD specimens. Under ||BD loading, the compression axis is perpendicular to the longer dimension of these two types of defects, which therefore tend to close or decrease in width during testing. This leads to denser specimens in which strength scales with density, which itself increases with decreasing sample size (Fig. 5.1 and Table 5.1). In contrast, under ⊥BD loading the compression axis is parallel to the longer dimension of voids and surface cracks, promoting stress localization at pore and crack tips. The stress intensity factor (SIF) at the tip of an elongated pore or crack is proportional to

the corresponding a_1/S ratio [133, 134], which is reported in Table 5.1 for voids and surface cracks. Type-2 voids exhibit a_2/S ratios of 0.067, 0.057, and 0.043 in cuboids with 4-, 6-, and 8-mm sides respectively. In turn, surface cracks exhibit a_4/S ratios of 0.076, 0.052, and 0.038, respectively. In both cases the a_i/S ratios decrease with increasing sample size, leading to a lower SIF, suppression of crack propagation and, consequently, higher σ_{max} and e_u.

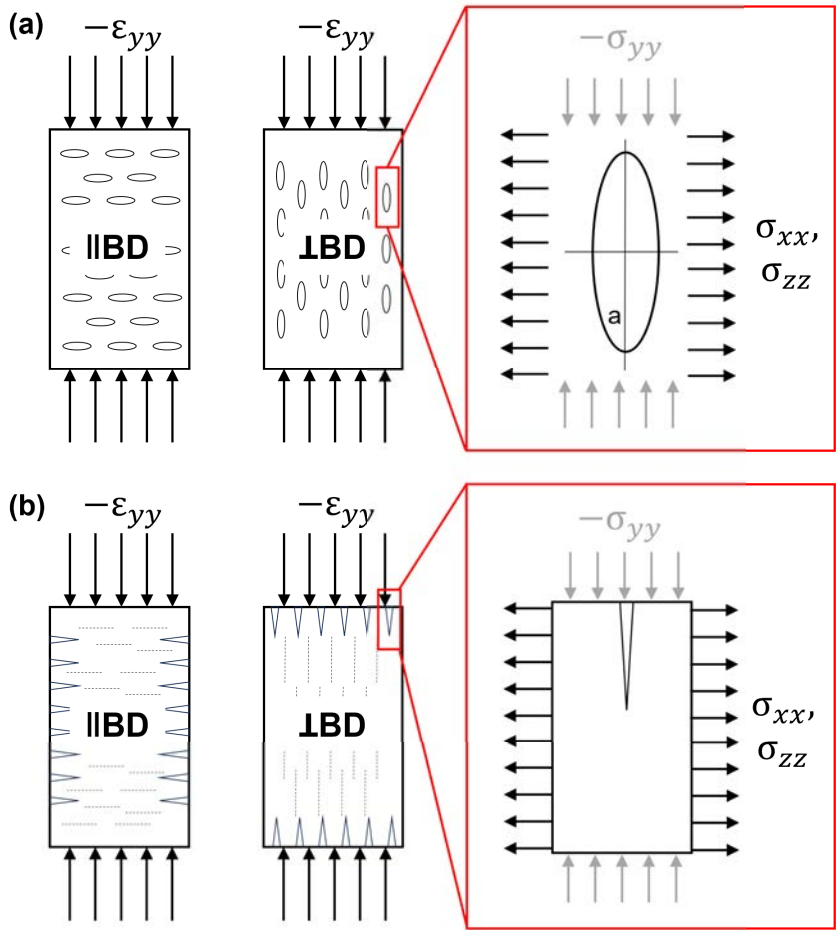

Figure 5.5. Schematic illustrating the stress state and the orientation of (a) voids and (b) surface cracks for tests where the compression axis lies parallel (∥BD) and perpendicular (⊥BD) to BD.

5.3.3. Micromechanical behavior

Fig. 5.6 depicts the local (micro)structure and the corresponding variation of the Young's modulus and of the microhardness in an area free of defects in a representative 8 mm Kuamet 6B2 cuboid. Fig. 5.6a presents an EBSD band contrast map where gray areas denote crystalline regions and black areas correspond to regions containing amorphous phase or crystallites with sizes that are below the resolution of the measurement (approximately 240 nm). Fig. 5.6b illustrates an inverse pole figure (IPF) map in the BD, where the orientations of crystallites are col-

ored according to the color key included in the inset. In agreement with EBSD work presented in Chapter 4 and similar work [90], both maps confirm that crystallites are mostly present in the heat affected zone (HAZ) surrounding the melt pools (MP), have a random crystallographic texture, and grain sizes that decrease gradually with the distance to the MP. Fig. 5.6c and Fig. 5.6d depict the corresponding Young's modulus and nanohardness (H) maps. Amorphous regions exhibit the lowest Young's modulus and the lowest hardness, with E values ranging between approximately 190 and 220 GPa and hardness value between 11 and 12.5 GPa. The crystalline regions are characterized by a higher Young's modulus, ranging between 230 and 290 GPa, and a higher hardness, comprised between 13 and 16 GPa. The variations in E and H in the crystalline regions are likely attributed to differences in the Fe(Si) grain size and to the heterogeneous spatial distributions of Fe_2B and $Fe_{23}B_6$ [135, 136]. While grain size differences and phase spatial arrangement clearly influence micro-mechanical properties. It must be noted that the Young's modulus measured by nanoindentation is as much as 6 times higher than the bulk value measured from the macromechanical compression tests (Fig. 5.4a). Such large deviation is attributed to the presence of defects, which leads to a significantly higher compliance.

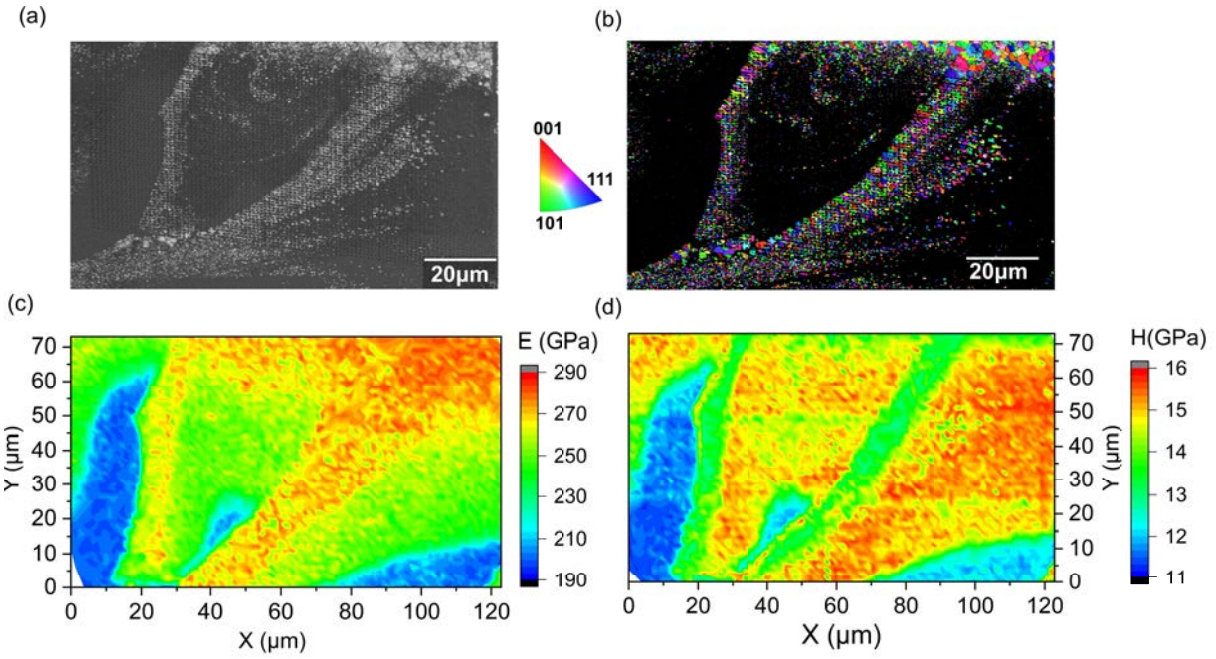

Figure 5.6. Local (micro)structure and nanoindentation data corresponding to a representative 8 mm Kuamet 6B2 cuboid processed by LPBF. (a) EBSD band contrast map. Crystalline and amorphous regions are colored in gray and black, respectively; (b) EBSD IPF map in the BD; (c) Young's modulus map; (d) hardness map.

5.4. Conclusions

In summary, a significant fraction of highly oriented defects was found on Kuamet 6B2 specimens of different sizes processed by laser powder bed fusion. These results are consistent with those of Chapter 4. Regardless of the processing parameters or scanning strategy, internal defects and local devitrification have never been fully avoided on Kuamet 6B2. More importantly, the consequences of such defects and crystalline features on the mechanical response of the material had not been thoroughly studied in this composition. The present work provides an understanding of the effect of typically observed voids, cracks and crystallites resulting from devitrification of the previously deposited amorphous layers on the mechanical properties at different length scales. However, it is expected that the complexity of said relationships will increase for intricate print geometries. Hence, future work in the field should aim to eliminate the aforementioned undesired features by means of alloy design or through advanced LPBF processing control. Until then, the following findings must be considered during the design and production of Kuamet 6B2 components using LPBF:

1. Irrespective of the sample size, three main kinds of highly oriented defects were identified in the Kuamet 6B2 LPBF manufactured samples: large LoF pores elongated perpendicularly to the BD, oblique internal cracks preferentially propagated at specific angles relative to the BD, and large surface cracks perpendicular to the BD. The presence of these defects has a strong influence on the mechanical behavior.

2. The Young's modulus of the LPBF manufactured samples is as much as six times smaller than that of the bulk alloy due to the presence of voids and cracks. Moreover, E is smaller when testing parallel to BD than when testing along a direction perpendicular to BD, as in the former case voids and surface cracks tend to close during testing, thus enhancing compliance.

3. When testing ||BD, the maximum stress and uniform deformation exhibit an inverse correlation with sample size. This trend is attributed to the higher density achieved in smaller specimens.

4. When testing ⊥BD, the maximum stress and uniform deformation exhibit a positive correlation with sample size. This behavior is attributed to the decrease in the ai/S ratios,

and consequently in the stress intensity factor, with increasing size, which enhances the suppression of crack propagation.

6. LPBF OF FE-SI-B-CR-C (KUAMET 6B2) USING TIME DELAYS

6.1. Background

Chapters 4 and 5 have established the fundamental relationships between LPBF processing parameters, internal defects, (micro)structure and mechanical and soft magnetic properties of a commercial Fe-based glass-forming alloy. A simple scanning strategy was used to facilitate the reproducibility of results in the scientific community. However, due to the low GFA of this system, the processing parameters that yield dense parts also result in severe devitrification, producing glassy-crystalline composites [76–79, 82, 84–86, 90, 93]. Chapter 4 evidenced that the degree of crystallization generated by the combinations of parameters and scanning strategy used severely hindered the magnetic properties of the alloy. Hence, a breakthrough in LPBF processing of Fe-based BMGs involving advanced scanning strategies would be required to manufacture reliably complex geometry components with dense and fully amorphous structures that would enable a new generation of highly efficient motors with a drastic reduction of energy losses.

Sohrabi et al. [128] recently reported that the density and the amorphous fraction of an LPBF-manufactured Zr-based BMG could be simultaneously increased using conventional parallel single scanning strategies by the introduction of time delays (i.e., pre-defined time periods during which the laser is switched off) after each scan track. This approach reportedly mitigates crystallization at the turning points of the laser, where the dwell time is accumulated by the solidified material at high temperature peaks [137]. Studies on direct energy deposition (DED) of MGs have also shown that the implementation of time delays between printing tracks is a promising approach to reduce the temperature throughout the sample [138–140]. Finally, in LPBF of crystalline metals, time delays between layers [141] and at the turning points of printed tracks [142] have been used to homogenize the thermal profiles throughout the sample. To date, the introduction of time delays in LPBF manufacturing of Fe-based metallic glasses has not been explored.

The aim of this work is to investigate whether the introduction of time delays after each scan track would enable LPBF manufacturing of dense and amorphous Fe-based BMGs using a me-

ander scanning strategy. To that end, LPBF is carried out using pulsed wave emission and a wide range of complementary characterization techniques is utilized to relate the defect structure, the fraction of amorphous phase, and magnetic coercive field (H_c) to the processing parameters on a commercial Kuamet 6B2 Fe-based soft magnetic MG alloy. Additionally, multiphysics finite element (FE) modeling is utilized to simulate the local temperature evolution and crystallization for different combinations of parameters. This combined experimental/numerical approach will provide guidelines for the manufacturing of Fe-based BMGs with high density and high amorphous fractions, thus contributing to enhance their potential as enablers of energy efficient electric mobility solutions.

6.2. Methods

6.2.1. LPBF processing parameters

A total of 28 prisms with dimensions 8×8×5.4 mm^3 were printed with different combinations of parameters, which are summarized in Table 6.1. The layer thickness was maintained at 30 μm, h and pd were both set at 80 μm, which is the approximate size of the laser's spot diameter. LPBF processing was carried out using two values of laser power (P = 120 and 160 W) and two values of laser exposure time (t_{ON} = 80 and 120 μs). The corresponding scan speed values (v = 888 and 615 mm/s, respectively), are also reported in Table 6.1. For each P and v combination, one sample was printed using a conventional meander strategy with 67º rotation between layers and with the minimum default delay time (t_{OFF}) at the end of each scan track (1 ms) and six additional prisms were manufactured with t_{OFF} values of 50, 100, 150, 200, 250, 300 ms. The associated increases in build time for one single sample when introducing these delays are, respectively, 56 %, 116 %, 175 %, 234 %, 294 %, 353 %. A schematic representation of this modified meander scanning strategy is displayed on Fig. 6.1, where areas with different degrees of heat accumulation are qualitatively depicted using a color code. As shown in Fig. 6.1, the introduction of time delays is aimed at reducing heat accumulation in the printed sample. The 28 LPBF-manufactured samples have been divided into 4 groups (A to D), each with common P and v values, and with different t_{OFF} times (A (160 W, 615 mm/s); B (160 W, 888 mm/s); C (120 W, 615 mm/s); D (120 W, 888 mm/s)).

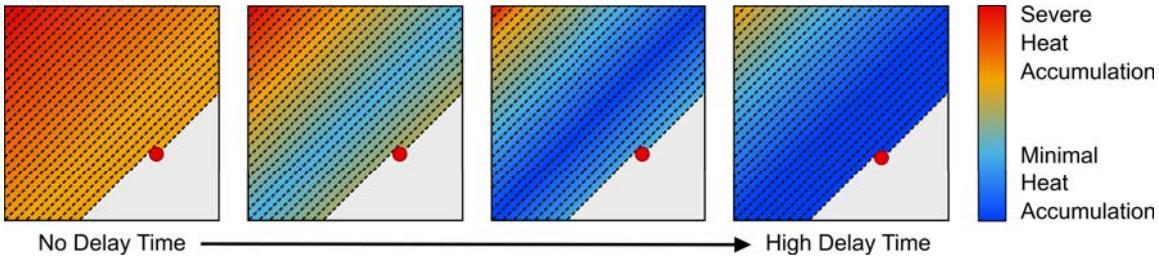

Figure 6.1. Schematic representing the influence of time delays on heat accumulation.

Table 6.1. LPBF processing parameters and normalized volumetric energy density.

Group	Sample ID	P (W)	t_{ON} (µs)	t_{OFF} (ms)	v (mm/s)	E^*
Group A	S1	160	120	1	615	7.08
	S2	160	120	50	615	5.61
	S3	160	120	100	615	5.59
	S4	160	120	150	615	5.59
	S5	160	120	200	615	5.58
	S6	160	120	250	615	5.58
	S7	160	120	300	615	5.58
Group B	S8	160	80	1	888	4.45
	S9	160	80	50	888	3.87
	S10	160	80	100	888	3.86
	S11	160	80	150	888	3.86
	S12	160	80	200	888	3.86
	S13	160	80	250	888	3.86
	S14	160	80	300	888	3.85
Group C	S15	120	120	1	615	4.97
	S16	120	120	50	615	4.20
	S17	120	120	100	615	4.19
	S18	120	120	150	615	4.19
	S19	120	120	200	615	4.19
	S20	120	120	250	615	4.18
	S21	120	120	300	615	4.18
Group D	S22	120	80	1	888	3.21
	S23	120	80	50	888	2.90
	S24	120	80	100	888	2.89
	S25	120	80	150	888	2.89
	S26	120	80	200	888	2.89
	S27	120	80	250	888	2.89
	S28	120	80	300	888	2.89

6.2.2. Simulated LPBF processing conditions and validation

To elucidate the influence of time delays on crystallization, the thermo-metallurgical FEM-based model was utilized to simulate laser melting of a single track processed using P = 160 W and v = 615 mm/s (group A) and of double tracks manufactured with the same P and v, with a

hatch distance of 80 μm, and with time delays (t_{OFF}) of 1, 50, and 300 ms (as in samples S1, S2, and S7). The laser spot size was taken as 80 μm. The model validation campaign included laser melting of single and double tracks with the processing parameters utilized for the simulations and using the Renishaw RenAM500Q Flex system on top of a fully amorphous Kuamet 6B2 plate. The latter was produced by copper mold suction casting with a thickness of approximately 120 μm, which is close to the critical casting thickness for this alloy. The absence of crystalline phases in the substrate prior to laser melting was verified by synchrotron X-ray diffraction at the Deutsches Elektronen-Synchrotron (DESY, Germany). The corresponding XRD pattern exhibited two broad halos around $2\theta = 45°$ and 80°. Before laser melting the amorphous plate was fixed to a 316L steel substrate within the RBV using double-sided copper tape and the stage position was adjusted to place the top surface of the amorphous plate at the focal plane of the laser. cross-sections of the single track and double track melt-pools perpendicular to the scan direction (SD) were prepared for EBSD examination. With that purpose, the substrate plate was held by pins and mounted in conductive resin with the lasered surface perpendicular to the bottom plane, such that the cross-section of the melt pools generated by the melted tracks would be visible after grinding and polishing using the procedures described for EBSD sample preparation in Chapter 3.

6.3. Results

6.3.1. Influence of time delays on processability

All samples in groups A to D exhibited good dimensional stability, with the exception of sample S1 (group A), with the highest E^* (7.08), where severe warping and delamination effects were observed. However, as shown in Fig. 6.2, the introduction of time delays led to improved processability and excellent dimensional stability in group A samples. Fig. 6.2 illustrates the outer appearance of samples S1 (t_{OFF} = 1 ms, which is the minimum default time delay, Fig. 6.2a) and S7 (t_{OFF} = 300 ms, Fig. 6.2b). It can be clearly seen that, while sample S1 experienced severe warping effects, sample S7 retained its original shape. To elucidate the origin of the improved processability with the introduction of time delays, the infrared melt-pool emission during LPBF processing of samples S1 and S7 was measured in-operando using a spectrometer installed at the RenAM500Q system. Measurements were performed at two representative layers (46 and 66) where the direction of the scan tracks is oriented along the

square cross-section's diagonal. The results are shown in Fig. 6.2. In the absence of time delays (sample S1, Fig. 6.2a), significant heat accumulation is observed at the corners, where the scan path is very short. However, switching off the laser after each track for 300 ms (sample S7, Fig. 6.2b) enables sample cooling before the next track is melted, limiting heat accumulation, and hence homogenizing the temperature across the printed layer.

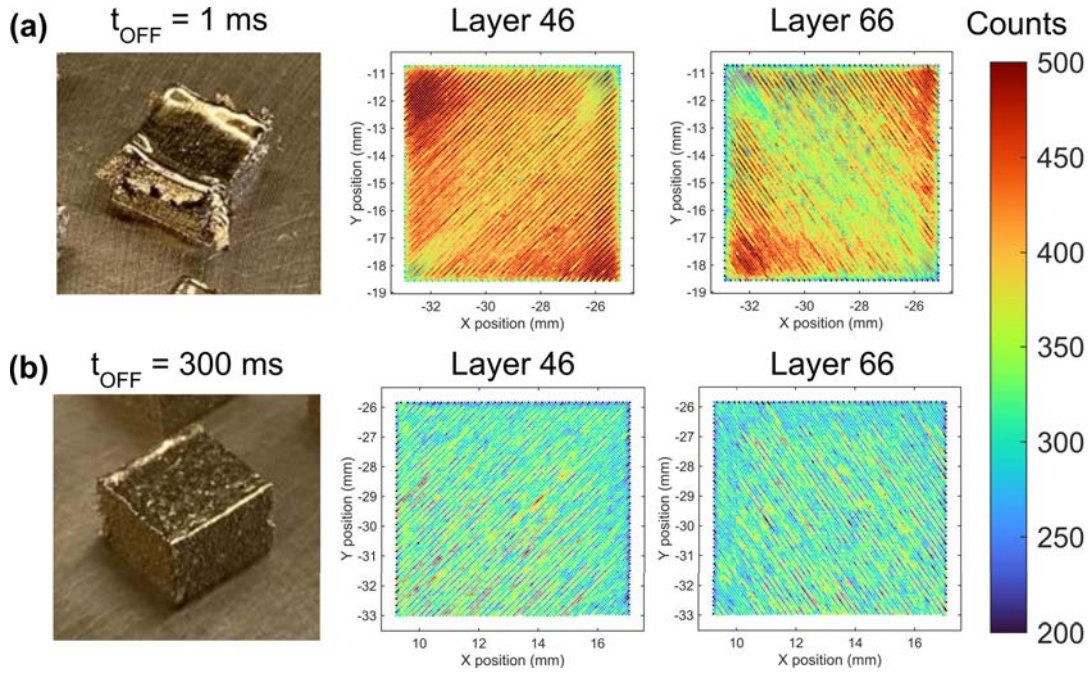

Figure 6.2. Normalized infrared melt pool emission measured in-operando in the RenAM500Q LPBF system during processing of group A samples (a) S1 (P = 160 W, v = 615 mm/s, t_{OFF} = 1 ms) and (b) S7 (P = 160 W, v = 615 mm/s, t_{OFF} = 300 ms) at two representative layers (46 and 66).

6.3.2. Influence of time delays on density and melt-pool geometry

Fig. 6.3 illustrates the influence of the time delay on the density for samples belonging to groups A, B, C, and D. All samples have a relative density above 90 %. Despite the evident scatter within each group, it can be concluded from Fig. 6.3 that group B and C samples, with intermediate E^* values (between 3.85 and 4.97), have on average the highest density, while group A and D samples, with E^* values above 5.58 and below 3.21, respectively, possess a higher fraction of porosity. In samples belonging to groups A, B, and C, the increase in t_{OFF} from 1 ms to 300 ms has a small and/or positive effect on the density. However, most notably, in samples belonging to group D, which have the lowest E^*, an increase in the time delay leads clearly to a notable decrease in density. Fig. 6.4 depicts several optical micrographs illustrating the defect structure in cross-sections parallel to the build direction (BD) of two samples from

each group (A to D) with, respectively, 1 and 300 ms delay. In agreement with Fig. 6.3, it can be seen that increasing the time delay in groups B and C samples (Fig. 6.4c,d and Fig. 6.4e,f, respectively) leads to a moderate increase in density. However, in group A samples (Fig. 6.4a,b) increasing the time delay does not eliminate excessive melting porosity, and in group D samples (Fig. 6.4g,h) time delays introduce a large fraction of lack of fusion defects. Cracks are present in all the manufactured samples, in agreement with Section 4.4.1, and the crack area fraction (around 2 %) appears to be fairly independent of the processing conditions.

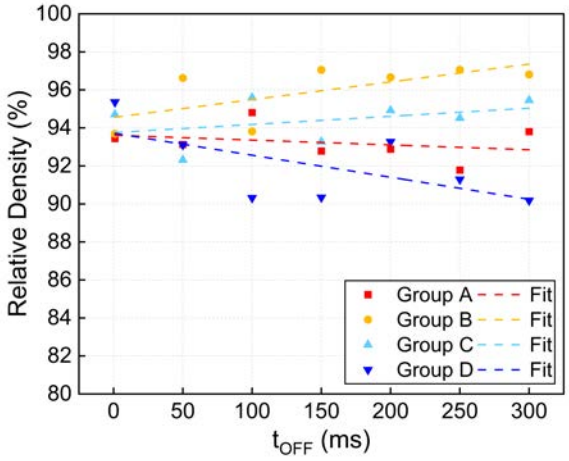

Figure 6.3. Influence of the time delay on the density of the LPBF manufactured prisms. The dotted lines are first-degree exponential decay fits for groups A to D.

Fig. 6.5 illustrates the influence of time delays on the geometry of the melt-pools belonging to all sample groups (A to D). In particular, the effect of the time delay on the melt-pool width (Fig. 6.5a), depth (Fig. 6.5b), and depth to width ratio (Fig. 6.5c), measured at the top layer, is shown. Fig. 6.5a and Fig. 6.5b reveal that both W and D, but especially W, decrease for all sample groups when a time delay of 50 ms is introduced, and then both W and D remain fairly stable for higher time delays. As shown in Fig. 6.5c, the D/W ratio increases slightly with the time delay for groups A and B and it remains stable for groups C and D. For all samples, the D/W ratio ranges between 0.35 and 0.6, suggesting a transition melting mode, where both conduction and keyhole melting are present [143]. Indeed, a close look at the geometry of melt pools at the top layer of samples manufactured with a time delay of 50 ms in groups A (Fig. 6.5d), B (Fig. 6.5e), C (Fig. 6.5f), and D (Fig. 6.5g) reveals the presence of melt-pools with tear-drop shape, characteristic of keyhole mode melting, intermingled with others that resemble a half-moon, which are more typical of conduction melting.

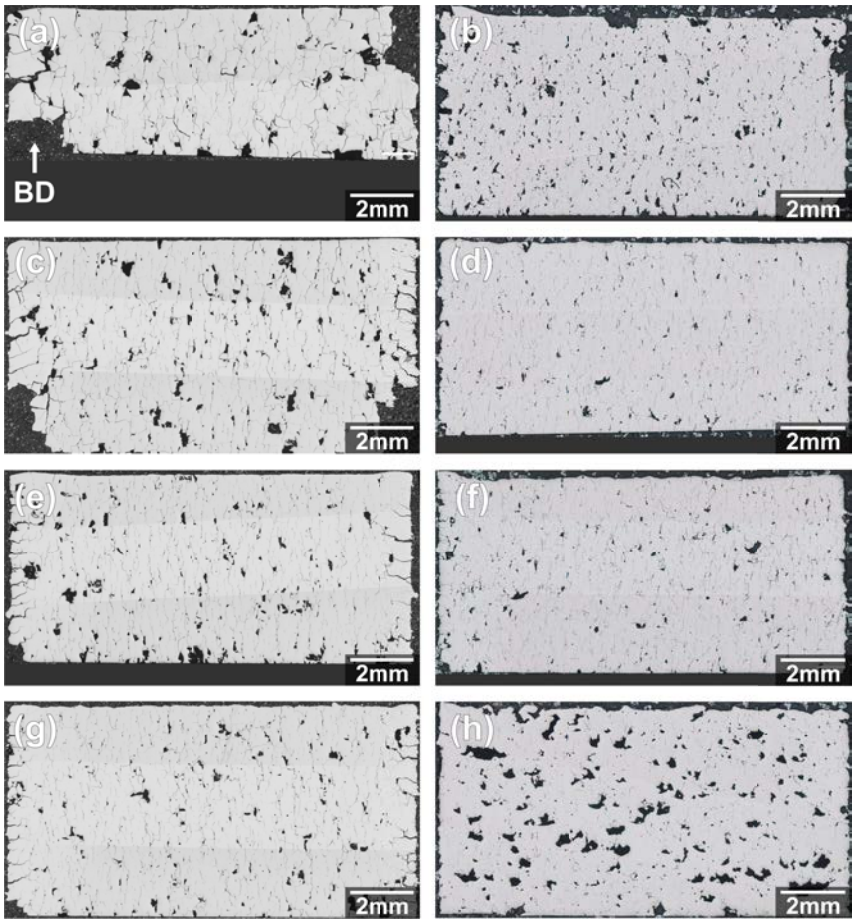

Figure 6.4. Optical micrographs illustrating the defect structure in the following samples: (a) group A S1 (1 ms), (b) group A S7 (300 ms), (c) group B S8 (1 ms), (d) group B S14 (300 ms), (e) group C S15 (1 ms), (f) group C S21 (300 ms), (g) group D S22 (1 ms), (h) group D S28 (300 ms). The imaged cross-sections are parallel to BD.

6.3.3. Influence of time delays on the amorphous fraction

Fig. 6.6 illustrates the influence of time delays in the volume fraction of the amorphous phase (AM %) measured by DSC in all manufactured samples. The highest amorphous fractions, ranging between 60 and 70 %, are obtained in groups C and D, while group A specimens exhibit the lowest AM % due to the excessive energy input. In general, the introduction of time delays leads to an increase in AM % in the LPBF manufactured prisms. The largest variation of AM % is observed for a time delay of 50 ms, and then the increase in AM % is smoother for larger delay times. In particular, the increase in AM % achieved when introducing a time delay of 50 ms in groups A to D amounts to +15 %, +25 %, +41 %, and +33 %, respectively. Also, the increase in AM % achieved when introducing a time delay of 300 ms in groups A to D amounts to +33 %, +40 %, +50 %, and +48 %, respectively.

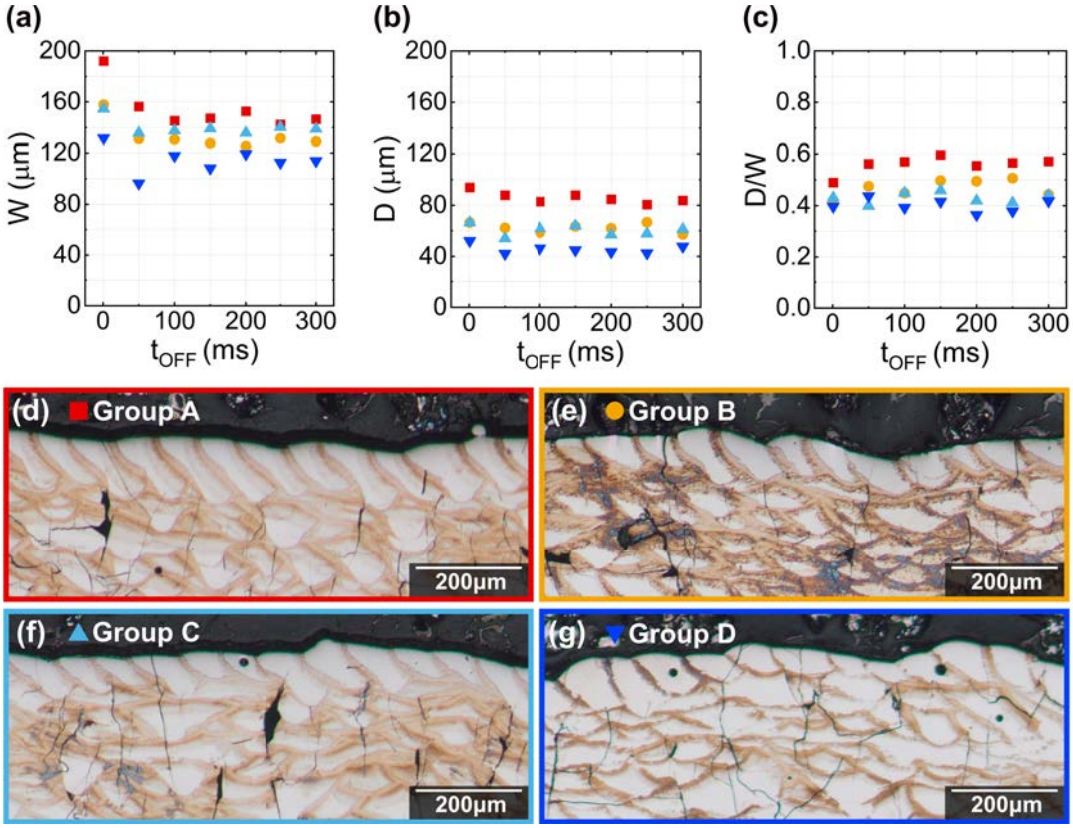

Figure 6.5. Influence of the time delay on (a) the average melt pool width, (b) the average melt pool depth, and (c) the depth to width ratio for samples belonging to groups A to D; (d-g) optical micrographs of etched LPBF samples showing the morphology of melt pools at the top layer for samples manufactured with a time delay of 50 ms in groups (d) A (S2), (e) B (S9), (f) C (S16) and (g) D (S23).

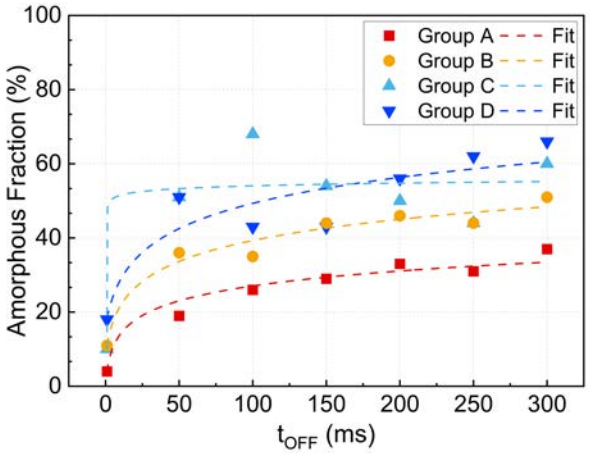

Figure 6.6. Influence of time delay on the fraction of the amorphous phase measured by DSC. The dotted lines are logarithmic fits for groups A to D.

In order to understand the effect of time delays in AM %, the thermo-metallurgical FEM-based model described in Section 3.3.1 is utilized to simulate laser melting of a single track processed using P = 160 W, v = 615 mm/s (i.e., with laser parameters equivalent to those of group A specimens) and of double tracks manufactured with the same P and v, with a hatch

distance of 80 μm, and with t_{OFF} of 1, 50, and 300 ms (as in group A samples S1, S2, and S7). The map of Fig. 6.7a illustrates as an example the temperature distribution during one of the double track simulations. The node from where the temperature readings were captured is located 0.5 mm away from the edge of the simulated volume (Fig. 6.7a) at a location around the center of the melt pool of the first track, and within the heat affected zone (HAZ) of the second track, as indicated by the star symbol in Fig. 6.7b and Fig. 6.7c, respectively. Fig. 6.7d illustrates the temperature profiles corresponding to the simulated single and double tracks. While the first temperature peaks of all three conditions are identical, the maximum temperature of the second peak decreases from 1166 ºC when t_{OFF} = 1 ms to 976 ºC when t_{OFF} = 50 ms, and to 943 ºC when t_{OFF} = 300 ms. Most importantly, the temperature at the selected location when the second track is printed (T_0) decreases from 242 ºC when t_{OFF} = 1 ms to 64 ºC when t_{OFF} = 50 ms, and to 41 ºC when t_{OFF} = 300 ms.

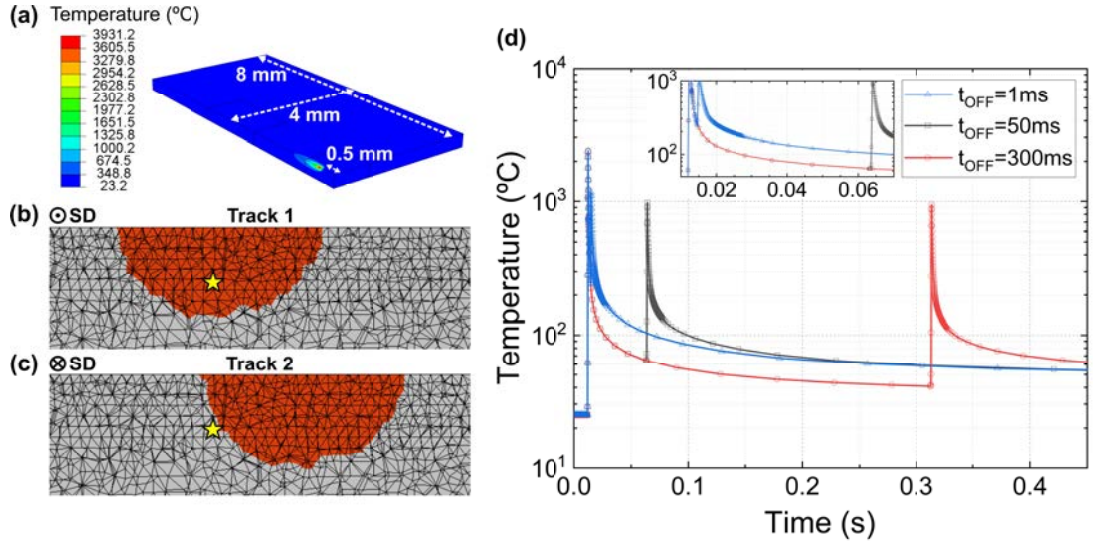

Figure 6.7. (a) A representative image of the FEM-simulated temperature distribution during a double track simulation. (b,c) cross-sections of simulated melt pools perpendicular to the scan direction (SD) during the (b) first and (c) second tracks. The red semicircles indicate the liquid material during scanning and the yellow star marks the location of the node where temperature profiles were evaluated. (d) Simulated temperature evolution during double track experiments using group A conditions with t_{OFF} = 1, 50, and 300 ms. The temperature profiles correspond to a location 0.5 mm away from the edge of the simulated volume.

Single and double tracks were laser melted over an amorphous Kuamet 6B2 substrate with the same manufacturing conditions used in the simulations. Fig. 6.8 compares EBSD band contrast maps of cross-sections perpendicular to the scan direction of the single track (Fig. 6.8a) and of the double tracks (Fig. 6.8c,e,g) with the corresponding FEM-simulated maps illustrating τ, the computed weighted time that the material remains at a temperature between T_x and T_S (Fig. 6.8b,d,f,h). In the EBSD band contrast maps of Fig. 6.8a,c,e,g the gray areas corre-

spond to crystalline regions while the black areas represent regions where the amorphous phase dominates. Comparison of experiments and simulations prove that there is a direct proportionality between the proposed residencetime, τ and the crystalline volume fraction. Fig. 6.8a and Fig. 6.8b suggest, furthermore, that devitrification during laser melting of single tracks is comparatively limited, even when high E^* conditions (group A) are used. However, as shown in Fig. 6.8c and Fig. 6.8d, when a second track is melted adjacently with the minimum default delay time (1 ms) devitrification takes place within a significantly large region within the HAZ. The devitrified region has been pointed with arrows in Fig. 6.10c. Increasing the time delay to 50 (Fig. 6.8e,f) and 300 ms (Fig. 6.8g,h) reduces progressively the size of the devitrified region in the overlap of the two tracks.

In summary, the increase in AM % with the introduction of time delays (Fig. 6.6) is driven by the reduction of T_0 in the amorphous regions solidified during the first pass (Fig. 6.7d), an effect that becomes more pronounced as the delay time increases. Consequently, during the second laser pass, the amorphous regions with lower T_0 within the HAZ spend less time at temperatures between T_X and T_S, leading to a lower degree of devitrification (Fig. 6.8e,f,g,h).

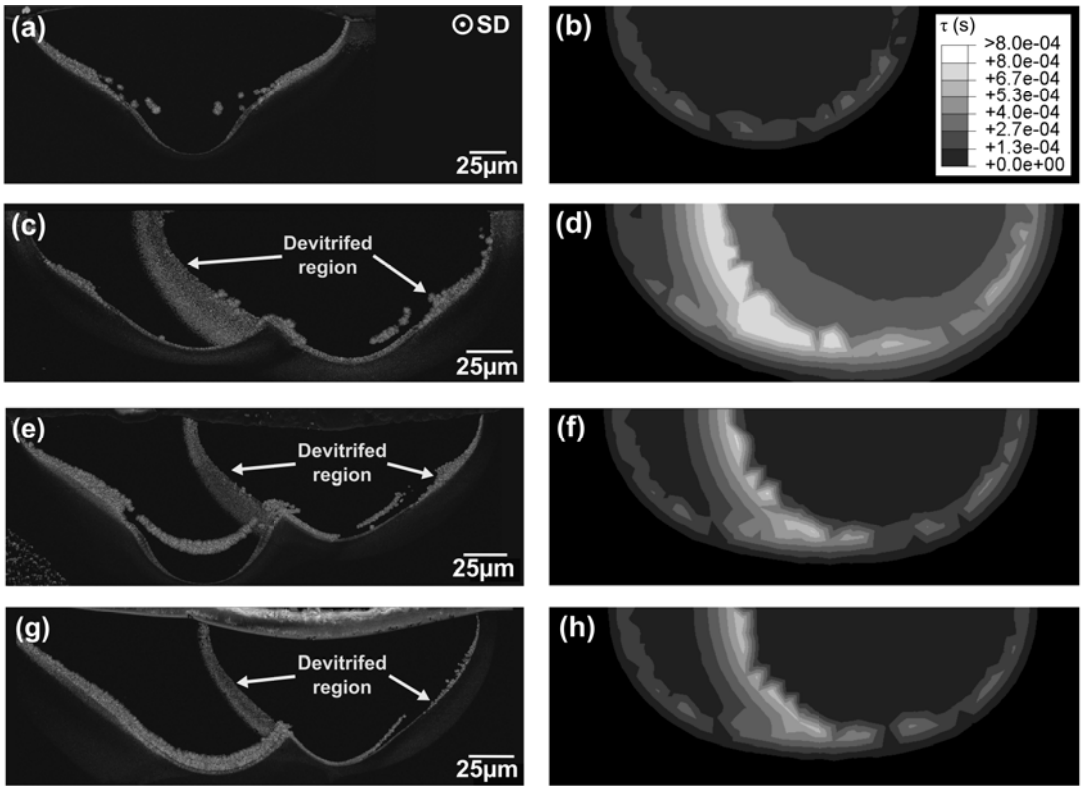

Figure 6.8. (a,c,e,g) EBSD band contrast maps illustrating cross-sections perpendicular to the scan direction of group A (a) single track and (c,e,g) double tracks with (c) t_{OFF} = 1 ms, (e) t_{OFF} = 50 ms, and (g) t_{OFF} = 300 ms; (b,d,f,h) FEM-simulated τ maps corresponding to (b) the single track, and (d,f,h) the double tracks with (d) t_{OFF} = 1 ms, (f) t_{OFF} = 50 ms (h) t_{OFF} = 300 ms.

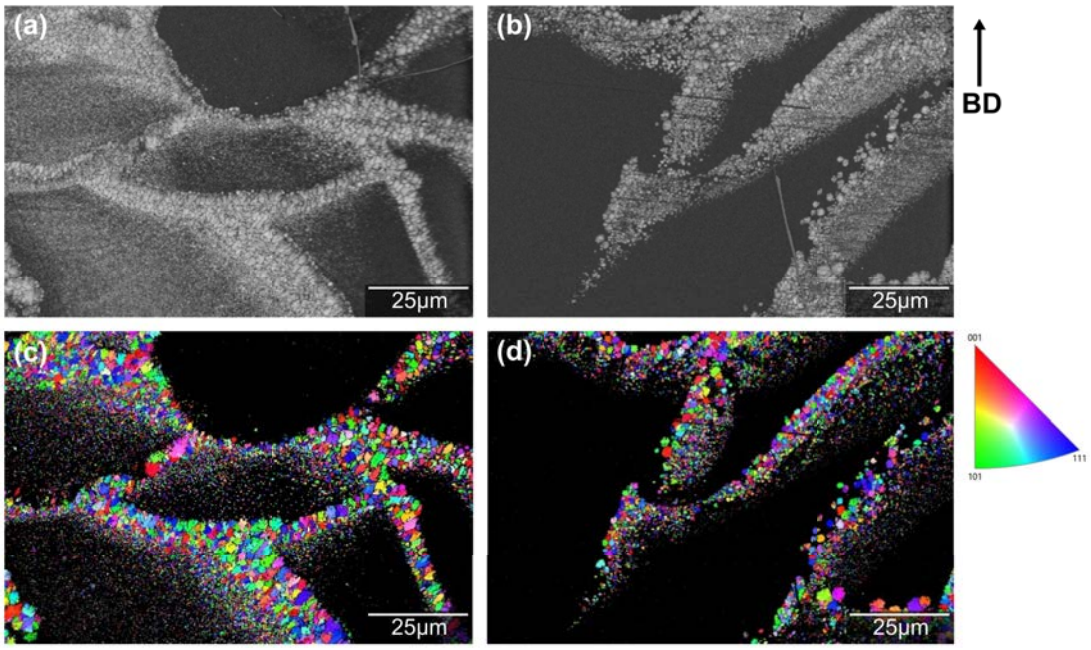

Figure 6.9. EBSD maps of two LPBF processed Kuamet 6B2 specimens processed with a time delay of 50 ms and two extreme E^* values: (a and c) sample S2 (group A, E^* = 5.61, AM % = 19 %) and (b and d) sample S23 (group D, E^* = 2.90, AM % = 55 %). (a, b) Band contrast maps showing in gray the crystalline regions and in black the amorphous regions, where the presence of nano-crystals smaller than the EBSD detection limit cannot be ruled out; (c, d) inverse pole figure maps illustrating the orientation of the build direction.

Fig. 6.9 illustrates several EBSD maps corresponding to the LPBF-manufactured Kuamet 6B2 samples S2 (group A, E^* = 5.61, AM % = 19 %) (Fig. 6.9a,c) and S23 (group D, E^* = 2.90, AM % = 55 %) (Fig. 6.9b,d). In the band contrast maps of Fig. 6.9a,b the crystalline regions are depicted in gray and the amorphous regions are colored in black. The step size used to measure these maps was 120 nm and thus the presence of smaller nanocrystals within the amorphous regions cannot be ruled out. Most importantly, Fig. 6.9a and Fig. 6.9b evidence that, in both specimens, crystallization takes place along the melt pool boundaries and that higher E^* values result in wider crystalline regions, in agreement with Fig. 6.6. The inverse pole figure maps of Fig. 6.9c and Fig. 6.9d, which illustrate the orientation of the build direction (BD), reveal that, irrespective of E^*, crystallites do not have any preferred orientation and are endowed with a relatively equiaxed shape. The grain size is, in both cases, below 4 μm, with the largest grains located close to the melt-pool boundary and a gradient of decreasing sizes with increasing distance from the melt-pool. The dominant phase is Fe_3Si, in agreement with Section 4.3.2.

6.3.4. Influence of time delays on the coercivity

Fig. 6.10 illustrates the evolution of the coercive field (H_c) with the time delay for LPBF-manufactured Kuamet 6B2 specimens belonging to groups A to D. In general, the introduction of time delays leads to a decrease in H_c in the LPBF manufactured prisms. The largest variation of H_c is observed for a time delay of 50 ms, and for larger time delays the coercivity decreases more smoothly, tending towards a stable value. In particular, the reduction in H_c achieved when introducing a time delay of 50 ms in groups A to D amounts to -900 A/m (-16.9 %), -2260 A/m (-46.1 %), -1730 A/m (-36.7 %), and -2170 A/m (-56.7 %), respectively. The total reduction in H_c achieved when introducing a time delay of 300 ms in groups A to D amounts to -2580 A/m (-48.6 %), -3130 A/m (-63.9 %), -2610 A/m (-55.4 %), and -2800 A/m (-73.1 %), respectively. The lowest H_c values, approaching 1000 A/m, are obtained in D specimens, which were processed with the lowest energy input.

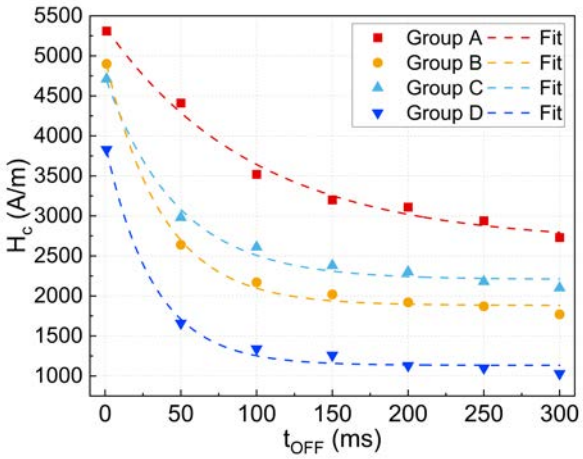

Figure 6.10. Effect of the introduction of time delays on the coercive field of the LPBF-manufactured Kuamet 6B2 prisms. The dashed lines are exponential decay fits corresponding to samples from groups A to D.

6.4. Discussion

6.4.1. Time delays as a tool to overcome the density-amorphous fraction paradox

Previous works on LPBF of Fe-based metallic glasses, which are endowed with very low GFA, have reported an inverse relationship between the relative part density and the amorphous fraction of printed parts [76–79, 82, 84–86, 90, 93, 97] . High energy LPBF conditions reportedly give rise to high density but low amorphous fractions, and low energy LPBF conditions

result in higher amorphous fractions but introduce lack of fusion defects. Since soft magnetic applications require dense and highly amorphous components, this "density-amorphous fraction paradox" poses critical challenges to the fabrication of Fe-based components by LPBF.

Significant efforts have been made in the BMG community to overcome this processability issue. For instance, Nam et al. [85] used an LPBF remelting strategy on Kuamet 6B2 to first consolidate the powder into a solid layer that was subsequently remelted. This approach yielded samples with relative densities of up to 96 % and amorphous fractions of 47 %. Zrodowski et al. [89] also implemented an LPBF double scanning strategy on Kuamet 6B2, where remelting was performed following a so-called "point-random" sequence, in which consecutive exposure points are chosen randomly at distances larger than 1 mm within the sample to avoid heat accumulation. Reportedly, such separation gives a longer time for exposed areas to cool down before an adjacent region is melted, hence minimizing devitrification. While this approach yielded samples with simultaneously high densities (94 %) and high AM % (90 %), the use of double scanning leads to very long manufacturing times, and the point-random strategy is not feasible in most commercial LPBF manufacturing systems. Additionally, this strategy presents reproducibility challenges when manufacturing complex-geometry parts.

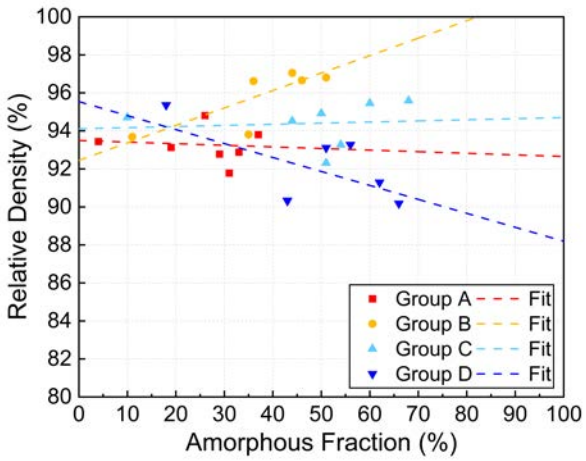

Figure 6.11. Variation of the density with the fraction of the amorphous phase in LPBF manufactured Kuamet 6B2 samples belonging to groups A to D.

In this work, a conventional meander scan strategy, with 67º interlayer rotations, which can be easily replicated in most LPBF systems, has been modified by the introduction of time delays at the end of each scan track. Fig. 6.11 illustrates the variation of the density with respect to AM % for all the Kuamet 6B2 samples manufactured within the present study. It can be seen that the use of time delays allows to improve the amorphous fraction while retaining high density

values in samples within groups A, B, and C. In group D samples, which were processed with the lowest normalized volumetric energy density, an increase in AM % of 50 % is accompanied by a decrease in density of approximately 5.5 % due to the increase in lack of fusion defects with the introduction of time delays. Even in these samples, however, the decrease in density is comparatively much smaller than that observed in earlier studies for smaller increases in AM % (Section 4.4.3).

In summary, this study demonstrates, for the first time, that a decoupling of the variations of the density and of the amorphous fraction can be achieved in Fe-based metallic glasses using a simple scanning strategy and varying only one single processing parameter (t_{OFF}). The introduction of time delays can be put forward as an effective tool to break the density/amorphous fraction paradox in these materials.

6.4.2. Understanding the relationship between the fraction of amorphous phase and H_c

In soft magnetic Fe-based alloys, coercivity is closely dependent on the amorphous fraction, grain size, and alloy composition. A higher amorphous fraction minimizes domain wall pinning by reducing grain boundaries, while nanocrystalline structures with grain sizes below 10 nm further lower coercivity due to reduced magnetocrystalline anisotropy and enhanced magnetic coupling through the amorphous matrix [57]. Additionally, compositional tuning, such as the inclusion of elements like Sn or B, can improve magnetic properties by optimizing internal stresses and magnetoelastic anisotropy [57].

Coercivity does not always decrease with an increasing amorphous fraction in Fe-based soft magnetic alloys due to the complex interplay of magnetoelastic anisotropy, internal stresses, and structural defects inherent in the amorphous matrix. While a fully amorphous structure eliminates grain boundaries that typically act as domain wall pinning centers, it introduces other sources of anisotropy, such as stress-induced magnetoelastic effects, which can hinder domain wall motion. Additionally, the absence of magnetic coupling between nanocrystals (as described by the Random Anisotropy Model) in a fully amorphous state prevents the averaging out of magnetocrystalline anisotropy, which is key to achieving ultra-low coercivity in nanocrystalline systems [144].

Fig. 6.12 shows the variation of the coercive field with respect to AM % in the Kuamet 6B2 LPBF-manufactured specimens belonging to groups A to D. The data corresponding to a

SWAP-atomized powder and to a melt-spun ribbon of the same composition are plotted as a reference. In general, an inverse linear dependency between H_c and AM %, with a slope of -71 A/m, is observed when AM % $\leq$ 45 %, in agreement with Section 4.3.2. This AM % range includes all samples within groups A and B and the samples processed with 1 and 50 ms time delay from groups C and D. For processing conditions where AM % > 45 %, however, H_c becomes less dependent on AM %. This AM % range includes samples from groups C and D with time delays higher than 50 ms. In these samples, increases in AM % from around 50 to 70 % lead only to comparatively minor variations of H_c. Additionally, samples from group D are characterized by coercivity values stabilizing around 1 kA/m. This behavior may arise from multiple factors that are beyond the scope of the present work. Notably, all samples still exhibit a relatively high crystalline fraction (not less than 30 %), mostly dominated by the Fe_3Si phase as shown in Section 4.3.2, and which may also contain a minor presence of boride phases such as FeB, Fe_2B, and Fe_2B. These phases are known to significantly influence the magnetic properties of Fe-based soft magnetic alloys by increasing coercivity and reducing permeability [144], which likely accounts for the absence of further coercivity reduction beyond the observed plateau at 1 kA/m.

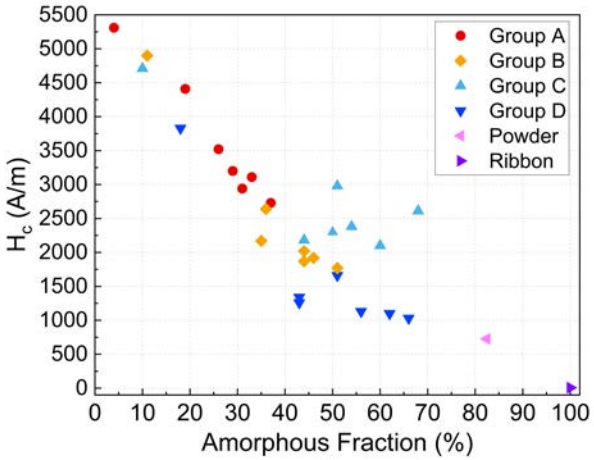

Figure 6.12. Variation of the coercive field with respect to the amorphous fraction in the Kuamet 6B2 LPBF-manufactured specimens. The data corresponding to a SWAP-atomized powder and a melt-spun ribbon of the same composition are plotted as a reference.

6.5. Conclusions

The aim of this study is to investigate the impact of introducing time delays (laser switch-off times) after each scan track of an LPBF meander scanning strategy on the processability,

density, crystallinity, and coercive field of Fe-based Kuamet 6B2 specimens. With that goal, LPBF is performed using two laser power levels (120 W and 160 W), two scan speeds (615 mm/s and 888 mm/s), and time delays ranging from 50 to 300 ms. Multiphysics FEM simulations are utilized to rationalize the influence of time delays on the temperature evolution and on crystallization during LPBF. The following conclusions can be drawn from this work:

1. Introducing time delays improves processability and dimensional accuracy in the samples manufactured with the highest normalized energy density (group A, with P = 160 W and v = 615 mm/s), reducing warping and delamination effects.

2. Glass/crystalline composites were obtained for all investigated LPBF conditions. The addition of time delays increases the amorphous fraction in the LPBF manufactured samples without compromising density. The most pronounced increases in the amorphous fraction are observed for time delays as short as 50 ms.

3. The introduction of time delays results in a lower T_0 in the solidified amorphous regions which, in turn, experience a lower degree of devitrification during subsequent laser passes. Although increasing time delays lead to progressively lower degrees of devitrification, the most pronounced change in the fraction of devitrified material occurs for time delays as short as 50 ms.

4. A strong inverse linear dependency exists between H_c and the amorphous fraction when the latter is smaller than 45 %; for higher fractions the dependency is significantly less pronounced.

5. The introduction of time delays is presented as a strategy with high potential to resolve the "density/amorphous fraction" paradox in Fe-based MGs, providing guidelines for LPBF manufacturing of these alloys for soft magnetic applications.

7. LPBF OF THE FE-SI-B-NB-NI ALLOY, A MG SYSTEM WITH ENHANCED GLASS-FORMING ABILITY

7.1. Background

Chapter 6 presented a the implementation of time delays as a tool with a double purpose: to improve the amorphous fraction retained after printing without compromising the part density while simultaneously improve the print stability of Kuamet 6B2 specimens. As discussed, Kuamet 6B2 is a commercial glass-forming composition with excellent soft magnetic properties in the fully amorphous state. However, due to its poor GFA, devitrification is unavoidable during LPBF processing, making the lowest H_c three orders of magnitude higher than that of fully amorphous ribbons of the same composition. It is evident that a better glass former is needed to achieve the full potential of soft magnetic metallic glasses.

This work presents the first LPBF parameter study on a recently patented Fe-based system, which possesses a d_c of > 1 mm, an order of magnitude higher than Kuamet 6B2 (d_c = 120 μm) and similar commercially available alloys, without the use of P, Co or rare earth elements as alloying elements. Three approaches were taken: (i) the exploration of changes of laser power and scan speed, (ii) the consecutive remelting of the upper layer and (iii) the implementation of time delays. The influence of variations in processing parameters or scan strategies on the internal defects, (micro)structure and magnetic properties were studied. The aim of processing this alloy with LPBF is to begin to explore its viability as a substitute for soft magnetic materials currently used in electric motors, since the combination of material properties presented by the alloy and the flexibility of additive manufacturing opens the door to producing highly efficient electrical machines.

7.2. Methods

In this chapter, the of the feedstock powder employed was an Fe-Si-B-Nb-Ni alloy and the RenAM500Q Flex system was used for LPBF manufacturing. Three sets of processing parameters (termed hereafter S, R, and J-series) were used to fabricate $8 \times 8 \times 5.4$ mm^3 cuboid

specimens. Fig. 7.1 shows a schematic of the different series of samples and Table 7.1 details the parameters used for each sample. For all three groups, constant values were assigned to the layer thickness (t = 30 μm), hatch distance (h = 80 μm) and point distance (pd = 80 μm). The S-Series P and t_{ON} values ranging from 100-180 W and 80-120 μs, respectively. t_{OFF} was fixed at 50 ms, as it was shown in Chapter 6 that this parameter contributes towards reducing warping and delamination at combinations of high power and low exposure time on Kuamet 6B2. In the R-series a double scanning strategy was used, where the power was fixed at 140 W and the exposure time at 100 μs for both scans, and the direction of the remelting scan tracks was rotated by 0°, 30°, 45° and 90° with respect to the first scan tracks. This angle will be hereafter referred to as the re-scan angle. Finally, in the J-series the power and the exposure time were also fixed at 140 W and 100 μs, respectively, and a time delay was introduced at the end of each track within the range of 20 ms to 200 ms.

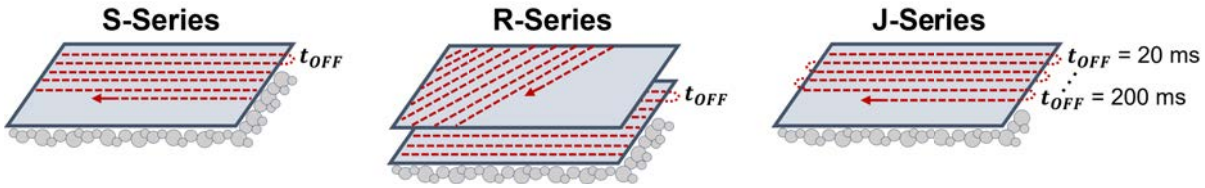

Figure 7.1. Schematic of printing strategy for each sample group.

Table 7.1. Summary of processing parameters varied during S-, R- and J-series.

Sample	P (W)	t_{ON} (μm)	v (mm/s)	Re-scan offset (º)	t_{OFF} (ms)
S1	180	120	615	–	50
S2	180	100	730	–	50
S3	180	80	890	–	50
S4	140	120	615	–	50
S5	140	100	730	–	50
S6	140	80	890	–	50
S7	100	120	615	–	50
S8	100	100	730	–	50
R1	140	100	730	0	50
R2	140	100	730	30	50
R3	140	100	730	45	50
R4	140	100	730	90	50
J1	140	100	730	–	20
J2	140	100	730	–	30
J3	140	100	730	–	40
J4	140	100	730	–	50
J5	140	100	730	–	75
J6	140	100	730	–	200

7.3. Results

7.3.1. Internal Defects

Fig. 7.2 contains optical micrographs of cross-sections parallel to BD of all manufactured samples, and it provides a two-dimensional view of the internal defect structure. The values of the density and of the area fraction of pores and cracks, calculated by image analysis of these micrographs, are compiled in Table 7.2. Fig. 7.3 shows the variation of the area fraction of porosity with P and v (Fig. 7.3a, S-series), with the rotation angle (Fig. 7.3b, R-series), and with the delay time (Fig. 7.3c, J-series). In the S-series, as displayed on Fig. 7.3a, the highest porosity (7.6 %) resulted from the lowest energy combinations of parameters (P = 100 W and t_{ON} = 80 μs). As the values for both parameters increased, the porosity was progressively reduced, with the exception of the combinations of highest power input of P = 180 W and medium or high exposure times of t_{ON} = 100 μs (S2) and t_{ON} = 120 μs (S1), where samples present large, sparsely distributed voids with irregular shapes (Fig. 7.2). As displayed on Fig. 7.3b, in the R-series the smallest porosity (1.5 %) was found when the directions of the first and second laser scans were perpendicular (re-scan angle = 90º), and the highest porosity (4.5 %) was measured

when they were parallel (re-scan angle = 0º). Fig. 7.3c shows an increase of porosity in the J-series prints as a function of t_{OFF}, from 2.1 % when t_{ON} = 20 ms to 6.4 % when t_{ON} = 200 ms. All samples contain a relatively high number of cracks, oriented mostly at low angles with respect to the BD. The crack area fraction measurements performed on OM images showed a small variation between processing parameter and scan strategy combinations. The lowest (0.5 %) was measured in sample J5, processed with one of the highest delay times explored in this study. Conversely, the highest crack area fraction (1.5 %) was measured in sample R4, which was processed with a 90º angle between the first and second scan. Internal cracks presented lengths below 300 μm, regardless of the processing conditions.

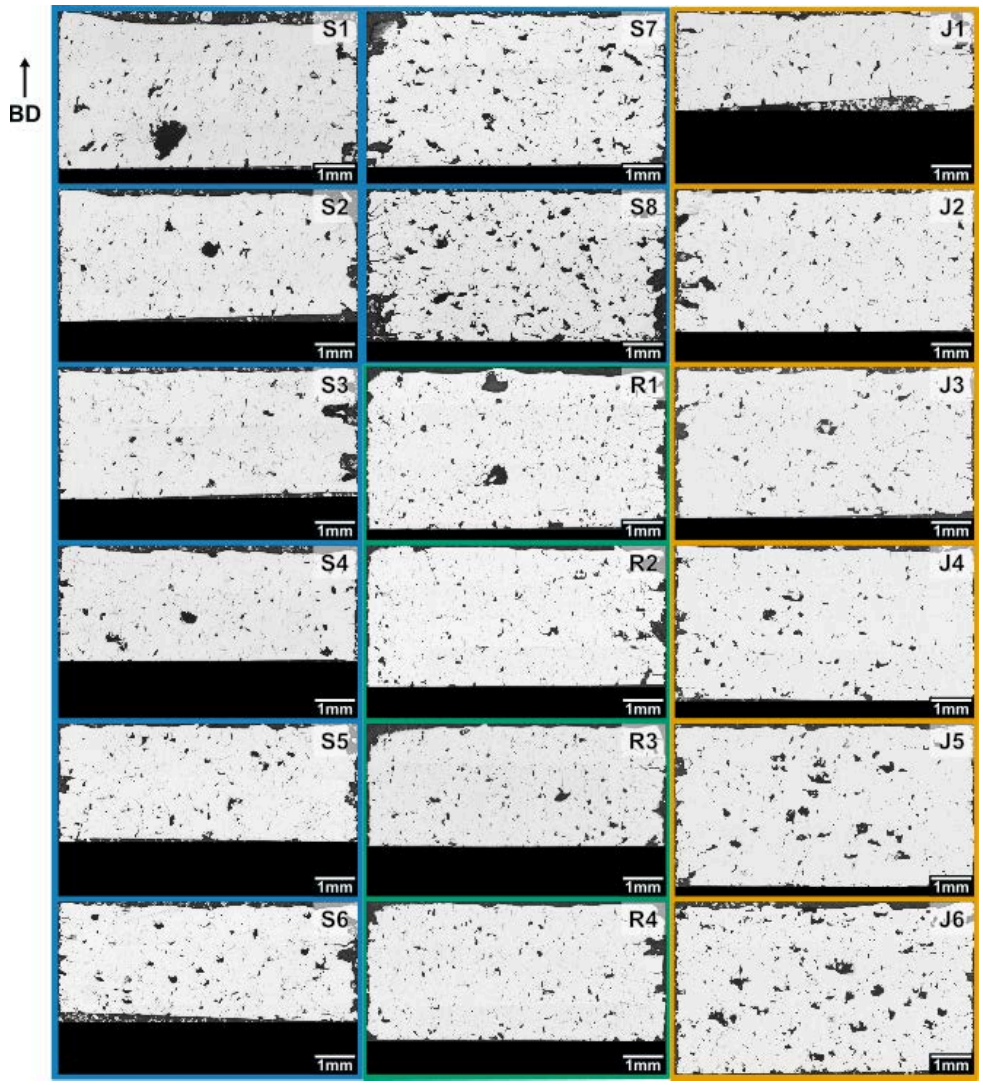

Figure 7.2. Optical micrographs along planar cross-sections of all the Fe-Si-B-Nb-Ni samples processed by LPBF. The vertical axis of all micrographs corresponds to the build direction (BD). Images corresponding to samples manufactured with different conditions are highlighted with different colors: S-series (blue), R-series (green), J-series (yellow).

A 3D quantification of the defect structure was carried out in samples J1 and J6 by XCT.

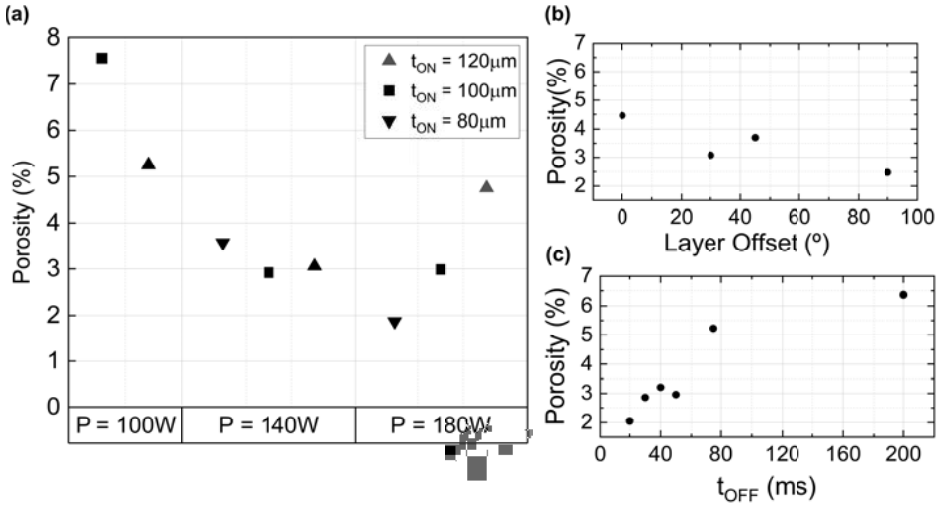

Figure 7.3. Area fraction of porosity, measured by image analysis of the optical micrographs of Fig. 7.2, as a function of (a) P and t_{ON} (S-series), (b) the re-scan angle between the first and second laser scans (R-series), and (c) the time delays (J-series).

Table 7.2. Density and area fraction of different defect-types, measured by image analysis of OM images, of samples belonging to the S-, J- and R-series.

Sample	Porosity (%)	Crack Volume (%)	Relative Density (%)
S1	4.8	1.0	94.3
S2	3.0	0.8	96.2
S3	1.9	1.0	97.1
S4	3.1	1.0	96.0
S5	2.9	1.1	96.0
S6	3.6	1.2	95.3
S7	5.3	1.1	93.7
S8	7.6	1.7	90.8
R1	4.5	1.5	93.9
R2	3.1	1.3	95.7
R3	3.7	1.5	94.8
R4	2.5	1.5	96.0
J1	2.1	0.9	97.0
J2	2.9	0.8	96.3
J3	3.2	0.9	95.9
J4	3.0	0.6	96.5
J5	5.2	0.5	94.3
J6	6.4	1.0	92.6

These samples were selected as they were processed, respectively, with the minimum and maximum delay times within the J-series, exhibiting widely differing values of the area fraction of porosity (Fig. 7.3). Figs. 7.4 and 7.5 illustrate $2 \times 2 \times 1$ mm^3 segmented volumes corresponding to bulk material, colored semi-transparent gray, voids, colored blue and cracks, colored red in samples J1 and J6, respectively. Fig. 7.4a,b and Fig. 7.5a,b include the three features overlayed

in the same volume while Fig. 7.4c and Fig. 7.5c present the isolated voids and Fig. 7.4d and Fig. 7.5d show the network of internal cracks for each sample. It can be seen that the porosity increases significantly as the time delay increases (Fig. 7.4a-c and Fig. 7.5a-c). As shown on Fig. 7.4c, small voids are sparsely distributed throughout sample J1, while voids with a wider size distribution are present in sample J6. The corresponding volume fractions, 0.1 % and 5.1 %, respectively, are lower than the fractions measured from OM micrographs (2.1 % and 6.4 %, respectively). Fig. 7.4d and Fig. 7.5d confirm that the morphology and distribution of internal cracks is similar on both samples. The corresponding volume fractions, 7.4 % and 4.8 %, respectively, are significantly higher than the area fractions measured from OM micrographs (0.9 % and 1.0 %). While the vertical length of cracks in the 2D OM images appeared to be mostly smaller than 300 μm (i.e. approximately the height of 10 layers), 3D XCT data confirms that in the direction perpendicular to the BD cracks may exceed 2 mm in length (Fig. 7.4a).

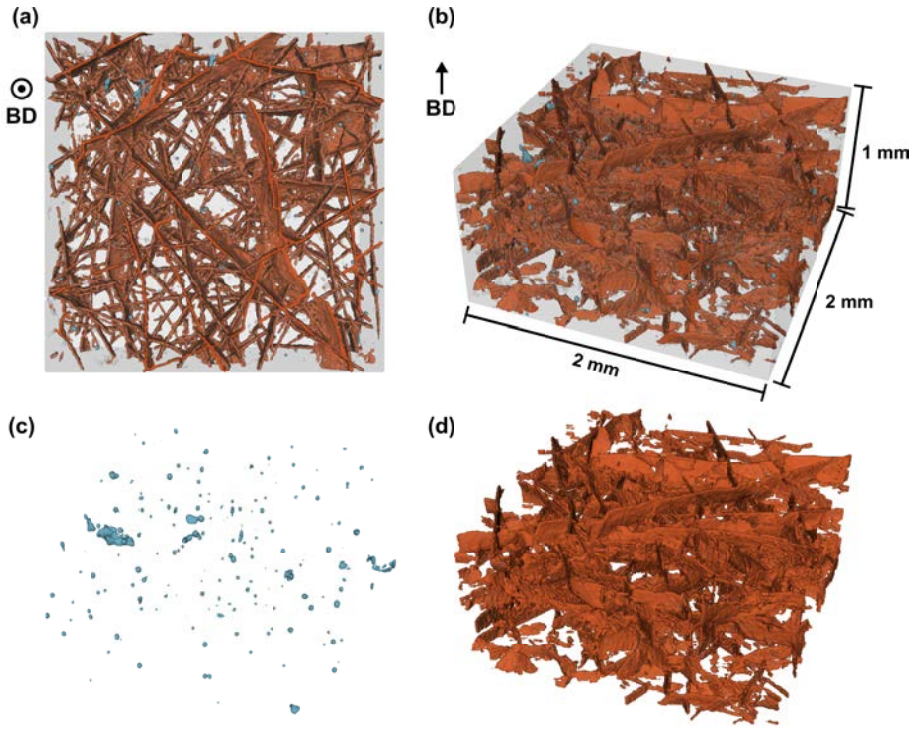

Figure 7.4. 3D defect structure corresponding to the J1 sample. The build direction is labeled as BD. Voids are colored in blue, cracks are colored in red, and the bulk material is colored in semi-transparent gray. (a) Top view; (b) 3D view; (c) segmented pores; (d) segmented cracks.

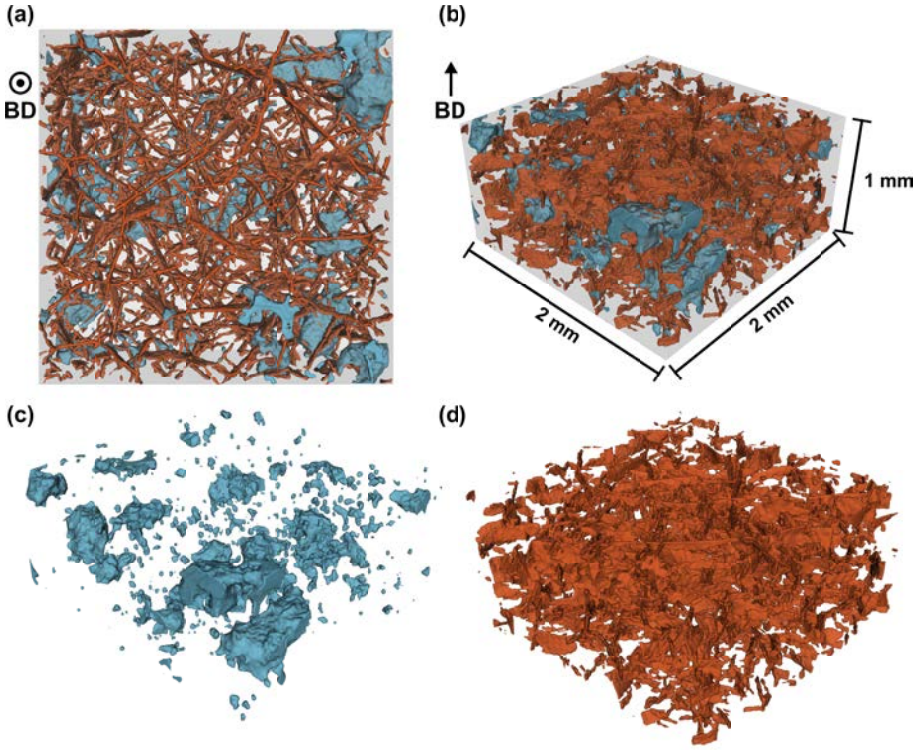

Figure 7.5. 3D defect structure corresponding to the J6 sample. The build direction is labeled as BD. Voids are colored in blue, cracks are colored in red, and the bulk material is colored in semi-transparent gray. (a) Top view; (b) 3D view; (c) segmented pores; (d) segmented cracks.

The difference in the measured 2D and 3D void fractions might be attributed to the detachment of solid pieces from the surface during sample grinding due to the high concentration of internal cracks, leading to artificially enhanced porosity in optical micrographs. On the other hand, cracks in 2D measurements were grossly underestimated. It is believed that the limited resolution of OM methods, in combination with sample preparation, affected the visibility of micro-cracks.

7.3.2. (Micro)structure

Several complementary measurements were performed to examine the (micro)structure of the manufactured samples and to detect the potential presence of grains at different length scales. Fig. 7.6 displays the XRD patterns corresponding to samples belonging to the S-series (Fig. 7.6a), R-series (Fig. 7.6b), and J-series (Fig. 7.6c). Samples belonging to the R-series (Fig. 7.6b) exhibit a single wide hump at 45°, and they can thus be considered XRD amorphous. S-series samples (Fig. 7.6a), with the exception of S8, which is also XRD amorphous, and J-series specimens (Fig. 7.6c), exhibit a superposition at 45° of a wide hump and a Fe(Si) sharp crystalline peak, revealing the presence of a crystalline/amorphous composite. The crystalline

peak in the J-series samples decreases in intensity with increasing time delay.

The DSC up-scans presented on Fig. 7.7 for all manufactured samples, as well as for the atomized powder and for a melt-spun ribbon of the same composition, provide a macroscopic measurement of the heat flow upon heating for each set of conditions. A deep and narrow endothermic peak is present in the scans of all printed samples, whereas the reference feedstock powder and melt-spun ribbon of the same material exhibit a wider and shallower peak. In particular, the ribbon's curve has a shoulder to the right of the main crystallization peak, indicating a secondary crystallization event. This makes the quantification of the crystallization enthalpy (ΔH_{cr}), and thereby of the amorphous fraction, non-trivial, as the baseline of the ribbon's curve is not completely flat. The value of ΔH_{cr} and the AM % estimated with respect to the ribbon are reported in Table 7.3 for all manufactured samples. The presence of values higher than 100 % for some conditions results from the difficulty in estimating the enthalpy corresponding to the ribbon due to the presence of a double crystallization peak. In any case, this estimation reveals, qualitatively, that the amorphous fraction is in all cases very large.

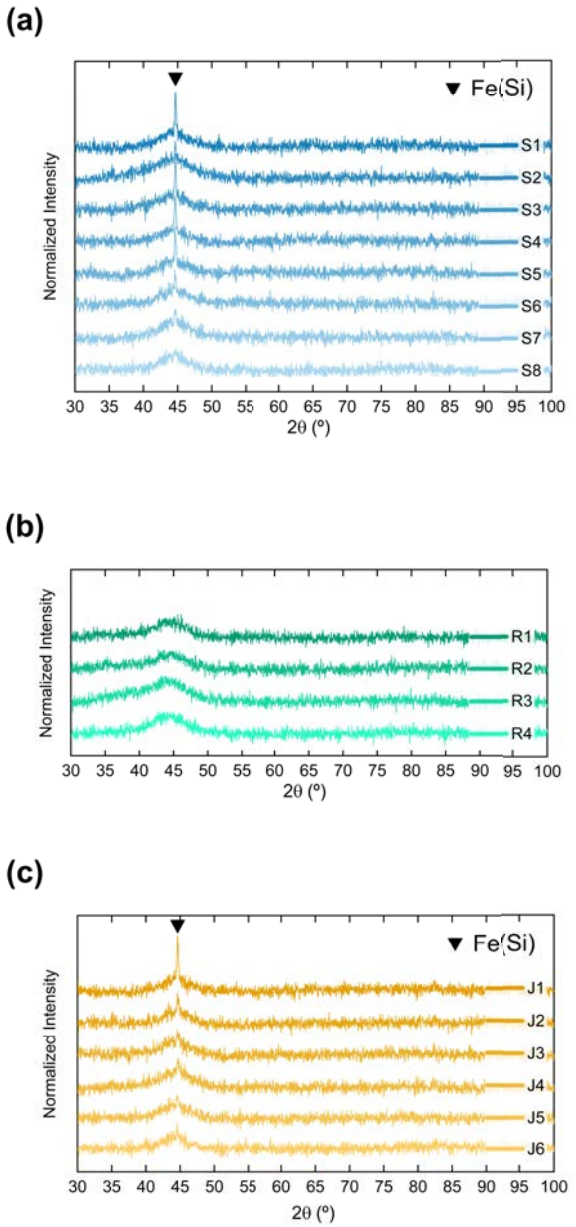

Figure 7.6. X-ray diffraction patterns corresponding to all printed samples. (a) S-series; (b) R-series; (c) J-series. All samples exhibit an amorphous hump at 45°, and some samples have an overlaid peak corresponding to the crystalline Fe(Si) phase (black inverted triangle).

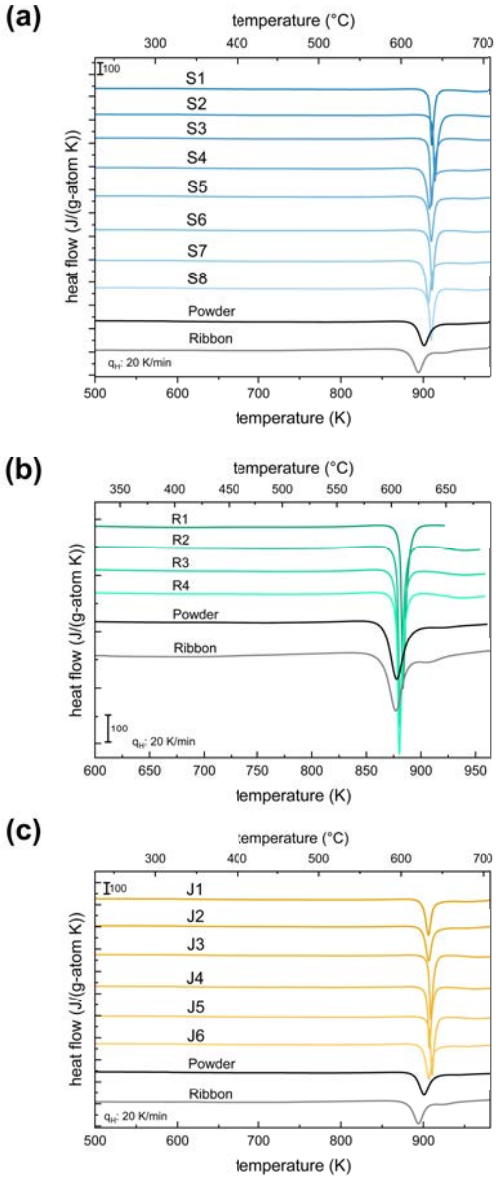

Figure 7.7. Differential scanning calorimetry scans corresponding to all the printed Fe-Si-B-Nb-Ni samples. The curves corresponding to atomized powders and a melt-spun ribbon of the same composition are added for reference. (a) S-series, (b) R-series, and (c) J-series.

Table 7.3. Crystallization enthalpy along with the corresponding estimated amorphous fractions corresponding to samples belonging to S-, J- and R-series.

Sample	Cryst. Enthalpy (J/g atom)	Estimated AM (%) (Ribbon as ref.)
S1	3100 ± 200	89.9 ± 5
S2	3700 ± 200	107.2 ± 5
S3	3700 ± 200	107.2 ± 5
S4	3050 ± 200	88.4 ± 5
S5	3050 ± 200	88.4 ± 5
S6	3350 ± 200	97.1 ± 5
S7	3000 ± 200	87.0 ± 5
S8	3250 ± 200	94.2 ± 5
R1	3450 ± 200	100.0 ± 5
R2	3350 ± 200	97.1 ± 5
R3	3350 ± 200	97.1 ± 5
R4	3300 ± 200	95.7 ± 5
J1	3150 ± 200	91.3 ± 5
J2	3150 ± 200	91.3 ± 5
J3	3550 ± 200	102.9 ± 5
J4	3400 ± 200	98.6 ± 5
J5	3350 ± 200	97.1 ± 5
J6	3100 ± 200	89.9 ± 5
Powder	3250 ± 200	94.2 ± 5
Ribbon	3450 ± 200	-

A detailed multiscale (micro)structural characterization was carried out in samples S5 and R1 with the aim of exploring the potential presence of ultrafine and nanocrystallites. These two samples were manufactured using the same LPBF parameters but in S5 a single scan was carried out in each layer whereas R1 was processed using the remelting strategy with a re-scan angle of 0° between the first and second laser passes. Fig. 7.8 illustrates EBSD band contrast (Fig. 7.8a,c,e-h) and inverse pole figure maps (Fig. 7.8c,d,g,h) for samples S5 (Fig. 7.8a,c, e-h) and R1 (Fig. 7.8b,d). The maps on Fig. 7.8a-d were acquired at representative centrally located regions of the two investigated samples; the maps on Fig. 7.8e-h were acquired at a border region of sample S5 at different magnifications. This border area has been explored in more detail because of the highest likelihood of devitrification as the time between consecutive laser passes is very small. The resolution limit is approximately 360 nm for the low magnification images (Fig. 7.8a-e,g) and 90 nm for the high magnification images (Fig. 7.8f,h). No trace of crystalline phases was found on any of the examined regions, as can be inferred from the black band contrast maps and the virtually-zero indexed IPF maps.

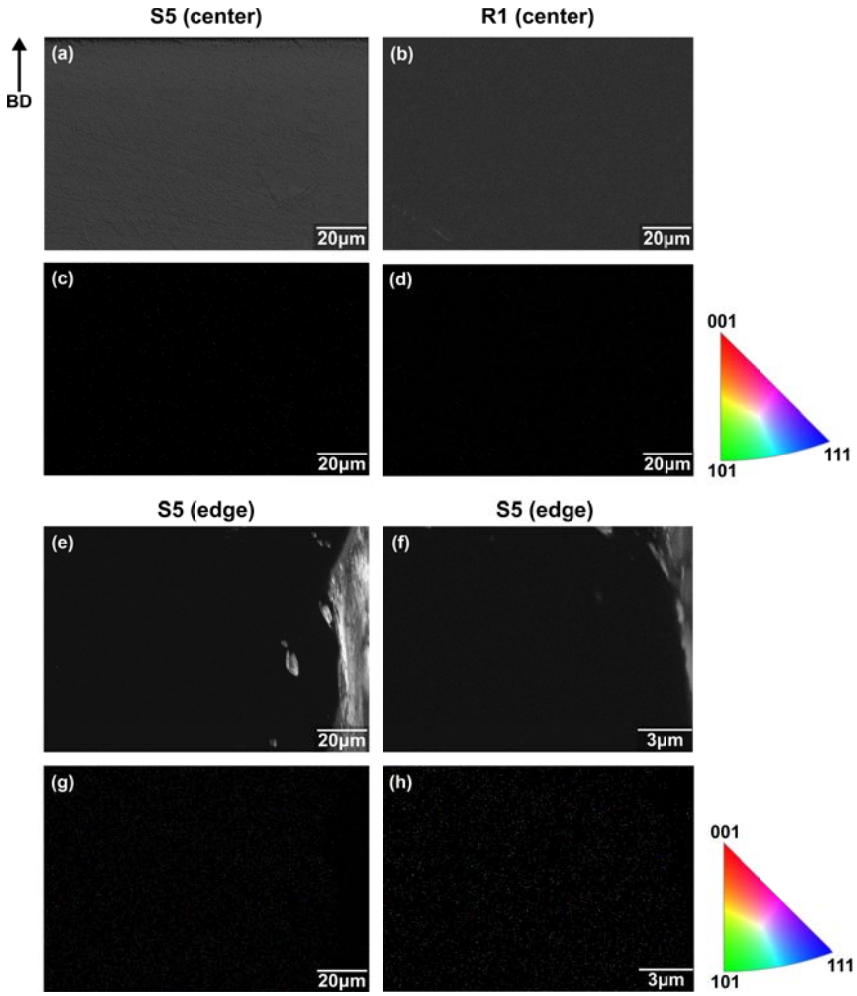

Figure 7.8. EBSD examination of (a,c,e-h) S5 and (b,d) R1 samples: (a,b,e,f) band contrast maps and (c,d,g,h) IPF maps of the build direction (BD). The light regions in (e,f) correspond to the edge of the sample.

Transmission electron microscopy was also carried out at different magnifications on the same samples that were examined by EBSD (S5 and R1, Fig. 7.9). Both lamellae exhibited Cu contamination in the bottom edge (dark contrast in Fig. 7.9a,b) due to unwanted deposition during the last stages of FIB thinning. The high concentration of Cu in the lower edge of both lamellae was confirmed by TEM-EDX and these regions were therefore excluded from further analysis. In all other areas of both lamellae no signs of crystalline features were found. FFT transforms of the high-resolution images of Fig. 7.9c,d (included as insets) exhibited only the diffuse halo characteristic of a disordered atomic structure, in the absence of any bright spots, which would have indicated the presence of long-range atomic ordering.

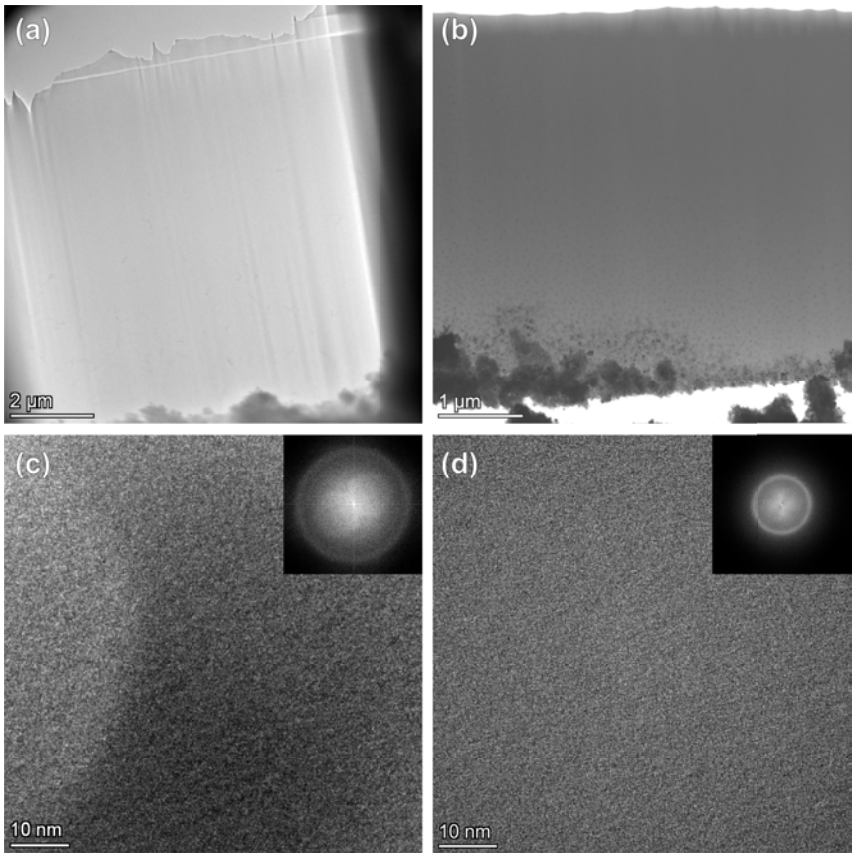

Figure 7.9. Bright field transmission electron microscopy images at different magnifications of lamellae corresponding to (a,c) S5 and (b,d) R1 samples. Insets in (c,d) are fast Fourier transform patterns from their corresponding image.

To further investigate the presence or absence of a compositional segregation or nano-scale phases at the near-atomic scale APT analysis was conducted for samples S5 and R1. Fig. 7.10 shows APT reconstructions from sample S5 (Fig. 7.10a) and R1 (Fig. 7.10b). All elements followed the binomial distribution, which indicates that they are randomly arranged within the material. This is further confirmed by the Pearson coefficient, μ, which is given in Table 7.4, which is used to reveal statistical deviation from randomness. The Pearson coefficient is indicated with values between 0 and 1, where 0 represents a random distribution and 1 reveals a statistical compositional segregation. It is evident that for all the elements the distribution is random.

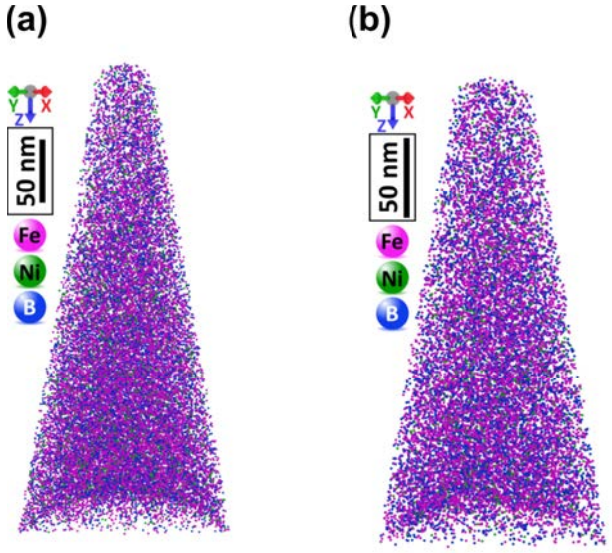

Figure 7.10. APT reconstructions of selected elements (Fe, Ni, B) from (a) S5 and (b) R1 samples.

Table 7.4. Pearson coefficients (μ) for Fe, Si, B, Nb, and Ni as calculated from the APT elemental distributions for the samples S5 and R1.

Element	S5 sample	R1 sample
Fe	0.0291	0.0263
Si	0.0160	0.0149
B	0.0638	0.0576
Nb	0.0072	0.0098
Ni	0.0094	0.0082

The absence of any grains or clustering of elements in the S5 regions examined by EBSD, TEM and APT suggests that the grains that were detected by XRD in this specimen (Fig. 7.6) are not homogeneously distributed throughout the sample. It is suspected that the crystalline regions in samples like S5 are located at the edges of the cube, as this is the turning point of the laser and more heat is accumulated during fabrication. Regardless of the location, the size of said crystals must be below the resolution limit of the EBSD technique (< 90 nm) and their composition is α-Fe(Si) or Fe_3Si, according to the XRD results.

7.3.3. Mechanical Properties

The local mechanical behavior of the same two selected samples (S5 and R1) was also investigated via nanoindentation in order to establish a connection between the processing parameters, the (micro)structure, and structural properties such as the Young's modulus and the hardness. Fig. 7.11 illustrates the hardness (Fig. 7.11a,b) and Young's modulus (Fig. 7.11c,d) maps corresponding to samples S5 (Fig. 7.11a,c) and R1 (Fig. 7.11b,d). Sample S5 shows

a comparatively more heterogeneous hardness and Young's modulus distribution, with average values of 11.6 ± 4.6 GPa and 198.6 ± 63.5 GPa, respectively. The homogeneous spatial distribution of local maxima and minima in the hardness (Fig. 7.11a) and Young's modulus (Fig. 7.11c) maps reveals that the observed scatter cannot be attributed to devitrification at the heat affected zones surrounding the solidified melt pools, as was the case with Kuamet 6B2 (see Chapter 5, Fig. 5.6). Instead, it is likely that it can be attributed to a heterogeneous distribution of internal stresses in the as-built condition. In contrast, sample R1, which was processed using the same P and t_{ON} conditions, but with the described re-melting approach, exhibits a more homogeneous hardness and Young's modulus distribution, with average values of 12.0 ± 2.5 GPa and 201.1 ± 29.3 GPa, respectively. It is our contention that the smaller scatter in R1 might be attributed to the partial relief of residual stresses during the remelting step, as reported earlier for other materials [17, 145].

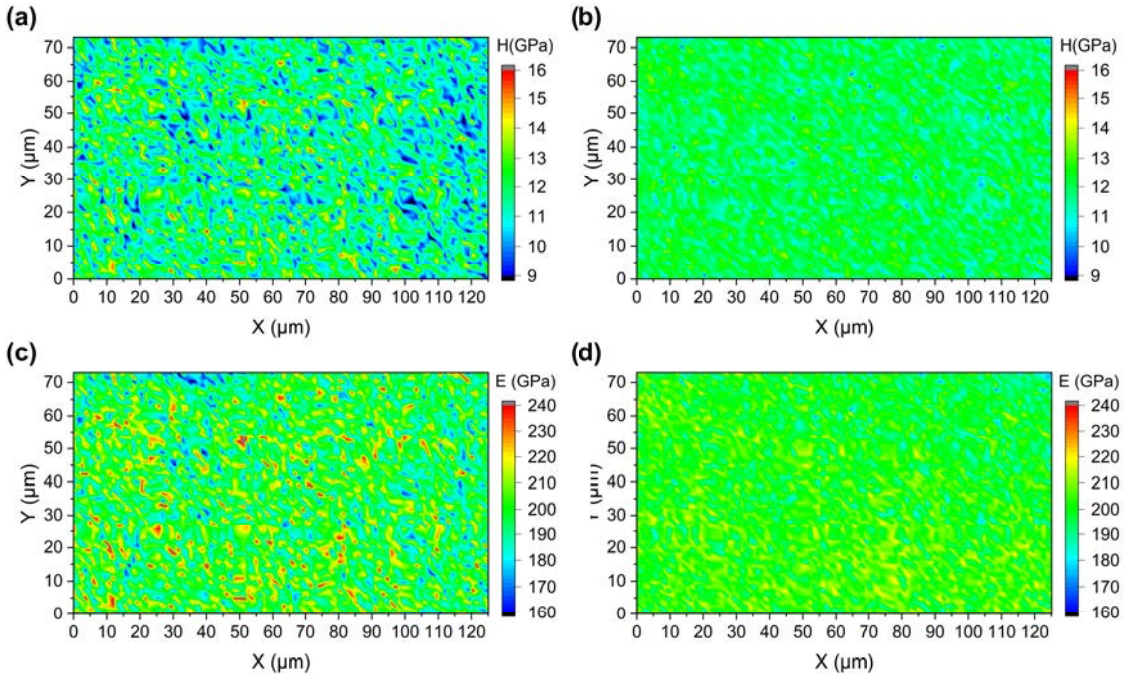

Figure 7.11. Hardness and Young's modulus maps from nanoindentation experiments on two selected samples: (a,c) S5 and (b,d) R1.

7.3.4. Magnetic Properties

Fig. 7.12 presents the magnetic hysteresis loops obtained from vibrating sample magnetometer measurements, under quasi-dynamic conditions. The magnetic properties obtained from such curves are summarized in Table 7.5. The coercive field is similar for all samples, being

lowest for sample J1, which had the lowest applied time delay (t_{OFF} = 30 ms). It is worth noting that the measured coercivity values are close to the sensitivity limit of the VSM instrument. The saturation magnetization was found to be very similar among all samples, between 122 Am^2/kg and 126 Am^2/kg. The magnetic permeability has not been calculated due to the variability in sample shape and the complexity of deriving the demagnetizing factor. However, the steepest slopes in the hysteresis loops, which are directly proportional to the permeability, correspond to S1, S2, R1 and J1, which are also the samples with lowest H_c within each series.

Table 7.5. Magnetic properties of Fe-Si-B-Nb-Ni samples processed by LPBF.

Sample	Coercive field (A/m)	Saturation magnetization (Am^2/kg)
S1	52	124
S2	49	125
S3	54	125
S4	63	126
S5	58	125
S6	65	125
S7	62	125
S8	65	125
R1	62	122
R2	63	122
R3	77	122
R4	67	122
J1	44	126
J2	56	125
J3	52	125
J4	60	124
J5	61	123
J6	72	123

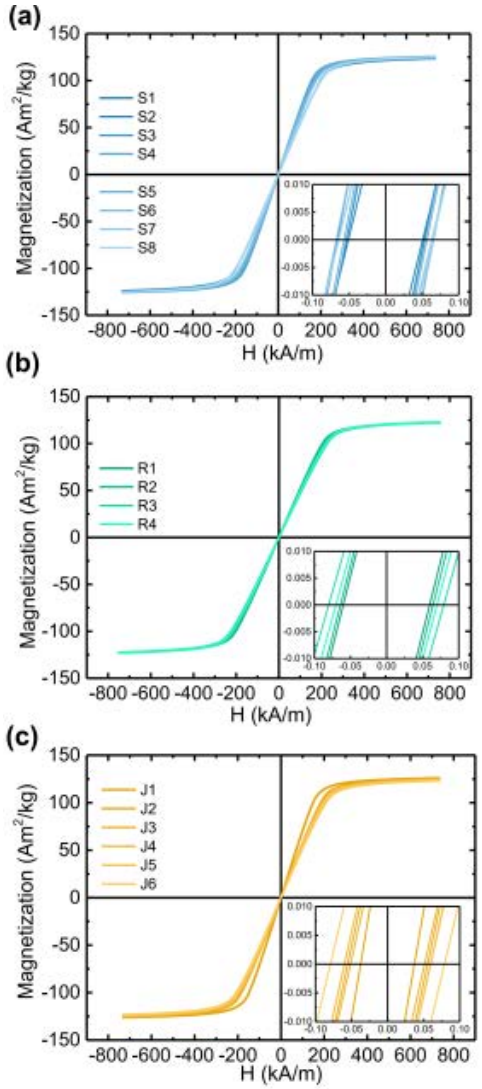

Figure 7.12. Room-temperature magnetic hysteresis loops measured by VSM: (a) S-series, (b) J-series and (c) R-series. Insets on each plot show a magnified view of the intersection of the magnetization curve with the vertical axis around the origin, providing a clearer view of H_c.

7.4. Discussion

7.4.1. Influence of time delays

Chapter 4 and similar works on LPBF of commercial Fe-based MG compositions have reported that, when AM % is smaller than 50 %, the presence of crystalline phases in the printed samples was the main contributor towards the increase of the coercive field [85, 86]. Fig. 7.13 presents the evolution of the coercive field, the amorphous fraction, and the area fraction of porosity with increasing time delay in the J-series samples. It can be seen, first, that, while the coercive field and the porosity increase with increasing time delay, this trend is not observed in

the amorphous fraction. Thus, our results reveal that, once very large AM % values are reached, the magnetic domain wall movement might be controlled by other factors, such as the internal defects [86]. It must be mentioned here that other factors that have not been measured in this work are also capable of domain wall pinning, including residual stresses and magnetostriction [65]. Indeed, work on melt-spun ribbons of the same composition has shown that heat treatment at temperatures below the crystallization temperature (T_x) of the alloy can relieve residual stresses without causing devitrification and further decrease H_c [146–148]. Studying the effect of different annealing treatments in LPBF-manufactured samples is a relevant and promising area for future research.

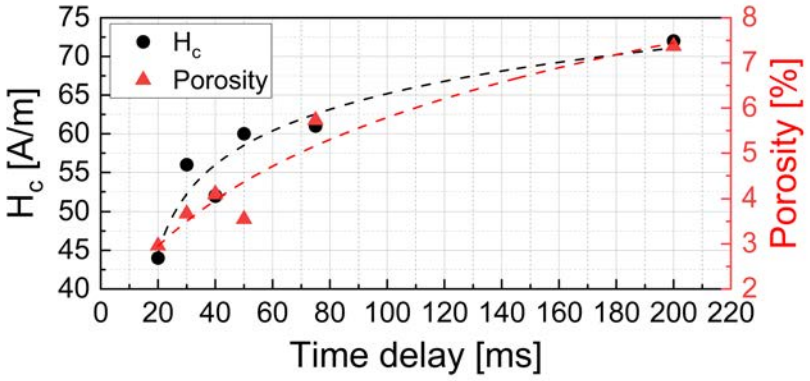

Figure 7.13. Coercivity (black axis, circles) of printed samples measured by VSM and porosity (red axis, triangles) measured by optical microscopy and image analysis as a function of time delays. Logarithmic fits have been included as dashed lines.

7.4.2. Progress in additive manufacturing of soft magnetic materials

Fig. 7.14 compares the H_c values of the Fe-Si-B-Nb-Ni LPBF-manufactured samples of this study with those of other soft magnetic materials processed using different additive manufacturing methods. The reviewed works include four alloy groups: crystalline systems based on Fe-Co [149–151], on Fe-Ni [152–155], and on Fe-Si [156–158], and Fe-based glass-forming alloys [78, 85–87, 89, 90] without P, Co or rare earths. Kustas et al. [150] and Yang et al. [149, 151] processed coarse-grained Fe-Co alloys by laser-based direct energy deposition (DED) with minimum H_c of 1000 A/m due to the precipitation of Fe_3B phase [151] and a M_s as high as 220 Am^2/kg [150]. Mikler et al. [154] and Li et al. [155] manufactured Fe-Ni specimens by LPBF and DED with coercivities of 390 A/m and 200 A/m, respectively. However, such improvement in H_c with respect to Fe-Co alloys typically comes at the expense of the saturation magnetization values, which were reported to be 82 Am^2/kg [154] and 60 Am^2/kg [155] due to the lower

Fe content. Fe-Si alloys processed by additive manufacturing have shown lower H_c values than Fe-Ni systems without compromising the saturation magnetization. Goll et al. [156] reported H_c values for these systems as low as 100 A/m in the as-printed state with saturation magnetization values of 149 Am^2/kg. Post-processing can further enhance the magnetic properties and in a recent study by Lamichhane et al. [159], hot isostatic pressing, annealing and electrical discharge machining, enabled the fabrication of a laminated motor stator with H_c = 40 A/m and M_s = 232 Am^2/kg.

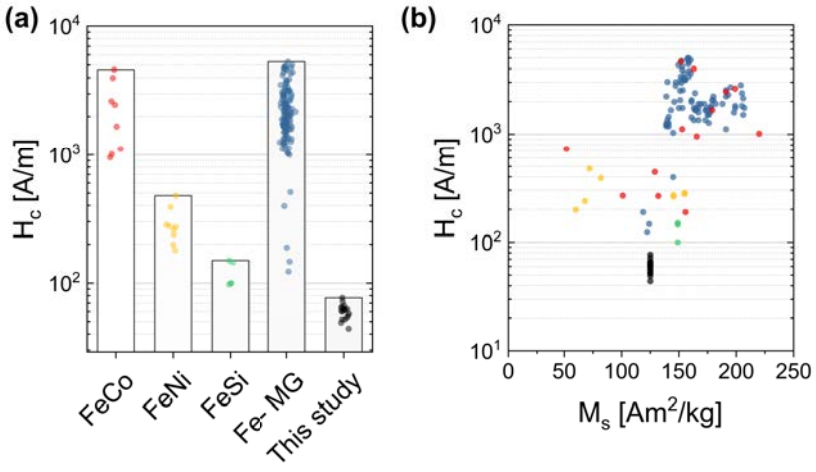

Figure 7.14. Comparison of (a) H_c and (b) M_s values reported in Chapter 4, in Chapter 6 and in the literature for different alloy systems and AM manufacturing techniques [78, 85, 86, 89, 90, 149–154, 156–158] to those obtained in the LPBF-manufactured Fe-Si-B-Nb-Ni alloy investigated in this chapter. The reported values include only as built material for comparison with this work.

The alloy presented in this work, when processed by LPBF, has shown coercive field values as low as 44 A/m, an unprecedented level for additively manufactured Fe-based metallic glasses (Fig. 7.14a). This value is two orders of magnitude lower than that reported in Chapter 4, Chapter 6 and other works on commercial Fe-based alloys when simple scanning strategies were used [86, 87, 90], and one order of magnitude lower than those reported for complex scanning strategies [78, 85, 89]. Such improvement is mainly attributable to the relatively high GFA of the alloy (approaching 1 mm), which increased the resistance to devitrification and, in particular, avoided the formation of boride phases, which can pin the magnetic domain wall movement [144]. However, this comes at the expense of the saturation magnetization, which is lower than that of the Fe-Co, Fe-Ni, and Fe-Si crystalline alloys, as well as of the commercial Fe-based Mg alloys, due to the lower Fe content, as depicted in Fig. 7.14b.

Finally, another widely used soft magnetic material, not included in Fig. 7.14, are soft ferrites. Mn-Zn ferrites exhibit extremely low H_c values (H_c < 20 A/m) and are thus suitable

for high-frequency power supplies [160]. Nevertheless, they typically have a low saturation magnetization (Ms < 85 Am^2/kg), which makes them unsuitable for many other applications. Additive manufacturing of ferrites was attempted to gain flexibility in design [161] and to tune the magnetic properties [161, 162]. However, the processed samples possessed relatively high H_c values (H_c > 1900 A/m).

7.5. Conclusions

Most works on LPBF of Fe-based metallic glasses free of P, Co or rare earths to date have reported magnetic coercivity values as low as 1110 A/m using simple scanning strategies [87] and 397 A/m using complex ones [89]. This study explores for the first time the processing-defect structure-(micro)structure-property relationship for LPBF of a newly designed Fe-Si-B-Nb-Ni glass-forming alloy with superior GFA. Several scanning strategies, including the use of time delays at the end of laser tracks in a meander path, and remelting steps, as well as a thorough multiscale characterization effort are put in place to achieve this goal. The key findings from this study are summarized as follows:

1. Irrespective of the LPBF processing conditions the improved GFA of the investigated alloy facilitated the manufacturing of dense samples with very high amorphous fractions. In particular, density values exceeding 90 % and AM % higher than 88 % were obtained in all cases.

2. The minimum coercive field achieved within the processing conditions investigated, 44 A/m, is lower than the levels reported for additively manufactured commercial Fe-based metallic glasses by at least an order of magnitude and it is also lower than those reported on any AM-processed as-built crystalline soft magnetic material.

3. Nanoindentation tests revealed that remelting strategies are beneficial to reduce the local scatter in the hardness and Young's modulus distributions, and this is attributed to an homogeneization of the internal stress fields.

4. At such high amorphous fraction levels (AM % > 88 %), the variation of the coercivity cannot be directly correlated with the concentration of crystalline phases. Instead, H_c might be more influenced by the internal porosity. The effect of other factors, such as the

local distribution of internal stresses and the magnetoelastic anisotropy, which have not been accounted for in the present study, can also not be neglected.

8. CONCLUSIONS

This thesis investigated the process–structure–property relationships governing the laser powder bed fusion of two Fe-based glass-forming alloys, Kuamet 6B2 and Fe-Si-B-Nb-Ni, with the aim of identifying processing conditions capable of fabricating large components with the soft magnetic properties sought after in energy-conversion applications such as electric motors, generators and transformers. By combining experimental process optimization, multiscale microstructural characterization, magnetic and mechanical testing, and finite-element simulations, this work provides new insight into the mechanisms underlying defect formation and devitrification, and clarifies how these features affect to mechanical and magnetic performance. Collectively, the results underscore both the potential and the persistent challenges associated with processing Fe-based metallic glasses manufactured by LPBF.

LPBF processing of Kuamet 6B2, a commercial alloy with limited glass-forming ability, revealed a narrow processabiliy window. The material showed a persistent tendency toward lack of fusion porosity, both internal and external cracking, and severe devitrification in the heat affected zones. The relative part density and amorphous fraction were strongly but inversely influenced by the scanning speed. Thermal accumulation was found to be a critical limitation: the absence of sufficient cooling time between successive tracks or layers promoted devitrification. Finite-element simulations provided a mechanistic context for the experimental observations by quantifying thermal gradients under different processing conditions. The simulations established that the HAZs are highly susceptible to devitrification, especially in the overlapping regions of neighboring tracks due to excessive heat accumulation. Introducing time delays after each scan track effectively mitigated this issue by prolonging cooling periods and reducing the incubation times at high temperatures, thereby reducing crystallization and localizing HAZs. These findings indicate that thermal management is a decisive factor in controlling microstructural stability during LPBF of Fe-based metallic glasses.

A considerably different response was observed for Fe-Si-B-Nb-Ni, a newly designed composition with higher glass-forming ability. The evaluation of this alloy's LPBF trials revealed substantially lower crystallization, reaching full amorphicity in several cases. Lower porosity levels were observed across a broader parameter space, while internal cracks persisted. In this

alloy, high energy input combinations yielded high relative density and a mainly amorphous structure. The results from Fe-Si-B-Nb-Ni illustrate that, provided sufficient intrinsic GFA, conduction-mode LPBF can indeed preserve amorphous structure to a significant extent when thermal accumulation is adequately controlled.

Mechanical characterization across multiple length scales highlighted the dominant influence of defects on the strength and on the stiffness of the LPBF-processed Kuamet 6B2. Micromechanical testing of individual phases showed that the crystalline constituents exhibited higher elastic moduli and hardness relative to the amorphous matrix, consistent with their more ordered atomic structure. However, these intrinsic differences were overshadowed at the macroscale by process-induced defects. Porosity, crack density, and their orientation relative to the build direction governed performance under uniaxial compression. Specimens aligned such that cracks or elongated pores intersected the loading axis failed at substantially lower stresses, underscoring the structural consequences of non-uniform thermal gradients during fabrication. These results collectively show that mechanical performance in LPBF-processed metallic glasses is controlled less by their intrinsic (micro)structural properties and more by the heterogeneous defect structure generated during processing.

The magnetic properties exhibited a strong sensitivity to microstructural features in Kuamet 6B2 parts. Magnetic coercivity showed a clear inverse correlation with the amorphous fraction, when the later was in the range of 0-70 %. This reflecting the role of structural disorder and the suppression of diamagnetic crystalline phases like borides in enabling efficient domain wall motion. The saturation magnetization, by contrast, was comparatively robust to processing variations and changed only moderately with crystallization, indicating that M_s is less sensitive than H_c to local structural heterogeneity and rather related to the Fe content of the part. Fe-Si-B-Nb-Ni again outperformed Kuamet 6B2, reaching coercivity values two orders of magnitude lower, while maintaining a high saturation magnetization across a wide processing range. Having eliminated the formation of boride phases in Fe-Si-B-Nb-Ni samples, internal porosity was shown to hinder soft magnetic properties. These results, achieved through alloy design and processing strategy selection, allow to address additional factors such as residual stresses or magneto-elasticity, to further enhance the soft magnetic properties.

In summary, this thesis combined multi-scale experimental investigation with numerical simulations to expand the community's understanding of the intricate phenomena involved in

LPBF processing of Fe-based metallic glasses. The Kuamet 6B2 work provides a deeper understanding on the effect of the most relevant processing parameters on the internal defects, (micro)structure and properties, putting forward thermal management tools to suppress devitrification, though some limitations persist. When such findings and methodology were applied to the processing of an alloy with sufficiently high GFA, such as Fe-Si-B-Nb-Ni, unprecedented combinations of fully amorphous content, high relative density, low coercivity and high magnetic saturation were achieved. Ultimately, this work aims to offer practical guidelines to enable the adoption of soft magnetic amorphous metals in the energy and transportation sectors, where they can be used to reduce energy losses of electrical machines, contributing towards a sustainable technological development. Beyond the specific alloys examined here, it is our contention that the approaches developed in this work might be applicable to the additive manufacturing of a wide range of glass-forming alloys.

9. FUTURE WORK

The findings presented in this work have contributed towards filling several gaps in the literature, providing necessary knowledge for integration of additively soft magnetic manufactured metallic glass parts in commercial components. However, several key topics in this field remain underexplored and must be further investigated.

9.1. Mitigation of internal cracks

Regardless of the processing parameter combination or scanning strategy selected on all the alloys studied in this thesis, internal cracking was not observed to degrease significantly. In Chapter 5, compression tests revealed that internal defects such as voids and cracks dominated and severely hindered the mechanical response of the material. It is therefore essential to control or mitigate the generation of internal cracks by gaining a deep understanding of their origin and propagation. Residual stress measurements can give valuable insight in this regard. Moreover, the multi-scale combination of characterization methods presented in this work can be used to locally study the (micro)structure around internal cracks. Approaches like pre-heating of the build substrate, beam shaping or dual-laser scanning have been used on other alloys to prevent cracking. Typically, these approaches are typically avoided when working with metallic glasses, as they reduce the cooling rates achieved in the manufacturing process. However, with new compositions with a higher GFA, better thermal stability and therefore a wider supercooled liquid region, may enable the manufacturing of samples with close to 100 % amorphous fractions and reduced internal cracking.

9.2. Further reduction of magnetic coercivity

This work has shown how the newly designed Fe-Si-B-Nb-Ni composition, in combination with the most favorable processing parameters and scanning strategy significantly enhanced the soft magnetic behavior of LPBF-processed parts, in comparison to the performance of the commercial alloy. Nevertheless, the magnetic coercivity remained one order of magnitude higher than that of the fully amorphous melt-spun ribbons. It is evident, based on the findings presented

in Chapter 7, that the residual coercivity is affected by factors beyond the (micro)structure, which must be better understood. Stress-relief heat treatments below the crystallization temperature can be performed on LPBF-manufactured samples to relieve stresses and magnetoelastic anisotropy. Finding the combination of heat treatment conditions leading to optimum soft magnetic behavior in new alloys like the Fe-Si-B-Nb-Ni system used in Chapter 7 requires a thorough understanding of the time-temperature-dependent properties of the specific alloy, which is currently missing.

9.3. Fabrication of complex geometries

Finally, the entirety of the samples fabricated in this doctoral thesis had simple cubic geometries. It is well known in the metal additive manufacturing community that parameter optimization becomes non-trivial for geometries of increased complexity. Additional studies should be carried out by gradually increasing the complexity from cubes to thin walls, tilted surfaces, thin rods or components which are bulky in the top and narrow at the base. The challenge here is the uneven thermal distribution caused by variable scan track lengths and re-scan times. In order to control this, advanced scanning strategies must be developed to locally manage the heat accumulation and avoid devitrification in the regions with poor heat dissipation. This thesis has demonstrated how the use of time delays and re-scan strategies can be used to mitigate devitrification in simple geometries, and can serve as a starting point for further studies on complex geometries.

BIBLIOGRAPHY

[1] W. E. Frazier, "Metal additive manufacturing: A review," *Journal of Materials Engineering and performance*, vol. 23, pp. 1917–1928, 2014. DOI: 10.1007/s11665-014-0958-z.

[2] F. Kerstens, A. Cervone, and P. Gradl, "End to end process evaluation for additively manufactured liquid rocket engine thrust chambers," *Acta Astronautica*, vol. 182, Mar. 2021. DOI: 10.1016/j.actaastro.2021.02.034.

[3] T. DebRoy, H. Wei, J. Zuback, T. Mukherjee, J. Elmer, J. Milewski, A. M. Beese, A. d. Wilson-Heid, A. De, and W. Zhang, "Additive manufacturing of metallic components–process, structure and properties," *Progress in Materials Science*, vol. 92, pp. 112–224, 2018. DOI: 10.1016/j.pmatsci.2017.10.001.

[4] M. A. Buhairi, F. M. Foudzi, F. I. Jamhari, A. B. Sulong, N. A. M. Radzuan, N. Muhamad, I. F. Mohamed, A. H. Azman, W. S. W. Harun, and M. S. Al-Furjan, "Review on volumetric energy density: Influence on morphology and mechanical properties of ti6al4v manufactured via laser powder bed fusion," *Progress in Additive Manufacturing 2022 8:2*, vol. 8, pp. 265–283, 2 Jul. 2022. DOI: 10.1007/S40964-022-00328-0.

[5] M. Thomas, G. J. Baxter, and I. Todd, "Normalised model-based processing diagrams for additive layer manufacture of engineering alloys," *Acta Materialia*, vol. 108, 2016. DOI: 10.1016/j.actamat.2016.02.025.

[6] H. Ghasemi-Tabasi, J. Jhabvala, E. Boillat, T. Ivas, R. Drissi-Daoudi, and R. E. Logé, "An effective rule for translating optimal selective laser melting processing parameters from one material to another," *Additive Manufacturing*, vol. 36, 2020. DOI: 10.1016/j.addma.2020.101496.

[7] M. A. L. Phan, O. Dew, and I. Todd, "Predictive process diagram for parameters selection in laser powder bed fusion to achieve high-density and low-cracking built parts," *Additive Manufacturing*, vol. 85, p. 104 145, Apr. 2024. DOI: 10.1016/J.ADDMA.2024.104145.

[8] D. B. Hann, J. Iammi, and J. Folkes, "A simple methodology for predicting laser-weld properties from material and laser parameters," *Journal of Physics D: Applied Physics*, vol. 44, p. 445 401, 44 Oct. 2011. DOI: 10.1088/0022-3727/44/44/445401.

[9] A. Mostafaei *et al.*, "Defects and anomalies in powder bed fusion metal additive manufacturing," *Current Opinion in Solid State and Materials Science*, vol. 26, 2 2022. DOI: 10.1016/j.cossms.2021.100974.

[10] S. Bag, A. Trivedi, and A. De, "Development of a finite element based heat transfer model for conduction mode laser spot welding process using an adaptive volumetric heat source," *International Journal of Thermal Sciences*, vol. 48, pp. 1923–1931, 10 Oct. 2009. DOI: 10.1016/J.IJTHERMALSCI.2009.02.010.

[11] J. Yang, L. M. Schlenger, M. H. Nasab, S. V. Petegem, F. Marone, R. E. Logé, and C. Leinenbach, "Experimental quantification of inward marangoni convection and its impact on keyhole threshold in laser powder bed fusion of stainless steel," *Additive Manufacturing*, vol. 84, Mar. 2024. DOI: 10.1016/j.addma.2024.104092.

[12] W. E. King, H. D. Barth, V. M. Castillo, G. F. Gallegos, J. W. Gibbs, D. E. Hahn, C. Kamath, and A. M. Rubenchik, "Observation of keyhole-mode laser melting in laser powder-bed fusion additive manufacturing," *Journal of Materials Processing Technology*, vol. 214, pp. 2915–2925, 12 Dec. 2014. DOI: 10.1016/J.JMATPROTEC.2014.06.005.

[13] P. Promoppatum and S. C. Yao, "Analytical evaluation of defect generation for selective laser melting of metals," *The International Journal of Advanced Manufacturing Technology 2019 103:1*, vol. 103, pp. 1185–1198, 1 Apr. 2019. DOI: 10.1007/S00170-019-03500-Z.

[14] R. Snell, S. Tammas-Williams, L. Chechik, A. Lyle, E. Hernández-Nava, C. Boig, G. Panoutsos, and I. Todd, "Methods for rapid pore classification in metal additive manufacturing," *JOM 2019 72:1*, vol. 72, pp. 101–109, 1 Sep. 2019. DOI: 10.1007/S11837-019-03761-9.

[15] S. Shrestha and K. Chou, "Formation of keyhole and lack of fusion pores during the laser powder bed fusion process," *Manufacturing Letters*, vol. 32, pp. 19–23, Apr. 2022. DOI: 10.1016/J.MFGLET.2022.01.005.

[16] C. Böhm, M. Werz, and S. Weihe, "Practical approach to eliminate solidification cracks by supplementing almg4.5mn0.7 with alsi10mg powder in laser powder bed fusion," *Materials 2022, Vol. 15, Page 572*, vol. 15, p. 572, 2 Jan. 2022. DOI: 10.3390/MA15020572.

[17] K. Kempen, L. Thijs, B. Vrancken, S. Buls, J. V. Humbeeck, and J.-P. Kruth, "Producing crack-free, high density m2 hss parts by selective laser melting: Pre-heating the baseplate," *University of Texas at Austin*, Aug. 2013. DOI: 10.26153/TSW/15419.

[18] W. Stopyra, K. Gruber, I. Smolina, T. Kurzynowski, and B. Kuźnicka, "Laser powder bed fusion of aa7075 alloy: Influence of process parameters on porosity and hot cracking," *Additive Manufacturing*, vol. 35, p. 101 270, Oct. 2020. DOI: 10.1016/J.ADDMA.2020.101270.

[19] P. Yu, S. Kou, and C. M. Lin, "Solidification and liquation cracking in welds of high entropy cocrfenicux alloys," *Materials 2023, Vol. 16, Page 5621*, vol. 16, p. 5621, 16 Aug. 2023. DOI: 10.3390/MA16165621.

[20] H. Jia, H. Sun, H. Wang, Y. Wu, and H. Wang, "Scanning strategy in selective laser melting (slm): A review," *The International Journal of Advanced Manufacturing Technology 2021 113:9*, vol. 113, pp. 2413–2435, 9 Feb. 2021. DOI: 10.1007/S00170-021-06810-3.

[21] J. Schröder, T. Fritsch, V. Luzin, B. Ferrari, J. Simón-Muzás, A. Evans, and G. Bruno, "Impact of scan strategy on principal stresses in laser powder bed fusion," *Materials & Design*, vol. 244, p. 113 171, Aug. 2024. DOI: 10.1016/J.MATDES.2024.113171.

[22] S. Chowdhury, N. Yadaiah, C. Prakash, S. Ramakrishna, S. Dixit, L. R. Gupta, and D. Buddhi, "Laser powder bed fusion: A state-of-the-art review of the technology, materials, properties & defects, and numerical modelling," *Journal of Materials Research and Technology*, vol. 20, pp. 2109–2172, Sep. 2022. DOI: 10.1016/J.JMRT.2022.07.121.

[23] W. H. Wang, C. Dong, and C. H. Shek, "Bulk metallic glasses," *Materials Science and Engineering: R: Reports*, vol. 44, pp. 45–89, 2-3 Jun. 2004. DOI: 10.1016/J.MSER.2004.03.001.

[24] Q. Halim, N. A. N. Mohamed, M. R. M. Rejab, W. N. W. A. Naim, and Q. Ma, "Metallic glass properties, processing method and development perspective: A review," *The International Journal of Advanced Manufacturing Technology*, vol. 112, pp. 1231–1258, 2021. DOI: 10.1007/s00170-020-06515-z.

[25] J. R. Scully, A. Gebert, and J. H. Payer, "Corrosion and related mechanical properties of bulk metallic glasses," *Journal of Materials Research*, vol. 22, pp. 302–313, 2 Feb. 2007. DOI: 10.1557/JMR.2007.0051.

[26] M. F. Ashby and A. L. Greer, "Metallic glasses as structural materials," *Scripta Materialia*, vol. 54, pp. 321–326, 3 Feb. 2006. DOI: 10.1016/J.SCRIPTAMAT.2005.09.051.

[27] C. A. Schuh, T. C. Hufnagel, and U. Ramamurty, "Mechanical behavior of amorphous alloys," *Acta Materialia*, vol. 55, pp. 4067–4109, 12 Jul. 2007. DOI: 10.1016/J.ACTAMAT.2007.01.052.

[28] Z. Zhang, J. Eckert, and L. Schultz, "Difference in compressive and tensile fracture mechanisms of zr59cu20al10ni8ti3 bulk metallic glass," *Acta Materialia*, vol. 51, no. 4, pp. 1167–1179, 2003. DOI: 10.1016/S1359-6454(02)00521-9.

[29] Z.-Q. Song, Q. He, E. Ma, and J. Xu, "Fatigue endurance limit and crack growth behavior of a high-toughness zr61ti2cu25al12 bulk metallic glass," *Acta Materialia*, vol. 99, pp. 165–175, 2015. DOI: 10.1016/j.actamat.2015.07.071.

[30] A. Inoue and J. S. Gook, "Fe-based ferromagnetic glassy alloys with wide supercooled liquid region," *Materials Transactions, JIM*, vol. 36, no. 9, pp. 1180–1183, 1995. DOI: 10.2320/matertrans1989.36.1180.

[31] H. X. Li, Z. C. Lu, S. L. Wang, Y. Wu, and Z. P. Lu, "Fe-based bulk metallic glasses: Glass formation, fabrication, properties and applications," *Progress in Materials Science*, vol. 103, pp. 235–318, Jun. 2019. DOI: 10.1016/j.pmatsci.2019.01.003.

[32] I. Gallino and R. Busch, *Physical Metallurgy of Bulk Metallic Glass-Forming Liquids. Thermodynamic and Kinetic Concepts in Glass Formation*, 341st ed. Springer Series in Materials Science, 2024, vol. 341. DOI: 10.1007/978-3-031-71536-5.

[33] S. K. Patel, B. K. Swain, A. Behera, S. S. Mohapatra, S. K. Patel, B. K. Swain, A. Behera, and S. S. Mohapatra, "Metallic glasses: A revolution in material science," *Metallic Glasses*, Jan. 2020. DOI: 10.5772/INTECHOPEN.90165.

[34] A. L. Greer, "Crystallization of metallic glasses," *Materials Science and Engineering: A*, vol. 179-180, pp. 41–45, PART 1 May 1994. DOI: 10.1016/0921-5093(94)90161-9.

[35] E. Pekarskaya, J. F. Löffler, and W. L. Johnson, "Microstructural studies of crystallization of a zr-based bulk metallic glass," *Acta Materialia*, vol. 51, pp. 4045–4057, 14 Aug. 2003. DOI: 10.1016/S1359-6454(03)00225-8.

[36] W. Klement, R. Willens, and P. Duwez, "Non-crystalline structure in solidified gold–silicon alloys," *Nature*, vol. 187, no. 4740, pp. 869–870, 1960. DOI: 10.1038/187869b0.

[37] C. Suryanarayana and A. Inoue, "Iron-based bulk metallic glasses," *International Materials Reviews*, vol. 58, no. 3, pp. 131–166, 2013. DOI: 10.1179/1743280412Y.0000000007.

[38] D. Turnbull, "Under what conditions can a glass be formed?" *Contemporary Physics*, vol. 10, pp. 473–488, 5 Sep. 1969. DOI: 10.1080/00107516908204405.

[39] J. Kinder, "Processing of metals and alloys – materials science and technology – vol. 15. hrsg. von r. w. cahn, p. haasen und e.-j. kramer, 628 seiten vch verlagsgesellschaft mbh, weinheim, new york, basel, cambridge 1991, dm 450,00, isbn 3-527-26828-6," *Materials and Corrosion*, vol. 47, no. 7, pp. 402–403, 1996. DOI: 10.1002/maco.19960470714.

[40] R. Madugundo, N. V. R. Rao, A. M. Schönhöbel, D. Salazar, and A. A. El-Gendy, "Recent developments in nanostructured permanent magnet materials and their processing methods," *Magnetic Nanostructured Materials: From Lab to Fab*, pp. 157–198, Jan. 2018. DOI: 10.1016/B978-0-12-813904-2.00006-1.

[41] J. G. Kaufman and E. L. Rooy, "Aluminum alloy castings : Properties, processes, and applications," p. 340, 2004.

[42] P. Pawlik and H. A. Davies, "The bulk glass forming abilities and mechanical and magnetic properties of fe–co–zr–mo–w–b alloys," *Journal of Non-Crystalline Solids*, vol. 329, pp. 17–21, 1-3 Nov. 2003. DOI: 10.1016/J.JNONCRYSOL.2003.08.005.

[43] A. Inoue and T. Zhang, "Fabrication of bulk glassy zr55al10ni5cu30 alloy of 30 mm in diameter by a suction casting method," *Materials Transactions, JIM*, vol. 37, pp. 185–187, 2 1996. DOI: 10.2320/MATERTRANS1989.37.185.

[44] T. Kozieł, K. Pajor, and Ł. Gondek, "Cooling rate evaluation during solidification in the suction casting process," *Journal of Materials Research and Technology*, vol. 9, pp. 13 502–13 508, 6 Nov. 2020. DOI: 10.1016/J.JMRT.2020.09.082.

[45] T. Kozieł, "Estimation of cooling rates in suction casting and copper-mould casting processes," *Archives of Metallurgy and Materials*, vol. 60, no. 2A, pp. 767–771, 2015.

[46] I. Figueroa, P. Carroll, H. Davies, H. Jones, and I. Todd, "Preparation of cu-based bulk metallic glasses by suction casting," p. 738, 2007. DOI: https://eprints.whiterose.ac.uk/id/oai_id/oai:eprints.whiterose.ac.uk:2641.

[47] H. S. Chen, "Thermodynamic considerations on the formation and stability of metallic glasses," *Acta Metallurgica*, vol. 22, pp. 1505–1511, 12 Dec. 1974. DOI: 10.1016/0001-6160(74)90112-6.

[48] N. Nishiyama, K. Takenaka, H. Miura, N. Saidoh, Y. Zeng, and A. Inoue, "The world's biggest glassy alloy ever made," *Intermetallics*, vol. 30, pp. 19–24, 2012, Bulk Metallic Glasse VIII. DOI: 10.1016/j.intermet.2012.03.020.

[49] N. Sohrabi, J. Jhabvala, and R. E. Logé, "Additive manufacturing of bulk metallic glasses—process, challenges and properties: A review," *Metals*, vol. 11, no. 8, p. 1279, 2021. DOI: 10.3390/met11081279.

[50] C. Zhang, D. Ouyang, S. Pauly, and L. Liu, "3d printing of bulk metallic glasses," *Materials Science and Engineering R: Reports*, vol. 145, Jul. 2021. DOI: 10.1016/j.mser.2021.100625.

[51] P. Zhang, J. Tan, Y. Tian, H. Yan, and Z. Yu, "Research progress on selective laser melting (slm) of bulk metallic glasses (bmgs): A review," *The International Journal of Advanced Manufacturing Technology*, pp. 2017–2057, 2021. DOI: 10.1007/s00170-021-07990-8/Published.

[52] H. Liu, Q. Jiang, J. Huo, Y. Zhang, W. Yang, and X. Li, "Crystallization in additive manufacturing of metallic glasses: A review," *Additive Manufacturing*, vol. 36, p. 101 568, 2020. DOI: 10.1016/j.addma.2020.101568.

[53] S. Pauly, L. L. Ber, R. Petters, M. Stoica, S. Scudino, U. K. Hn, and J. R. Eckert, "Processing metallic glasses by selective laser melting," *Materials Today*, vol. 16, pp. 37–41, 1-2 2013. DOI: 10.1016/j.mattod.2013.01.018.

[54] B. D. Cullity and C. D. Graham, *Introduction to magnetic materials*. IEEE/Wiley, 2009.

[55] G. Bertotti, *Hysteresis in Magnetism : For Physicists, Materials Scientists, and Engineers*. Academic press, 1998, p. 576.

[56] R. M. Bozorth, *Ferromagnetism*. IEEE Press, Aug. 1993, p. 968.

[57] M. E. McHenry, M. A. Willard, and D. E. Laughlin, "Amorphous and nanocrystalline materials for applications as soft magnets," *Progress in Materials Science*, vol. 44, pp. 291–433, 4 Oct. 1999. DOI: 10.1016/S0079-6425(99)00002-X.

[58] L. Han, F. Maccari, I. R. S. Filho, N. J. Peter, Y. Wei, B. Gault, O. Gutfleisch, Z. Li, and D. Raabe, "A mechanically strong and ductile soft magnet with extremely low coercivity," *Nature*, vol. 608, pp. 310–316, 7922 Aug. 2022. DOI: 10.1038/s41586-022-04935-3.

[59] R. Parekh, "Ac induction motor fundamentals," *Microchip Technology Inc*, no. DS00887A, pp. 1–24, 2003.

[60] G. E. Fish, "Soft magnetic materials," *Proceedings of the IEEE*, vol. 78, pp. 947–972, 6 1990. DOI: 10.1109/5.56909.

[61] F. Fiorillo, G. Bertotti, C. Appino, M. Pasquale, *et al.*, *Soft magnetic materials*. John Wiley & Sons, Inc., 2016, pp. 1–42.

[62] A. L. Greer, M. B. Costa, and O. S. Houghton, "Metallic glasses," *MRS Bulletin*, vol. 48, pp. 1054–1061, 10 Oct. 2023. DOI: 10.1557/S43577-023-00586-5/FIGURES/4.

[63] G. Bertotti, "Physical interpretation of eddy current losses in ferromagnetic materials. i. theoretical considerations," *Journal of Applied Physics*, vol. 57, pp. 2110–2117, 6 Mar. 1985. DOI: 10.1063/1.334404.

[64] M. A. Willard, M. Daniil, and K. E. Kniping, "Nanocrystalline soft magnetic materials at high temperatures: A perspective," *Scripta Materialia*, vol. 67, pp. 554–559, 6 Sep. 2012. DOI: 10.1016/J.SCRIPTAMAT.2011.12.043.

[65] P. Tiberto, M. Baricco, E. Olivetti, and R. Piccin, "Magnetic properties of bulk metallic glasses," *Advanced Engineering Materials*, vol. 9, no. 6, pp. 468–474, 2007. DOI: 10.1002/adem.200700050.

[66] J. M. Silveyra, E. Ferrara, D. L. Huber, and T. C. Monson, "Soft magnetic materials for a sustainable and electrified world," *Science*, vol. 362, no. 6413, eaao0195, 2018. DOI: 10.1126/science.aao0195.

[67] G. Herzer, "Modern soft magnets: Amorphous and nanocrystalline materials," *Acta Materialia*, vol. 61, no. 3, pp. 718–734, 2013, The Diamond Jubilee Issue. DOI: 10.1016/j.actamat.2012.10.040.

[68] A. Makino, C. Chang, T. Kubota, and A. Inoue, "Soft magnetic fe–si–b–p–c bulk metallic glasses without any glass-forming metal elements," *Journal of Alloys and Compounds*, vol. 483, pp. 616–619, 1-2 Aug. 2009. DOI: 10.1016/J.JALLCOM.2008.08.089.

[69] C. Chang, T. Kubota, A. Makino, and A. Inoue, "Synthesis of ferromagnetic fe-based bulk glassy alloys in the fe–si–b–p–c system," *Journal of Alloys and Compounds*, vol. 473, pp. 368–372, 1-2 Apr. 2009. DOI: 10.1016/J.JALLCOM.2008.05.088.

[70] Z. B. Jiao, H. X. Li, J. E. Gao, Y. Wu, and Z. P. Lu, "Effects of alloying elements on glass formation, mechanical and soft-magnetic properties of fe-based metallic glasses," *Intermetallics*, vol. 19, pp. 1502–1508, 10 Oct. 2011. DOI: 10.1016/J.INTERMET.2011.05.020.

[71] F. Liu, Q. Yang, S. Pang, C. Ma, and T. Zhang, "Ductile fe-based bmgs with high glass forming ability and high strength," *Materials Transactions*, vol. 49, pp. 231–234, 2 Feb. 2008. DOI: 10.2320/MATERTRANS.MRA2007186.

[72] B. Shen, C. Chang, Z. Zhang, and A. Inoue, "Enhancement of glass-forming ability of feconibsinb bulk glassy alloys with superhigh strength and good soft-magnetic properties," *Journal of Applied Physics*, vol. 102, 2 Jul. 2007. DOI: 10.1063/1.2757013/380175.

[73] K. Amiya and A. Inoue, "Fe-(cr,mo)-(c,b)-tm bulk metallic glasses with high strength and high glass-forming ability," *Materials Transactions*, vol. 47, pp. 1615–1618, 6 Jun. 2006. DOI: 10.2320/MATERTRANS.47.1615.

[74] A. Inoue, F. L. Kong, Q. K. Man, B. L. Shen, R. W. Li, and F. Al-Marzouki, "Development and applications of fe- and co-based bulk glassy alloys and their prospects," *Journal of Alloys and Compounds*, vol. 615, S2–S8, S1 Jan. 2015. DOI: 10.1016/J.JALLCOM.2013.11.122.

[75] Y. Zou, Z. Qiu, Z. Zheng, G. Wang, X. Yan, S. Yin, M. Liu, and D. Zeng, "Ex-situ additively manufactured fecrmocb/cu bulk metallic glass composite with well wear re-

sistance," *Tribology International*, vol. 162, p. 107 112, Oct. 2021. DOI: 10.1016/J.TRIBOINT.2021.107112.

[76] S. Gao, X. Yan, C. Chang, E. Aubry, P. He, M. Liu, H. Liao, and N. Fenineche, "Microstructure and magnetic properties of fesibcrc soft magnetic alloy manufactured by selective laser melting," *Materials Letters*, vol. 290, p. 129 469, May 2021. DOI: 10.1016/J.MATLET.2021.129469.

[77] Q. Jiang, P. Zhang, J. Tan, Z. Yu, Y. Tian, S. Ma, and D. Wu, "Influence of the microstructure on mechanical properties of slm additive manufacturing fe-based bulk metallic glasses," *Journal of Alloys and Compounds*, vol. 894, p. 162 525, Feb. 2022. DOI: 10.1016/J.JALLCOM.2021.162525.

[78] L. Thorsson, M. Unosson, M. T. Pérez-Prado, X. Jin, P. Tiberto, G. Barrera, B. Adam, N. Neuber, A. Ghavimi, M. Frey, R. Busch, and I. Gallino, "Selective laser melting of a fe-si-cr-b-c-based complex-shaped amorphous soft-magnetic electric motor rotor with record dimensions," *Materials & Design*, vol. 215, p. 110 483, Mar. 2022. DOI: 10.1016/J.MATDES.2022.110483.

[79] N. Luo, C. Scheitler, N. Ciftci, F. Galgon, Z. Fu, V. Uhlenwinkel, M. Schmidt, and C. Körner, "Preparation of fe-co-b-si-nb bulk metallic glasses by laser powder bed fusion: Microstructure and properties," *Materials Characterization*, vol. 162, p. 110 206, Apr. 2020. DOI: 10.1016/J.MATCHAR.2020.110206.

[80] F. Xie, Q. Chen, and J. Gao, "Brittle-ductile transition in laser 3d printing of fe-based bulk metallic glass composites," *Metals 2019*, vol. 9, p. 78, 1 Jan. 2019. DOI: 10.3390/MET9010078.

[81] N. Li, J. Zhang, W. Xing, D. Ouyang, and L. Liu, "3d printing of fe-based bulk metallic glass composites with combined high strength and fracture toughness," *Materials & Design*, vol. 143, pp. 285–296, Apr. 2018. DOI: 10.1016/J.MATDES.2018.01.061.

[82] D. Ouyang, W. Xing, N. Li, Y. Li, and L. Liu, "Structural evolutions in 3d-printed fe-based metallic glass fabricated by selective laser melting," *Additive Manufacturing*, vol. 23, pp. 246–252, 2018. DOI: 10.1016/j.addma.2018.08.020.

[83] Z. Mahbooba, L. Thorsson, M. Unosson, P. Skoglund, H. West, T. Horn, C. Rock, E. Vogli, and O. Harrysson, "Additive manufacturing of an iron-based bulk metallic glass

larger than the critical casting thickness," *Applied Materials Today*, vol. 11, pp. 264–269, Jun. 2018. DOI: 10.1016/J.APMT.2018.02.011.

[84] H. Y. Jung, S. J. Choi, K. G. Prashanth, M. Stoica, S. Scudino, S. Yi, U. Kühn, D. H. Kim, K. B. Kim, and J. Eckert, "Fabrication of fe-based bulk metallic glass by selective laser melting: A parameter study," *Materials & Design*, vol. 86, pp. 703–708, Dec. 2015. DOI: 10.1016/J.MATDES.2015.07.145.

[85] Y. G. Nam, B. Koo, M. S. Chang, S. Yang, J. Yu, Y. H. Park, and J. W. Jeong, "Selective laser melting vitrification of amorphous soft magnetic alloys with help of double-scanning-induced compositional homogeneity," *Materials Letters*, vol. 261, p. 127 068, Feb. 2020. DOI: 10.1016/J.MATLET.2019.127068.

[86] M. G. 0zden, F. S. Freeman, and N. A. Morley, "Soft-magnetic behavior of fe-based nanocrystalline alloys produced using laser powder bed fusion," *Advanced Engineering Materials*, vol. 25, p. 2 300 597, 19 Oct. 2023. DOI: 10.1002/ADEM.202300597.

[87] M. G. Özden and N. A. Morley, "Optimizing laser additive manufacturing process for fe-based nano-crystalline magnetic materials," *Journal of Alloys and Compounds*, vol. 960, p. 170 644, Oct. 2023. DOI: 10.1016/J.JALLCOM.2023.170644.

[88] Ł. Żrodowski, B. Wysocki, R. Wróblewski, K. J. Kurzydłowski, and W. Święszkowski, "The novel scanning strategy for fabrication metallic glasses by selective laser melting," in *Fraunhofer Direct Digital Manufacturing Conference (DDMC 2016)*, 2016.

[89] Ł. Żrodowski, B. Wysocki, R. Wróblewski, A. Krawczyńska, B. Adamczyk-Cieślak, J. Zdunek, P. Błyskun, J. Ferenc, M. Leonowicz, and W. Święszkowski, "New approach to amorphization of alloys with low glass forming ability via selective laser melting," *Journal of Alloys and Compounds*, vol. 771, pp. 769–776, Jan. 2019. DOI: 10.1016/J.JALLCOM.2018.08.075.

[90] S. Sadanand, M. Rodríguez-Sánchez, A. Ghavimi, R. Busch, P. Sharangi, P. M. Tiberto, E. Ferrara, G. Barrera, L. Thorsson, H. J. Wachter, I. Gallino, M. T. Pérez-Prado, and J. A. Phys, "Laser powder bed fusion of a nanocrystalline finemet fe-based alloy for soft magnetic applications," *Journal of Laser Applications*, vol. 36, p. 42 029, 4 Nov. 2024. DOI: 10.2351/7.0001391.

[91] S. X. Liang, X. Wang, W. Zhang, Y. J. Liu, W. Wang, and L. C. Zhang, "Selective laser melting manufactured porous fe-based metallic glass matrix composite with remarkable catalytic activity and reusability," *Applied Materials Today*, vol. 19, p. 100 543, Jun. 2020. DOI: 10.1016/J.APMT.2019.100543.

[92] Y. M. Zou, Y. S. Wu, K. F. Li, C. L. Tan, Z. G. Qiu, and D. C. Zeng, "Selective laser melting of crack-free fe-based bulk metallic glass via chessboard scanning strategy," *Materials Letters*, vol. 272, p. 127 824, Aug. 2020. DOI: 10.1016/J.MATLET.2020.127824.

[93] X. D. Nong, X. L. Zhou, and Y. X. Ren, "Fabrication and characterization of fe-based metallic glasses by selective laser melting," *Optics & Laser Technology*, vol. 109, pp. 20–26, Jan. 2019. DOI: 10.1016/J.OPTLASTEC.2018.07.059.

[94] A. Małachowska, Żrodowski, B. Morończyk, Maj, A. Kuś, and T. Lampke, "Selective laser melting of fe-based metallic glasses with different degree of plasticity," *Metallurgical and Materials Transactions A: Physical Metallurgy and Materials Science*, vol. 54, pp. 658–670, 2 Feb. 2023. DOI: 10.1007/s11661-022-06913-w.

[95] W. Xing, D. Ouyang, N. Li, and L. Liu, "Insight into micro-cracking in 3d-printed fe-based bmgs by selective laser melting," *Intermetallics*, vol. 103, pp. 101–106, Dec. 2018. DOI: 10.1016/J.INTERMET.2018.10.011.

[96] F. Xie, Q. Chen, J. Gao, and Y. Li, "Laser 3d printing of fe-based bulk metallic glass: Microstructure evolution and crack propagation," *Journal of Materials Engineering and Performance*, vol. 28, pp. 3478–3486, 6 Jun. 2019. DOI: 10.1007/S11665-019-04103-1/METRICS.

[97] L. Wang, H. Wang, Y. Liu, Z. Fu, T. Peng, J. Shen, S. Zhou, M. Yan, G. Wang, and Y. Dai, "Selective laser melting helps fabricate record-large bulk metallic glass: Experiments, simulation and demonstrative part," *Journal of Alloys and Compounds*, vol. 808, p. 151 731, Nov. 2019. DOI: 10.1016/J.JALLCOM.2019.151731.

[98] I. Otsuka, K. Wada, Y. Maeta, T. Kadomura, and M. Yagi, "Magnetic properties of fe-based amorphous powders with high-saturation induction produced by spinning water atomization process (swap)," *IEEE Transactions on Magnetics*, vol. 44, pp. 3891–3894, 11 PART 2 2008. DOI: 10.1109/TMAG.2008.2002249.

[99] A. International, "Standard test methods for flow rate of metal powders using the hall flowmeter funnel," *ASTM Standard*, 2016.

[100] A. B527-20, "Astm b527-20 standard test method for tap density of metal powders and compounds," *ASTM International*, 2020.

[101] M. A. Kaleem, M. Z. Alam, M. Khan, S. H. I. Jaffery, and B. Rashid, "An experimental investigation on accuracy of hausner ratio and carr index of powders in additive manufacturing processes," *Metal Powder Report*, vol. 76, 2021. DOI: 10.1016/j.mprp.2020.06.061.

[102] I. Arganda-Carreras, V. Kaynig, C. Rueden, K. W. Eliceiri, J. Schindelin, A. Cardona, and H. S. Seung, "Trainable weka segmentation: A machine learning tool for microscopy pixel classification," *Bioinformatics*, vol. 33, 15 2017. DOI: 10.1093/bioinformatics/btx180.

[103] K. Thompson, D. Lawrence, D. J. Larson, J. D. Olson, T. F. Kelly, and B. Gorman, "In situ site-specific specimen preparation for atom probe tomography," *Ultramicroscopy*, vol. 107, pp. 131–139, 2-3 Feb. 2007. DOI: 10.1016/J.ULTRAMIC.2006.06.008.

[104] D. Tourret, R. Tavakoli, A. D. Boccardo, A. K. Boukellal, M. Li, and J. Molina-Aldareguia, "Emergence of rapid solidification microstructure in additive manufacturing of a magnesium alloy," *Modelling and Simulation in Materials Science and Engineering*, vol. 32, p. 055 012, 5 May 2024. DOI: 10.1088/1361-651X/AD4576.

[105] B. Cheng, S. Price, J. Lydon, K. Cooper, and K. Chou, "On process temperature in powder-bed electron beam additive manufacturing: Model development and validation," *Journal of Manufacturing Science and Engineering, Transactions of the ASME*, vol. 136, 6 Dec. 2014. DOI: 10.1115/1.4028484.

[106] M. Rodríguez-Sánchez, M. T. Pérez-Prado, A. D. Boccardo, and D. Tourret, "Laser-based additive manufacturing device and method for crystallization control of metallic glasses," EP24383248.2, Nov. 2025.

[107] E. A. Brandes and G. B. Brook, *Smithells Metals Reference Book: Seventh Edition*. Elsevier Inc., Oct. 2013, pp. 1–1800. DOI: 10.1016/C2009-0-25363-3.

[108] A. Załuska and H. Matyja, "Crystallization characteristics of amorphous fe-si-b alloys," *Journal of Materials Science*, vol. 18, 7 1983. DOI: 10.1007/BF00555011.

[109] D. S. D. Santos and D. R. D. Santos, "Crystallization kinetics of fe-b-si metallic glasses," in *Journal of Non-Crystalline Solids*, vol. 304, 2002. DOI: 10.1016/S0022-3093(02)01004-9.

[110] P. Gorria, I. Orue, F. Plazaola, M. L. Fernández-Gubieda, and J. M. Barandiarán, "Magnetic and mössbauer study of amorphous and nanocrystalline fe86zr7cu1b6 alloys," *IEEE Transactions on Magnetics*, vol. 29, pp. 2682–2684, 6 1993. DOI: 10.1109/20.280941.

[111] A. D. Goodall, L. Chechik, R. L. Mitchell, G. W. Jewell, and I. Todd, "Cracking of soft magnetic fesi to reduce eddy current losses in stator cores," *Additive Manufacturing*, vol. 70, 2023. DOI: 10.1016/j.addma.2023.103555.

[112] J. Wang, R. Zhu, Y. Liu, and L. Zhang, "Understanding melt pool characteristics in laser powder bed fusion: An overview of single-and multi-track melt pools for process optimization," *Advanced Powder Materials*, 2023. DOI: 10.1016/j.apmate.2023.100137.

[113] T. V. Eagar and N.-S. Tsai, "Temperature fields produced by traveling distributed heat sources," *Welding journal*, 1983.

[114] T. Qi, H. Zhu, H. Zhang, J. Yin, L. Ke, and X. Zeng, "Selective laser melting of al7050 powder: Melting mode transition and comparison of the characteristics between the keyhole and conduction mode," *Materials & Design*, vol. 135, pp. 257–266, Dec. 2017. DOI: 10.1016/J.MATDES.2017.09.014.

[115] M. Markl and C. Körner, "Multiscale modeling of powder bed–based additive manufacturing," *https://doi.org/10.1146/annurev-matsci-070115-032158*, vol. 46, pp. 93–123, Jul. 2016. DOI: 10.1146/ANNUREV-MATSCI-070115-032158.

[116] R. Cunningham, C. Zhao, N. Parab, C. Kantzos, J. Pauza, K. Fezzaa, T. Sun, and A. D. Rollett, "Keyhole threshold and morphology in laser melting revealed by ultrahigh-speed x-ray imaging," *Science*, vol. 363, pp. 849–852, 6429 2019. DOI: 10.1126/SCIENCE.AAV4687.

[117] R. Rai, J. W. Elmer, T. A. Palmer, and T. Debroy, "Heat transfer and fluid flow during keyhole mode laser welding of tantalum, ti–6al–4v, 304l stainless steel and vanadium," *Journal of Physics D: Applied Physics*, vol. 40, p. 5753, 18 Aug. 2007. DOI: 10.1088/0022-3727/40/18/037.

[118] R. Drissi-Daoudi, G. Masinelli, C. de Formanoir, K. Wasmer, J. Jhabvala, and R. E. Logé, "Acoustic emission for the prediction of processing regimes in laser powder bed fusion, and the generation of processing maps," *Additive Manufacturing*, vol. 67, p. 103 484, Apr. 2023. DOI: 10.1016/J.ADDMA.2023.103484.

[119] L. E. Criales, Y. M. Arısoy, B. Lane, S. Moylan, A. Donmez, and T. Özel, "Laser powder bed fusion of nickel alloy 625: Experimental investigations of effects of process parameters on melt pool size and shape with spatter analysis," *International Journal of Machine Tools and Manufacture*, vol. 121, pp. 22–36, Oct. 2017. DOI: 10.1016/J.IJMACHTOOLS.2017.03.004.

[120] M. Afrasiabi, D. Keller, C. Lüthi, M. Bambach, and K. Wegener, "Effect of process parameters on melt pool geometry in laser powder bed fusion of metals: A numerical investigation," *Procedia CIRP*, vol. 113, pp. 378–384, Jan. 2022. DOI: 10.1016/J.PROCIR.2022.09.187.

[121] Q. Guo, C. Zhao, M. Qu, L. Xiong, L. I. Escano, S. M. H. Hojjatzadeh, N. D. Parab, K. Fezzaa, W. Everhart, T. Sun, and L. Chen, "In-situ characterization and quantification of melt pool variation under constant input energy density in laser powder bed fusion additive manufacturing process," *Additive Manufacturing*, vol. 28, pp. 600–609, Aug. 2019. DOI: 10.1016/J.ADDMA.2019.04.021.

[122] P. Akbari, F. Ogoke, N. Y. Kao, K. Meidani, C. Y. Yeh, W. Lee, and A. B. Farimani, "Meltpoolnet: Melt pool characteristic prediction in metal additive manufacturing using machine learning," *Additive Manufacturing*, vol. 55, p. 102 817, Jul. 2022. DOI: 10.1016/J.ADDMA.2022.102817.

[123] J. J. Dilip, S. Zhang, C. Teng, K. Zeng, C. Robinson, D. Pal, and B. Stucker, "Influence of processing parameters on the evolution of melt pool, porosity, and microstructures in ti-6al-4v alloy parts fabricated by selective laser melting," *Progress in Additive Manufacturing*, vol. 2, pp. 157–167, 3 Sep. 2017. DOI: 10.1007/S40964-017-0030-2/FIGURES/11.

[124] A. Keshavarzkermani, E. Marzbanrad, R. Esmaeilizadeh, Y. Mahmoodkhani, U. Ali, P. D. Enrique, N. Y. Zhou, A. Bonakdar, and E. Toyserkani, "An investigation into the effect of process parameters on melt pool geometry, cell spacing, and grain refinement

during laser powder bed fusion," *Optics & Laser Technology*, vol. 116, pp. 83–91, Aug. 2019. DOI: 10.1016/J.OPTLASTEC.2019.03.012.

[125] J. Metelkova, Y. Kinds, K. Kempen, C. de Formanoir, A. Witvrouw, and B. V. Hooreweder, "On the influence of laser defocusing in selective laser melting of 316l," *Additive Manufacturing*, vol. 23, pp. 161–169, Oct. 2018. DOI: 10.1016/J.ADDMA.2018.08.006.

[126] S. Y. Ahn, S. G. Jeong, M. J. SaGong, G. Lee, E. S. Kim, H. Park, J. W. Cho, J. G. Kim, and H. S. Kim, "Size matters: Exploring part size effects on microstructure, defects, and mechanical property in optimized laser powder bed fusion (l-pbf) additive manufacturing," *Materials Science and Engineering: A*, vol. 902, p. 146 616, Jun. 2024. DOI: 10.1016/J.MSEA.2024.146616.

[127] I. Rodríguez-Barber, A. M. Fernández-Blanco, I. Unanue-Arruti, I. Madariaga-Rodríguez, S. Milenkovic, and M. T. Pérez-Prado, "Precontouring as a tool to improve the laser powder bed fusion printability of inconel939 thin walls," *Advanced Engineering Materials*, vol. 27, p. 2 401 929, 4 Feb. 2025. DOI: 10.1002/ADEM.202401929;PAGEGROUP:STRING:PUBLICATION.

[128] N. Sohrabi, T. Ivas, J. Jhabvala, J. E. Schawe, J. F. Löffler, H. Ghasemi-Tabasi, and R. E. Logé, "Quantitative prediction of crystallization in laser powder bed fusion of a zr-based bulk metallic glass with high oxygen content," *Materials and Design*, vol. 239, Mar. 2024. DOI: 10.1016/j.matdes.2024.112744.

[129] S. I. Shahabad, U. Ali, Z. Zhang, A. Keshavarzkermani, R. Esmaeilizadeh, A. Bonakdar, and E. Toyserkani, "On the effect of thin-wall thickness on melt pool dimensions in laser powder-bed fusion of hastelloy x: Numerical modeling and experimental validation," *Journal of Manufacturing Processes*, vol. 75, pp. 435–449, Mar. 2022. DOI: 10.1016/J.JMAPRO.2022.01.029.

[130] Y. Sun, H. Zhao, R. Huang, L. Liu, C. Tan, D. Lin, B. Chen, X. Song, and R. Ma, "The effect of thickness on the defects and anisotropy of thin-wall hastelloy x fabricated via laser powder-bed fusion," *Journal of Materials Research and Technology*, vol. 27, pp. 703–717, Nov. 2023. DOI: 10.1016/J.JMRT.2023.10.025.

[131] J. Shi, S. Ma, S. Wei, J. P. Best, M. Stolpe, and B. Markert, "Connecting structural defects to tensile failure in a 3d-printed fully-amorphous bulk metallic glass," *Materials*

Science and Engineering: A, vol. 813, p. 141 106, May 2021. DOI: 10.1016/J.MSEA.2021.141106.

[132] R. Spatschek, C. Gugenberger, and E. Brener, "Effective elastic moduli in solids with high crack density," *Physical Review B - Condensed Matter and Materials Physics*, vol. 80, 14 Jul. 2009. DOI: 10.1103/PhysRevB.80.144106.

[133] M. Y., "Stress intensity factors handbook," *Soc. Mater. Sci., Japan*, 1986.

[134] P. Agarwal, D. Mathur, and S. S. Ghosh, "Formulation of stress concentration factor of a finite plate with an elliptical hole of high eccentricity ratio," *Lecture Notes in Mechanical Engineering*, pp. 113–122, 2021. DOI: 10.1007/978-981-16-1079-0_13/FIGURES/6.

[135] P. Novák, E. Duchková, A. Boháčová, A. Michalcová, F. Průša, K. Skotnicová, and I. Szurman, "Synthesis and properties of iron silicides," *Journal of Materials Research and Technology*, vol. 38, pp. 165–174, Sep. 2025. DOI: 10.1016/J.JMRT.2025.07.129.

[136] J. Lentz, A. Röttger, and W. Theisen, "Hardness and modulus of fe2b, fe3(c,b), and fe23(c,b)6 borides and carboborides in the fe-c-b system," *Materials Characterization*, vol. 135, pp. 192–202, Jan. 2018. DOI: 10.1016/J.MATCHAR.2017.11.012.

[137] P. A. Hooper, "Melt pool temperature and cooling rates in laser powder bed fusion," *Additive Manufacturing*, vol. 22, pp. 548–559, Aug. 2018. DOI: 10.1016/j.addma.2018.05.032.

[138] B. Zheng, Y. Zhou, J. E. Smugeresky, and E. J. Lavernia, "Processing and behavior of fe-based metallic glass components via laser-engineered net shaping," *Metallurgical and Materials Transactions A: Physical Metallurgy and Materials Science*, vol. 40, pp. 1235–1245, 5 Mar. 2009. DOI: 10.1007/S11661-009-9828-Y/FIGURES/11.

[139] V. K. Balla and A. Bandyopadhyay, "Laser processing of fe-based bulk amorphous alloy," *Surface and Coatings Technology*, vol. 205, pp. 2661–2667, 7 Dec. 2010. DOI: 10.1016/J.SURFCOAT.2010.10.029.

[140] X. Ye and Y. C. Shin, "Synthesis and characterization of fe-based amorphous composite by laser direct deposition," *Surface and Coatings Technology*, vol. 239, pp. 34–40, Jan. 2014. DOI: 10.1016/J.SURFCOAT.2013.11.013.

[141] A. Olleak, E. Adcock, S. Hinnebusch, F. Dugast, A. D. Rollett, and A. C. To, "Understanding the role of geometry and interlayer cooling time on microstructure variations in lpbf ti6al4v through part-scale scan-resolved thermal modeling," *Additive Manufacturing Letters*, vol. 9, Apr. 2024. DOI: 10.1016/j.addlet.2024.100197.

[142] K. Ettaieb, K. Godineau, S. Lavernhe, and C. Tournier, "Offline laser power modulation in lpbf additive manufacturing including kinematic and technological constraints offline laser power mod-ulation in lpbf additive manufacturing including kinematic and technological constraints offline laser power modulation in lpbf additive manufacturing including kinematic and technological constraints," *Rapid Prototyping Journal*, vol. 2022, pp. 80–91, 29 2022. DOI: 10.1108/RPJ-02-2022-0062Ãŕ.

[143] J. P. Oliveira, A. D. LaLonde, and J. Ma, "Processing parameters in laser powder bed fusion metal additive manufacturing," *Materials and Design*, vol. 193, Aug. 2020. DOI: 10.1016/j.matdes.2020.108762.

[144] N. Khitouni, R. Daly, J. Daza, A. H. Alsulami, J. J. Suñol, and M. Khitouni, "Characterization of the microstructural, magnetic, and thermal behaviors of boron-doped fe-co-ni alloys produced via mechanical alloying," *Journal of Applied Physics*, vol. 136, p. 35 103, 3 Jul. 2024. DOI: 10.1063/5.0213911/3303457.

[145] X. P. Li, C. W. Kang, H. Huang, and T. B. Sercombe, "The role of a low-energy–density re-scan in fabricating crack-free al85ni5y6co2fe2 bulk metallic glass composites via selective laser melting," *Materials & Design*, vol. 63, pp. 407–411, Nov. 2014. DOI: 10.1016/J.MATDES.2014.06.022.

[146] J. Dai, Y. G. Wang, L. Yang, G. T. Xia, Q. S. Zeng, and H. B. Lou, "Structural aspects of magnetic softening in fe-based metallic glass during annealing," *Scripta Materialia*, vol. 127, pp. 88–91, Jan. 2017. DOI: 10.1016/J.SCRIPTAMAT.2016.09.006.

[147] S. Xu, J. Wang, N. Wang, T. Wang, Z. Han, and Y. Wang, "Soft magnetic properties and corrosion resistance of the annealed (fe0.7co0.15ni0.15)75b21nb4 metallic glasses," *Materials Today Communications*, vol. 26, p. 101 906, Mar. 2021. DOI: 10.1016/J.MTCOMM.2020.101906.

[148] N. He, L. Song, W. Xu, J. Huo, J. Q. Wang, and R. W. Li, "The evolution of relaxation modes during isothermal annealing and its influence on properties of fe-based metallic

glass," *Journal of Non-Crystalline Solids*, vol. 509, pp. 95–98, Apr. 2019. DOI: 10.1016/J.JNONCRYSOL.2018.12.035.

[149] X. Yang, X. Cui, G. Jin, J. Liu, Y. Chen, and Z. Liu, "Soft magnetic property of (fe60co35ni5)78 si6b12cu1mo3 alloys by laser additive manufacturing," *Journal of Magnetism and Magnetic Materials*, vol. 466, pp. 75–80, Nov. 2018. DOI: 10.1016/j.jmmm.2018.06.085.

[150] A. B. Kustas, D. F. Susan, K. L. Johnson, S. R. Whetten, M. A. Rodriguez, D. J. Dagel, J. R. Michael, D. M. Keicher, and N. Argibay, "Characterization of the fe-co-1.5v soft ferromagnetic alloy processed by laser engineered net shaping (lens)," *Additive Manufacturing*, vol. 21, pp. 41–52, May 2018. DOI: 10.1016/j.addma.2018.02.006.

[151] X. Yang, J. Liu, X. Cui, G. Jin, Z. Liu, Y. Chen, and X. Feng, "Effect of remelting on microstructure and magnetic properties of fe-co-based alloys produced by laser additive manufacturing," *Journal of Physics and Chemistry of Solids*, vol. 130, pp. 210–216, Jul. 2019. DOI: 10.1016/j.jpcs.2019.03.001.

[152] M. Ahmadnia, E. Fereiduni, M. Yakout, M. Elbestawi, R. K. R. M, G. Vakil, and R. Muizelaar, "Optimizing magnetic performance of fe–50ni alloy for electric motor cores through lpbf: A study of as-built and heat-treated scenarios," *Journal of Materials Research and Technology*, vol. 29, pp. 2554–2571, Mar. 2024. DOI: 10.1016/j.jmrt.2024.02.011.

[153] A. K. Mazeeva, M. V. Staritsyn, V. V. Bobyr, S. A. Manninen, P. A. Kuznetsov, and V. N. Klimov, "Magnetic properties of fe–ni permalloy produced by selective laser melting," *Journal of Alloys and Compounds*, vol. 814, Jan. 2020. DOI: 10.1016/j.jallcom.2019.152315.

[154] C. V. Mikler, V. Chaudhary, T. Borkar, V. Soni, D. Choudhuri, R. V. Ramanujan, and R. Banerjee, "Laser additive processing of ni-fe-v and ni-fe-mo permalloys: Microstructure and magnetic properties," *Materials Letters*, vol. 192, pp. 9–11, Apr. 2017. DOI: 10.1016/j.matlet.2017.01.059.

[155] B. Li, W. Fu, H. Xu, B. Qian, and F. Xuan, "Additively manufactured ni-15fe-5mo permalloy via selective laser melting and subsequent annealing for magnetic-shielding structures: Process, micro-structural and soft-magnetic characteristics," *Journal of Mag-*

netism and Magnetic Materials, vol. 494, Jan. 2020. DOI: 10.1016/j.jmmm.2019.165754.

[156] D. Goll, D. Schuller, G. Martinek, T. Kunert, J. Schurr, C. Sinz, T. Schubert, T. Bernthaler, H. Riegel, and G. Schneider, "Additive manufacturing of soft magnetic materials and components," *Additive Manufacturing*, vol. 27, pp. 428–439, May 2019. DOI: 10.1016/j.addma.2019.02.021.

[157] M. Garibaldi, I. Ashcroft, N. Hillier, S. A. Harmon, and R. Hague, "Relationship between laser energy input, microstructures and magnetic properties of selective laser melted fe-6.9 wt si soft magnets," *Materials Characterization*, vol. 143, pp. 144–151, Sep. 2018. DOI: 10.1016/j.matchar.2018.01.016.

[158] M. Garibaldi, I. Ashcroft, J. N. Lemke, M. Simonelli, and R. Hague, "Effect of annealing on the microstructure and magnetic properties of soft magnetic fe-si produced via laser additive manufacturing," *Scripta Materialia*, vol. 142, pp. 121–125, Jan. 2018. DOI: 10.1016/j.scriptamat.2017.08.042.

[159] T. N. Lamichhane, H. Wang, C. Chinnasamy, L. Sethuraman, F. A. List, P. Nandwana, J. Yan, Z. Gai, and M. P. Paranthaman, "An additively manufactured fe-3si stator for a high-performance electrical motor," *Applied Sciences (Switzerland)*, vol. 15, 4 Feb. 2025. DOI: 10.3390/app15041706.

[160] TDK Electronics. "Ferrite materials and accessories – product overview." (), [Online]. Available: https://product.tdk.com/en/products/ferrite/index.html (visited on 11/28/2025).

[161] G. Chatzipirpiridis, S. Gervasoni, C. Fischer, O. Ergeneman, E. Pellicer, B. J. Nelson, and S. Pané, "3d printing of thermoplastic-bonded soft- and hard-magnetic composites: Magnetically tuneable architectures and functional devices," *Advanced Intelligent Systems*, vol. 1, p. 1 900 069, 6 Oct. 2019. DOI: 10.1002/AISY.201900069.

[162] A. Amirov, A. Omelyanchik, D. Murzin, V. Kolesnikova, S. Vorontsov, I. Musov, K. Musov, S. Khashirova, and V. Rodionova, "3d printing of pla/magnetic ferrite composites: Effect of filler particles on magnetic properties of filament," *Processes 2022, Vol. 10, Page 2412*, vol. 10, p. 2412, 11 Nov. 2022. DOI: 10.3390/PR10112412.